

# An equatorial thermal wind equation: Applications to Jupiter

Philip S. Marcus<sup>a,b,\*</sup>, Joshua Tollefson<sup>c</sup>, Michael H. Wong<sup>d</sup>, Imke de Pater<sup>c,d</sup>

<sup>a</sup> Department of Mechanical Engineering, University of California, Berkeley, CA 94720, United States

<sup>b</sup> Program in Applied Science & Technology, University of California, Berkeley, CA 94720, United States

<sup>c</sup> Department of Earth and Planetary Science, University of California, Berkeley, CA 94720, United States

<sup>d</sup> Department of Astronomy, University of California, Berkeley, CA 94720, United States

## ARTICLE INFO

### Article history:

Received 26 July 2017

Revised 24 September 2018

Accepted 24 September 2018

Available online 25 September 2018

## ABSTRACT

To relate the vertical wind shear to horizontal temperature gradients at and near the equator, we derive an “Equatorial Thermal Wind Equation” (EQTWE) using a minimum set of assumptions that are easily satisfied for the atmospheres of all the giant planets and Earth. Similar to the textbook Thermal Wind Equation (TWE), the EQTWE requires a small Rossby number, but the relevant Rossby number for the EQTWE depends on the velocity and length scales of the equatorial flows, and on the Coriolis parameter at the north pole (which is large), rather than the Coriolis parameter at the equator (which goes to zero). Unlike the TWE, the EQTWE is valid only for the east-west component of the wind. We apply the EQTWE to the Jovian wind measured by the *Galileo* probe Doppler wind experiment at jovicentric latitude 6.53°N (7.46°N jovigraphic), which is valid because the EQTWE is accurate at latitudes  $\theta < 18^\circ$ . Assuming that this wind profile holds at all longitudes, the EQTWE shows that near the equator at altitudes at 0.8 bar  $< P < 5$  bar, the atmosphere is anomalously cool with respect to the surrounding flow, and at 5 bar  $\leq P < 13$  bar, it is warm. These anomalies imply adiabatic up-welling (down-welling) at 0.8 bar  $< P < 5$  bar (at 5 bar  $\leq P \leq 13$  bar), which suggests a Jovian global circulation model with two layers of Hadley cells, with an upper layer like the one on Earth, and the lower has cells with the opposite rotation. Applying the EQTWE to CIRS temperatures at altitudes above 330 mbar, shows that the large vertical wind shears measured by the *Galileo* probe extend to higher altitudes, and at 3 mbar create a stratospheric equatorial jet with a velocity of 205 m/s (almost 50% faster than the speed that had been obtained earlier with the TWE).

© 2018 Elsevier Inc. All rights reserved.

## 1. Introduction and motivation

The Thermal Wind Equation (TWE) (e.g., Pedlosky, 1979 Sections 2.6, 2.9b, and 6.5) relates the vertical shear of the horizontal velocities to the horizontal gradients of the temperature in a rotating system such as the atmosphere of a planet. The TWE works well at polar and mid-latitudes, and sometimes, depending upon the application, at sub-tropical latitudes. However, it is reputed not to work in regions close to the equator because the Coriolis force is small and the traditional Rossby numbers are of order unity there (see Section 3.2). Despite this, since there is plentiful data and interesting phenomena near the equator, the TWE is frequently applied there. Before dismissing the application of the TWE near the equator, we note that observations by Allen and Sherwood (2008) of the east-west component of Earth’s atmospheric velocities and radiosonde temperature data sets show

that the TWE works “accurately, even in the deep tropics, where the Coriolis force approaches zero”. This observation suggests that for the east-west component of the velocity, there either must be a variant of the TWE that works well at the equator, or that for some unknown reason the TWE does not require approximate geostrophic balance (which breaks down at the equator). Therefore, it would be useful to determine the conditions (if any) for which the TWE is valid close to the equator, and better yet, to derive a new equation that relates the vertical shear of horizontal velocities to the horizontal gradients of the temperature that is valid at and near the equator. In this paper we derive such an equation, and refer to it as the “Equatorial Thermal Wind Equation” (EQTWE). We also show the circumstances under which a modified TWE can sometimes be used at the equator. The EQTWE is not only accurate at the equator but also in tropical regions at latitudes  $|\theta| \leq 18^\circ$  with only 10% errors.

Our EQTWE has four features, all independent of each other, that make it practical to use: (1) it does not become invalid when the traditional Rossby number becomes large (as usually happens near the equator); (2) it does not cease to produce useful

\* Corresponding author.

E-mail address: [pmarcus@me.berkeley.edu](mailto:pmarcus@me.berkeley.edu) (P.S. Marcus).

information, i.e., reducing to “zero equals zero”, at the equator as some modified thermal wind equations do (c.f., [de la Torre Juárez et al., 2002](#)); (3) it does not become ill-conditioned at the equator by requiring the division of one very small number by another to obtain the shear at the equator; and (4) it provides a relationship between the horizontal temperature gradient and the vertical shear at the equator, rather than the wind shear with respect to the axis of rotation (c.f., [de la Torre Juárez et al., 2002](#); [Li et al., 2008](#); [Li et al., 2013](#)). Our EQTWE can not only be used to study atmospheric dynamics in the equatorial region of the Earth, but also in major gaseous planets whose equatorial regions are often the most accessible to observers using ground-based telescopes, the Hubble Space Telescope, and fly-by satellites. Equatorial regions of the planets are rich in interesting dynamical features whose behavior we want to understand, such as:

- *The Jovian vertical wind shear deduced from the Galileo probe Doppler wind experiment.* The probe descended into Jupiter’s atmosphere at the South edge of a 5  $\mu\text{m}$  hot spot at 7.46°N jovigraphic latitude ([Young, 2003](#)) and measured the zonal winds as a function of altitude ([Atkinson et al., 1998](#)). Since geostrophic balance does not hold at this low-latitude, attempts to explain the data have been made by making use of a more general gradient wind balance ([Showman and Ingersoll, 1998](#)). To date, however, no model has fully explained the observed wind shear. We apply our EQTWE to the probe velocities in [Section 3.3](#).
- *The Jovian equatorial stratospheric jet.* [Flasar et al. \(2004\)](#) reported an intense stratospheric equatorial jet at an altitude near 3 mbar, which they believe is evidence of a 4–5 year quasi-biennial oscillation. They used the TWE to find jet velocities of 140 m/s, which are nearly the same magnitude as the largest jet velocities at the visible Jovian cloud-tops. This finding is somewhat contradictory to that of [Li et al. \(2006\)](#) who found that the wind shear is negligible between 319 and 499 mbar. However, the TWE was used near 5° and at 3°, respectively, in these two studies, which is formally too close to the equator to use the TWE. We apply our EQTWE to the CIRS temperatures in [Section 3.2](#) to re-examine the stratospheric jet.
- *Saturn’s equatorial jet.* Saturn has a broad and fast equatorial jet, with a narrow “jet within a jet” showing up between  $\pm 3^\circ$  latitude, in data taken in 2004 and later ([García-Melendo et al., 2010](#)). Wind speeds derived from *Cassini* ISS, *Voyager*, and Hubble images differ with wavelength and over time ([Sánchez-Lavega et al., 2016](#); [Porco et al., 2005](#)). [Sánchez-Lavega et al. \(2016\)](#) disentangled vertical and temporal trends to summarize the evolution of this complex structure from the *Voyager* era to the present day. Saturn’s equatorial region also experiences a Stratospheric Oscillation, where the winds and temperature vary periodically ([Li et al., 2008](#)). An EQTWE could elucidate how variations in temperature quantitatively affect changing shape, vertical structure, and speed of the equatorial winds. This approach would be particularly valuable in the narrow high-speed jet, whose position at the equator makes it intractable for the textbook TWE.
- *Neptune’s zonal vertical wind shear.* Significant vertical wind shear is detected in Neptune’s equatorial region throughout the upper atmosphere. Vertical wind shear in Neptune’s stratosphere (120 mbar–30 mbar) was calculated from temperature retrievals from the infrared interferometer spectrometer (IRIS) on *Voyager 2*, showing the winds decreasing in strength with height ([Conrath et al., 1989](#)). Retrievals of vertical wind shear from stellar occultation measurements found comparable vertical wind shear values, finding that the winds decayed in magnitude at 0.38 mbar compared to the 100 mbar velocities following the zonal wind profile derived from *Voyager*

images ([French et al., 1998](#)). Cloud tracking from Keck/NIRC2 images found that zonal velocity profiles differed at the equator between filters ([Fitzpatrick et al., 2014](#); [Tollefson et al., 2018](#)). These filters probe different altitudes near and below the tropopause (1 bar–100 mbar), implying variations of the zonal flow with depth. The observed vertical wind shear in these studies is opposite in direction of the stratospheric wind shear and is inconsistent with the TWE and measured *Voyager*/IRIS temperature gradients ([Fletcher et al., 2014](#)). Neptune’s rapid equatorial winds at the cloud tops (300–400 m/s) also mean that geostrophic balance breaks down there. [Tollefson et al. \(2018\)](#) use the EQTWE, derived in this paper, to show how temperature variations in latitude along with meridional variations in methane abundance explain the observed vertical wind shear.

- *Jupiter’s deep equatorial ammonia plume.* Understanding this plume ([de Pater et al., 2016](#); [Li et al., 2017](#)) and its implications to the velocities measured by the *Galileo* probe is important because the latitude of the probe entry and of the persistent plume are nearly the same. This is discussed in [Section 3.5](#).

Others, c.f., [Flasar et al. \(2005\)](#) in studying Titan and [Flasar et al. \(2004\)](#) in studying Jupiter, have noted the breakdown of the textbook TWE at low latitudes and the utility of having a modified TWE valid near the equator. [de la Torre Juárez et al. \(2002\)](#) and [Li et al. \(2008; 2013\)](#) developed a modified TWE valid near the equator that relates the horizontal variation in the temperature to the derivative of the zonal flow with respect to the  $z$ -axis of a cylindrical coordinate system, or equivalently the rotation axis of a planet. In contrast, the textbook TWE and the EQTWE that we develop here relate the horizontal variation in the temperature to the derivative of the zonal flow with respect to  $r$ , the radial coordinate of a spherical coordinate system, or equivalently the local vertical coordinate of a planet. Near the equator, the derivative with respect to  $z$  is approximately equal to the derivative with respect to the local north-south coordinate, so the information in the modified TWE developed by [de la Torre Juárez et al. \(2002\)](#) (in their Eq. (10)) and by [Li et al. \(2008; 2013\)](#) is literally orthogonal to the information in the EQTWE. [de la Torre Juárez et al. \(2002\)](#) also derived a modified thermal wind equation (their Eq. (12)) which they state can be used at the equator. Unfortunately, this leads to a modified thermal wind equation that makes the vertical wind shear zero at the equator (and almost zero near the equator, up to and including the latitude of the *Galileo* probe entry), which produces results inconsistent with observations. (See [Section 3.2](#).)

[Andrews et al. \(1987\)](#) (in their Eq. (8.2.2)) also proposed a modified thermal wind equation valid at the equator on Earth, but their derivation was not general, and the authors assumed that their modified thermal wind equation had very limited applicability (see the second footnote in [Section 4.2](#)). Other methods, such as the use of Jupiter’s gravity moments measured by the ongoing *Juno* mission, can measure Jupiter’s internal differential rotation ([Kaspi et al., 2017; 2018](#); [Guillot et al., 2018](#)). Unlike the TWE, these measurements can be used to find the zonal velocity at the equator. However, vertical zonal shears have not yet been determined with this method, and, in fact, the functional form of the vertical shear needs to be assumed by [Kaspi et al. \(2018\)](#) and [Guillot et al. \(2018\)](#) to carry out their calculations.

In the following section, we remind the reader about the assumptions used in the standard thermal wind equation, and then summarize our results, including: the EQTWE, the list of assumptions used in its derivation, and estimates of fractional errors in the equation in terms of dimensionless quantities. In [Section 3](#) we apply the EQTWE to Jupiter’s *Galileo* probe data to derive a temperature profile (as a function of depth and latitude) near the equator

that we show to be consistent with a 2-layer cellular global circulation model of the atmosphere near the equator (Ingersoll et al., 2000; Showman and de Pater, 2005). We also apply the EQTWE to CIRS temperatures at altitudes of 500 mbar and above to show that the strong vertical wind shear measured by the *Galileo* probe at 0.7 bar continues to altitudes up to 1 mbar. These findings are in contrast to those found earlier (Li et al., 2006) with the TWE that showed that the wind shear vanishes at these altitudes. The qualitative difference between the results of the EQTWE and of the TWE analysis illustrates the importance of the EQTWE.

We further show with the EQTWE that the Jovian stratospheric equatorial jet is almost 50% faster than found by Flasar et al. (2004), whose application of the textbook TWE did not permit them to resolve the jet peak velocity at the equator and noted that their derived velocity is a lower bound to the actual jet speed. We also consider the implications of the EQTWE to the equatorial global circulations at the Jovian equator and compare our results to *Juno* findings. Our conclusions, in Section 4, include a discussion of the circumstances under which the textbook TWE is valid at low latitudes: *if applied correctly, if temperature gradients of sufficient accuracy can be obtained, and if the flow is sufficiently symmetric about the equator*. Three Appendices give the complete derivation of the EQTWE. Because it is generally assumed that the TWE can never be used at the equator and that the modified thermal wind equation of Andrews et al. (1987) can be used only under very restrictive conditions, we decided that it would be worthwhile to publish in the Appendices the full, unabridged derivation of the EQTWE, including its limitations and fractional errors.

## 2. Summary of the thermal wind equations

The standard textbook TWE (c.f. Pedlosky, 1979, Section 2.9b) written in terms of spherical coordinates is:

$$f_0 \sin \theta \frac{\partial \mathbf{v}_\perp(r, \theta, \phi)}{\partial r} = \frac{g}{T} \hat{\mathbf{r}} \times \nabla_\perp T \Big|_P, \quad (1)$$

where  $f_0 \equiv 2\Omega_0$  is the Coriolis parameter at the north pole (so it is a constant, rather than a function of latitude  $\theta$ );  $\Omega_0$  is the angular velocity of the planet around its  $z$ -axis (using a spherical coordinate system in which  $z = r \sin \theta$ , where  $r$  is the radius);  $\phi$  is the longitude;  $\mathbf{v}_\perp$  is the horizontal ( $\theta$  and  $\phi$ ) component of the velocity; a “hat” means a unit vector;  $\nabla_\perp$  is the horizontal component of the gradient operator;  $T$  is the temperature;  $\rho$  is the density;  $P$  is the pressure; and  $g$  is the gravity and is in the radial direction. On the right side of the equation, we have used the pressure as the independent vertical coordinate, rather than  $r$ , and  $|_P$  means to hold  $P$ , rather than  $r$ , constant when computing derivatives so that the gradient is along a constant pressure surface.

Assumptions needed for the textbook TWE to be valid are: (i) The characteristic time over which the flow changes is slow. In particular, a sufficient (but not necessary) condition for the slowness is that the characteristic time over which the flow changes is of order or slower than the advective time (the time it takes for the characteristic velocity  $V$  to travel over the characteristic length  $L$  of the flow features). Fast waves can invalidate this assumption. (ii) Flows are in approximate vertical hydrostatic equilibrium. (iii) The traditional Rossby number  $Ro \equiv V/(f_0 L \sin \theta)$  is small, where  $\theta$  is the latitude at which the TWE is applied.

While these seem like straight-forward constraints, they have many subtleties because there are often different characteristic velocities and lengths in the east-west, north-south and vertical directions. As pointed out by Pedlosky (1979) (Sections 2.6, 2.9b, and 6.5), these different velocities and scales, especially when the aspect ratios of the flows' features are small (as they are in the Jovian atmosphere), can make the required conditions of, and the fractional errors in, the TWE more subtle and complex. Thus, in

deriving the EQTWE, we shall not assume that all length scales are the same nor that all velocity scales are the same. For this reason, our stated required conditions for the validity of the EQTWE and its fractional errors appear to be more restrictive and complicated than those of the textbook TWE, but actually they are not, as discussed in Section A.3 in Appendix A. A final necessary assumption for the TWE is that the flow obeys

$$\frac{\nabla P}{P} = \frac{\nabla T}{T} + \frac{\nabla \rho}{\rho}, \quad (2)$$

or equivalently that  $(1/\rho)(\partial \rho / \partial \theta)|_P = -(1/T)(\partial T / \partial \theta)|_P$  and  $(1/\rho)(\partial \rho / \partial \phi)|_P = -(1/T)(\partial T / \partial \phi)|_P$  is valid, which holds for an ideal gas equation with one component or for an ideal gas equation in which the mixing ratios of the various components do not vary significantly with location (i.e., that the anomalies in the density of the gas are due to thermal, rather than computational, anomalies). If this last assumption does not hold, then replacing the kinetic temperature in the TWE with the virtual temperature will make the TWE valid (c.f., Sun et al., 1991; Tollefson et al., 2018, and Appendix C).

Our required assumptions for deriving our EQTWE are:

1. The flow changes on a slow time scale. In particular, the magnitude of  $\partial \omega_\phi / \partial t$  is much less than the magnitude of  $[g/(r_0 \rho)](\partial \rho / \partial \theta)|_P$ , where  $\omega_\phi$  is the azimuthal component of the vorticity  $\boldsymbol{\omega} \equiv \nabla \times \mathbf{v}$ , where  $\mathbf{v}$  is the fluid velocity, and where  $r_0$  is the radius of the planet where the EQTWE is applied. A sufficient, but not necessary, condition is that the characteristic time over which the flow changes is longer than the advective timescale.
2. The vertical scale  $D$  of the flow is less than  $r_0$ .
3. The vertical scale  $D$  is less than or equal to  $L_\theta$ , the characteristic length scale in the north-south direction at the equator.
4. The vertical scale  $D$  is less than or equal to  $L_\phi$ , the characteristic length scale in the east-west direction at the equator.
5. The flow obeys Eq. (2).

These assumptions are modest, and easily hold for all of the giant gas planets since the atmospheric scale height is roughly equal to  $D$  and is much less than the scale of the flow and the radius of the planet. In addition, as in the TWE, if assumption # 5 in the list enumerated above does not hold, then the EQTWE is valid if the kinetic temperature is replaced with the virtual temperature (See Appendix C).

In the Appendices, we derive the EQTWE that relates the vertical shear of the azimuthal component of the velocity  $v_\phi$  to the meridional change of the temperature  $T$  with respect to latitude  $\theta$ . Our EQTWE in its most general form is:

$$-\frac{g'}{r_0 T} \frac{\partial^2 T}{\partial \theta^2} \Big|_P = f_0 \frac{\partial v_\phi}{\partial r}, \quad (3)$$

where  $g' \equiv g - (f_0^2 r_0 \cos \theta)/4$  is the effective gravity (i.e.,  $g'$  is  $g$  minus the centrifugal acceleration in the radial direction). For Jupiter, Neptune, and Uranus  $g' = g$  within 10%, whereas for Saturn the difference is larger. In Eq. (3),  $v_\phi$  and  $T$  are both averaged over all longitudes. Note that the EQTWE applies only to  $v_\phi$ , the east-west component of the wind and states nothing about  $v_\theta$ , the north-south component, whereas, the textbook TWE applies to both components.

In the Appendices, we derive the fractional errors<sup>1</sup> of the EQTWE and show that they are

$$O \left[ \overline{Ro} \left( \frac{r_0}{L_\theta} \frac{V_\phi^2}{V_\theta^2}, \frac{r_0}{L_\phi} \frac{V_\theta}{V_\phi}, \frac{r_0}{L_\phi}, \frac{D}{L_\theta} \right), \frac{DV_\phi^2}{gL_\theta^2}, \frac{DV_\theta^2}{gL_\theta^2}, \frac{DV_\phi V_\theta}{gL_\phi L_\theta}, \frac{Dr_0}{L_\theta^2}, \right. \\ \left. \widetilde{Ro}, \left( \frac{[T^A]}{[T^M]} \right)^2, \left( \frac{[\rho^A]}{[\rho^M]} \right)^2, \left( \frac{[\mathbf{v}^A]}{[\mathbf{v}^M]} \right)^2, 0.0003 \theta_0^2 \right], \quad (4)$$

where  $V_\theta$  is the characteristic velocity in the north-south direction at the equator;  $V_\phi$  is the characteristic east-west velocity at the equator;  $\overline{Ro} \equiv V_\phi/(f_0 L_\theta)$  and is a modified Rossby number that does not blow up at the equator because it does not have  $\sin\theta$  in the denominator;  $\widetilde{Ro} \equiv V_\phi/(f_0 r_0)$  is another modified Rossby number that does not blow up at the equator; and  $\theta_0$  is the latitude (in degrees) where the EQTWE is applied. In expression (4), the A and M superscripts refer to the spatial symmetries of the flow. Specifically, the density can be decomposed into a component that is mirror-symmetric with respect to the equator,

$$\rho^M(r, \theta, \phi) \equiv [\rho(r, \theta, \phi) + \rho(r, -\theta, \phi)]/2, \quad (5)$$

and a part that is anti-mirror-symmetric,

$$\rho^A(r, \theta, \phi) \equiv [\rho(r, \theta, \phi) - \rho(r, -\theta, \phi)]/2. \quad (6)$$

A similar decomposition holds for the temperature  $T(r, \theta, \phi) \equiv T^M(r, \theta, \phi) + T^A(r, \theta, \phi)$  and for pressure and the  $\phi$  and  $r$  components of the velocity. For the  $\theta$ -component of the velocity, we define the terms oppositely with

$$v_\theta^M(r, \theta, \phi) \equiv [v_\theta(r, \theta, \phi) - v_\theta(r, -\theta, \phi)]/2, \quad (7)$$

and

$$v_\theta^A(r, \theta, \phi) \equiv [v_\theta(r, \theta, \phi) + v_\theta(r, -\theta, \phi)]/2. \quad (8)$$

Due to the symmetries of the equations of motion, it is possible that an equilibrium flow could be perfectly mirror-symmetric with  $0 \equiv \mathbf{v}^A(r, \theta, \phi) = \rho^A(r, \theta, \phi) = T^A(r, \theta, \phi)$ .  $[T^A]$ ,  $[T^M]$ ,  $[\rho^A]$ ,  $[\rho^M]$ ,  $[\mathbf{v}^A]$ , and  $[\mathbf{v}^M]$  are defined as the characteristic values of the anti-mirror-symmetric and mirror-symmetric components of their corresponding fields. The giant planets are nearly mirror-symmetric. At and near the equator, the velocity and thermodynamic variables  $T$  and  $\rho$  of the atmospheres of the gas giant planets are nearly mirror-symmetric with respect to the equator. For example on Jupiter as Fig. 1 shows, the average temperature at 500 mbar at the equator is about 140K. There are latitudinal variations about this average temperature of approximately  $\pm 5$ K, but these fluctuations themselves are nearly symmetric with respect to the equator. Therefore, even if the magnitude of the temperature fluctuations near the equator increases to  $\pm 20$  K at depths of 10 bar (see Section 3), the characteristic value of the magnitude of  $T^A$  at the equator,  $[T^A]$ , divided by the characteristic value of the magnitude of  $T^M$  at the equator,  $[T^M]$  is likely to be no greater than 0.05. We would also expect  $[\rho^A]/[\rho^M]$  and  $[\mathbf{v}^A]/[\mathbf{v}^M]$  to be less than 0.05 at the equator, so the fractional error due to anti-mirror-symmetric behavior of the flow (i.e., the last three terms in expression (4) are less than  $(0.05)^2$  or less than 1%.<sup>2</sup>

Note that none of these fraction errors in expression (4) depend on the traditional Rossby number or any other term that depends (inversely) on the local value of the Coriolis force  $f \equiv f_0 \sin\theta$ . The fact that the fractional errors in the EQTWE are independent of the traditional Rossby number is what allows the EQTWE to be useful at the equator. All of the terms in expression (4) for the giant gas planets are small as shown in Table 1.

<sup>1</sup> meaning that the difference between the left and right sides of Eq. (3) are at most the fractional error multiplied by the left or right side of Eq. (3).

<sup>2</sup> Even Uranus, with its large obliquity, has small  $[\rho^A]/[\rho^M]$  and  $[T^A]/[T^M]$  because the mean density and temperature at the equator are much larger than their corresponding meridional gradients,  $\partial\rho/\partial\theta$  and  $\partial T/\partial\theta$ , at the equator.

The EQTWE is also valid a reasonable distance away from the equator. The derivation of the EQTWE, given in the Appendices, uses a Taylor series expansion in  $\theta$  about the equator, and the fractional errors due to this expansion are  $O(\theta^2)$  (where  $\theta$  is in radians). Therefore, the EQTWE is not limited to the equator, but rather, can be applied at a tropical latitude  $\theta_0$ , leading to the last term in expression (4). For  $|\theta| < 18^\circ$ , that fractional error is less than 10%. On the other hand, the TWE would have a fractional error dependent on  $1/\sin(\theta) > 3$  at these same latitudes due to the dependence on  $\theta$  in the traditional Rossby number. Thus, for many applications, the EQTWE is more accurate than the TWE at latitudes as high as  $|\theta| = 18^\circ$ .

The fractional errors in expression (4) appear to be much more complicated and possibly restrictive than those in the usual TWE. However, a thorough derivation of the TWE, similar to the one we used to derive the EQTWE in the Appendices, would yield an expression for the fractional errors as complex as the one in Eq. (4). If in our analysis of the errors of the EQTWE, we had assumed that  $V_\phi$  (the characteristic velocity in the east-west direction) is of the same order as  $V_\theta$  (the characteristic velocity in the north-south direction) and that  $L_\phi$  is of the same order as  $L_\theta$  (as done in the standard derivation and analysis of the TWE), and that  $[T^A]/[T^M] \simeq [\rho^A]/[\rho^M] \simeq [\mathbf{v}^A]/[\mathbf{v}^M]$ , then the fractional errors in the EQTWE in expression (4) reduce to

$$O \left[ \overline{Ro} \left( \frac{r_0}{L_\theta}, \frac{L_\theta}{r_0} \right), \frac{DV_\theta^2}{gL_\theta^2}, \frac{Dr_0}{L_\theta^2}, \left( \frac{[T^A]}{[T^M]} \right)^2, 0.0003 \theta_0^2 \right], \quad (9)$$

Without loss of generality, the EQTWE in Eq. (3) can be written as

$$-\frac{g'}{r_0 T^M} \frac{\partial^2 T^M}{\partial \theta^2} \Big|_p = f_0 \frac{\partial v_\phi^M}{\partial r}, \quad (10)$$

or

$$-\left\{ \frac{g'}{r_0 T} \frac{\partial^2 T}{\partial \theta^2} \Big|_p \right\}^M = f_0 \frac{\partial v_\phi^M}{\partial r}, \quad (11)$$

with the same frame fractional errors as in expression (4), where the large curly brackets with the superscript  $M$ ,  $\{\}^M$  means “take the mirror-symmetric component of the quantity within the brackets”. Depending upon the application, the form in Eqs. (3), (10), or (11) will be the most useful form of the EQTWE.

In atmospheres in which large changes in the mixing ratios have a significant impact on the density anomalies, the virtual temperature can be substituted for the kinetic temperature in Eqs. (3), (10), or (11); or we can eschew the temperature altogether and write the EQTWE directly in terms of the density as an “equatorial density wind equation” or EQDWE:

$$\frac{g'}{r_0 \rho} \frac{\partial^2 \rho}{\partial \theta^2} \Big|_p = f_0 \frac{\partial v_\phi}{\partial r}, \quad (12)$$

or

$$\frac{g'}{r_0 \rho^M} \frac{\partial^2 \rho^M}{\partial \theta^2} \Big|_p = f_0 \frac{\partial v_\phi^M}{\partial r}, \quad (13)$$

or

$$\left\{ \frac{g'}{r_0 \rho} \frac{\partial^2 \rho}{\partial \theta^2} \Big|_p \right\}^M = f_0 \frac{\partial v_\phi^M}{\partial r}, \quad (14)$$

with same fractional errors as in expression (4).

In contrast to our EQTWE, the east-west component of the textbook TWE in Eq. (1), is:

$$-\frac{1}{\sin\theta} \frac{g}{r_0 T} \frac{\partial T}{\partial \theta} \Big|_p = f_0 \frac{\partial v_\phi}{\partial r}. \quad (15)$$

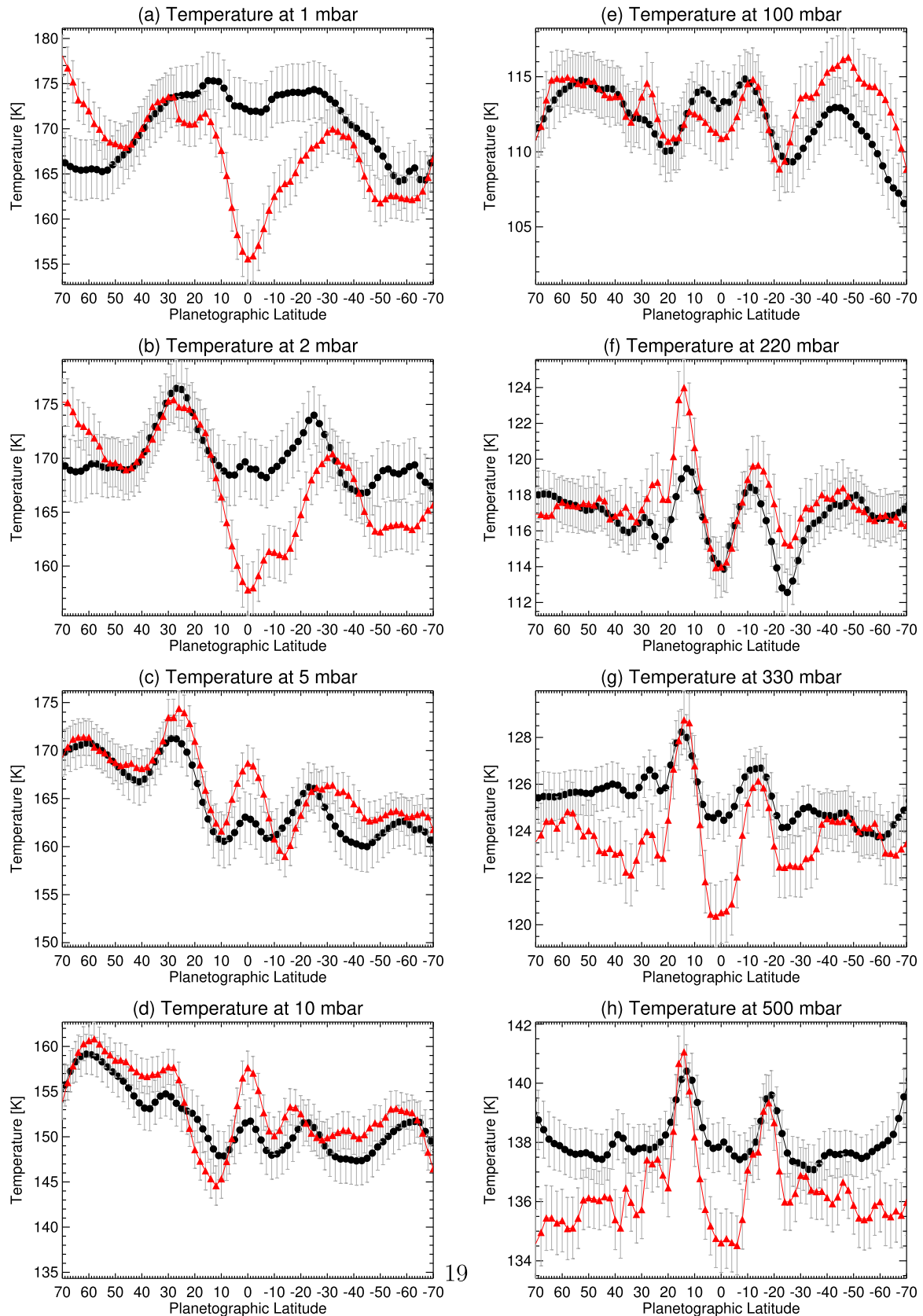


**Fig. 1.** Longitudinally-averaged temperatures derived from TEXES (black circles) and CIRS (red triangles) from 1–500 mbar, taken from Fig. 14 in Fletcher et al. (2016). Gray bars represent retrieval uncertainties. Our analysis in Section 7 uses the CIRS data since it was taken roughly 4 years after the Doppler Wind Experiment, and would therefore be on the same cycle as the Quasi Quadrennial Oscillation.

**Table 1**

Above the double horizontal lines: estimates of the relevant parameters of Jupiter, Saturn, Uranus, and Neptune. All values in SI units. Below the double horizontal lines: most of the dimensionless fractional errors in expression (4) for the EQTWE in Eq. (3), showing that the EQTWE is accurate to 1% at the equator for all of the giant gaseous planets.

Parameter and description	Jupiter	Saturn	Uranus	Neptune
$r_0$ Equatorial Radius	$7.0 \times 10^7$	$5.8 \times 10^7$	$2.5 \times 10^7$	$2.5 \times 10^7$
$g$ Gravitational Acceleration	25	10	9	11
$\Omega_0$ Angular velocity	$1.7 \times 10^{-4}$	$1.6 \times 10^{-4}$	$1.0 \times 10^{-4}$	$1.1 \times 10^{-4}$
$D$ Vertical Length Scale	$2.7 \times 10^4$	$6.0 \times 10^4$	$2.8 \times 10^4$	$2.0 \times 10^4$
$L_\phi$ Longitudinal Length Scale	$10^8$	$10^8$	$10^8$	$10^8$
$L_\theta$ Latitudinal Length Scale	$10^7$	$10^7$	$10^7$	$10^7$
$V_r$ Characteristic Vertical Velocity	1–10	1–10	1–100	1–100
$V_\phi$ Characteristic Zonal Velocity	100	300	100	300
$V_\theta$ Characteristic Latitudinal Velocity	1–10	1–10	1–100	1–100
$\bar{R}_0 \equiv V_\phi / (f_0 L_\theta)$	0.03	0.09	0.05	0.14
$\bar{R}_0 (r_0 / L_\theta) (V_\theta / V_\phi)^2$	0.002	0.0005	0.1	0.04
$\bar{R}_0 (r_0 / L_\phi) (V_\theta / V_\phi)$	0.002	0.002	0.01	0.01
$\bar{R}_0 r_0 / L_\phi$	0.02	0.05	0.01	0.04
$\bar{R}_0 D / L_\theta$	$8 \times 10^{-5}$	$5 \times 10^{-4}$	$1 \times 10^{-4}$	$3 \times 10^{-4}$
$DV_\phi^2 / (gL_\phi^2)$	$1 \times 10^{-9}$	$5 \times 10^{-8}$	$3 \times 10^{-9}$	$2 \times 10^{-8}$
$DV_\theta^2 / (gL_\theta^2)$	$1 \times 10^{-9}$	$6 \times 10^{-9}$	$3 \times 10^{-7}$	$2 \times 10^{-7}$
$DV_\theta V_\phi / (gL_\phi L_\theta)$	$1 \times 10^{-9}$	$2 \times 10^{-8}$	$3 \times 10^{-8}$	$5 \times 10^{-8}$
$Dr_0 / L_\theta^2$	$2 \times 10^{-2}$	$3 \times 10^{-2}$	$7 \times 10^{-3}$	$5 \times 10^{-3}$
$\bar{R}_0 \equiv V_\phi / (f_0 r_0)$	0.004	0.02	0.02	0.05

Note the EQTWE depends on the second derivative of  $T$ , while the TWE depends on the first derivative. More importantly, the TWE has a  $1/\sin\theta$  term on the right side (making it inapplicable near the equator), while the EQTWE does not have this dependence on  $\theta$ . Both the TWE and EQTWE are approximations and contain many fractional errors, but only the TWE includes errors that are of order the traditional Rossby number, and that is worrisome because near the equator the traditional Rossby number and the fractional errors it creates can be greater than unity.

### 3. Application to the Galileo Probe Doppler Wind Experiment and to the equatorial stratospheric jet

#### 3.1. Assumptions about the velocity field at the 5 $\mu\text{m}$ hot spots

In this section, we shall use the Jovian zonal winds measured by the *Galileo* Probe Doppler Wind Experiment in two ways. First, we use the wind speeds with the EQTWE to determine the temperature as a function of latitude and altitude at the altitudes where the probe measured the winds. These altitudes span pressures of 0.7–21 bar where the temperatures have never been retrieved by remote sensing. Second, we use the Jovian wind speeds measured by the probe at an altitude near 700 mbar to establish a reference altitude where the value of the zonal wind at the equator is known precisely. This reference speed is needed to calculate zonal velocities at the equator from the wind shears calculated with the EQTWE at altitudes spanning 0.7 bar to 1 mbar, well above the altitudes where the probe measured the zonal winds. Both of these applications of the probe-measured wind speeds require that we know the accuracy of the winds at the latitude of the probe entry site. The *Galileo* probe descended into Jupiter on December 7, 1995 into the southern edge of a 5  $\mu\text{m}$  hot spot at 7.46°N jovigraphic and transmitted data to the orbiter for 57 min before contact was lost. Zonal wind velocities were derived from the probe’s location via the Doppler Wind Experiment and are shown, with an error envelope, in Fig. 2 (taken from Fig. 4 in Atkinson et al., 1998).

Understanding properties of hot spots is important in this study because we need to know if the velocities measured by the *Galileo* probe were unique to a hot spot or representative of the average zonal flow where the probe entered. The probe showed that a hot spot is a dry region with low molecular weight (Niemann et al., 1998; Wong et al., 2004). There is no universally accepted

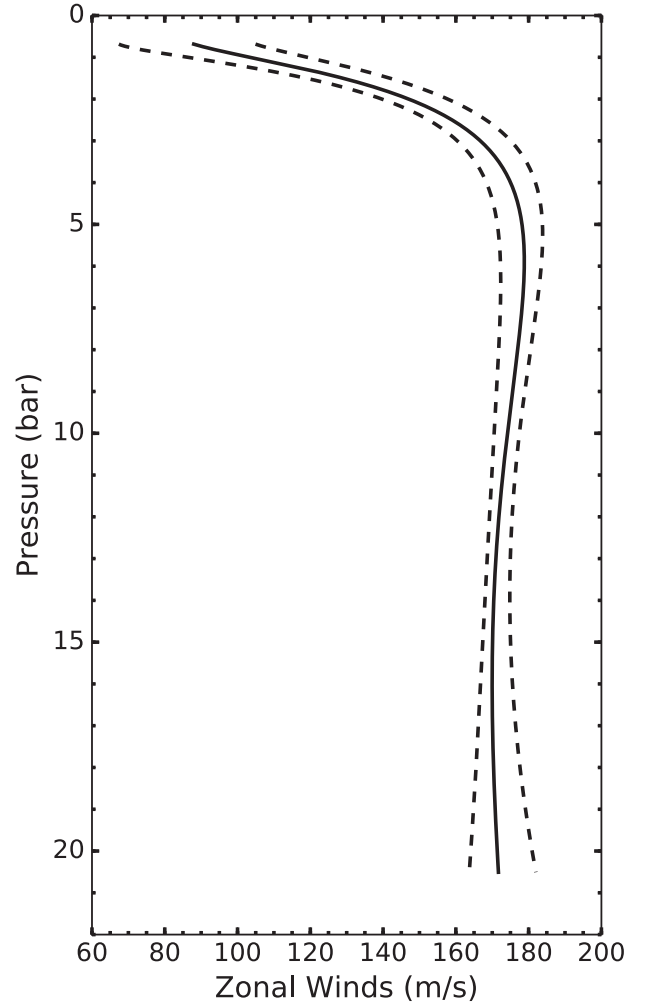


**Fig. 2.** Zonal wind velocity vs. pressure (solid black line) with an error envelope (dashed black line) as measured by the *Galileo* probe and the Doppler Wind experiment, taken from Atkinson et al. (1998). At  $P > 13$  bar, the measured wind shear and its uncertainties are consistent with zero wind shear.

and totally self-consistent picture of what hot spots and dark spots are, but there are strong qualitative similarities in several analyses and models of these features (Allison, 1990; Ortiz et al., 1998; Showman and Dowling, 2000; Friedson, 2005). Specifically, the cloud patterns and temperature and density anomalies of the hot spots are created by local, isolated downdrafts of nonlinear trapped equatorial Rossby waves. In this scenario, the Rossby waves circumscribe the entire planet with wavelengths of  $2\pi r_0/m$ , where  $m$  is the average number of hot spots ( $6 \leq m \leq 13$ ), which can vary as a function of time. This downdraft, although weak, clears out the upper aerosols that scatter sunlight back to us, resulting in the signature dark spots at visible wavelengths (Orton et al., 2017). The relatively aerosol-free, low opacity upper region allows the warmer low layers to be observable and appear as  $5 \mu\text{m}$  hot spots. Ortiz et al. (1998) and Friedson (2005) support their scenario in a number of ways, including showing that the observed numbers of dark/hot spots are consistent with the theoretical wave numbers of the Rossby waves and that the observed drift rates of the dark/hot spots are consistent with the theoretical westward phase speeds of Rossby waves with respect to the local zonal flow. In addition, the observed variability of the number of dark/hot spots as a function of time is consistent with the dispersion relationship of equatorial Rossby waves. Further, more recent support for this scenario is provided by Bjoraker et al. (2015), who show, based upon radiative transfer models that fit Keck observations, that hot spots are dry, and contain no opaque clouds between 2 and the 7 – 8 bar level. In addition, an analysis of microwave observations (Sault et al., 2004; de Pater et al., 2016) also show that hot spots have depleted mixing ratios of ammonia down to the 8-bar level, similar to *Galileo* Probe Mass Spectrometer measurements (Wong et al., 2004). The upwelling branch of the wave, displaced equatorward from the downwelling branch, as simulated by Showman and Dowling (2000), was shown to be ammonia-rich by de Pater et al. (2016).

The scenario that the hot spots are due to a Rossby wave is important in our analysis because the EQTWE relates the vertical wind shear *approximately averaged over all longitudes*, rather than at a single isolated longitude, to the meridional temperature gradient similarly averaged.<sup>3</sup> If the wind shear measured by the *Galileo* probe were a peculiarity of a local hot spot and did not represent the long longitudinal wavelength component or longitudinal average of the zonal wind shear, then we could not apply the EQTWE to the probe's measurements. Note that our analysis uses only the longitudinally-averaged meridional temperature profiles shown in Fig. 1 and only makes predictions about longitudinally-averaged temperatures. Whether or not a hot spot has a thermal or a compositional anomaly compared to the longitudinally-averaged values is irrelevant to our analyses. Our scenario only assumes that the probe-measured zonal wind shear is representative of the longitudinally-averaged values, and this is the same assumption that Friedson (2005) uses in his model.

Vertical wind profiles in Jupiter are not experimentally known except in the probe entry site. Many interpretations of hot spots share our assumption that wind shear within these features is the same as the zonal average wind shear (Allison, 1990; Ortiz et al., 1998; Friedson, 2005). One exception is by Showman and Dowling (2000), who argued that the strong wind shear seen from 1 to 5 bars in the *Galileo* probe data was strongly affected by local conditions (such that the wind shear would have been different had the probe entered elsewhere in the equatorial region). Application of our EQTWE would be invalid under these conditions. To test the robustness of the locally anomalous winds from the Showman and

Dowling (2000) model, we measured horizontal winds in a hot spot observed in 2017. Fig. 3 compares hot spot velocities from Hubble Space Telescope observations (shading in top row) and infrared images at  $4.68 \mu\text{m}$  from the Gemini North observatory (bottom row).

The 2D velocity field, extracted with ACCIV<sup>4</sup> (Asay-Davis et al., 2009), is qualitatively similar to the observed velocities from *Galileo* Orbiter data shown by Showman and Dowling (2000) in their Fig. 1. In particular, a large area of clockwise circulation is found to the south and east of the hot spot, just as in our Fig. 3. However, their model velocity field shows a clockwise circulation just to the south of the model hot spot (or about  $180^\circ$  out of phase), which leads them to find 40-m/s winds near the 1-bar level in their simulated probe entry location. This is the basis for their hypothesis that vertical wind shear in the probe region is anomalous. However, since observations differ from the horizontal velocity field in their model, it is conceivable that their conclusions regarding the vertical wind profile also differ.

In Fig. 4, we compare mean eastward winds in the region surrounding the hot spot in Fig. 3, spanning  $310\text{--}345^\circ\text{W}$ , with zonal wind measurements taken about a year earlier (Tollefson et al., 2017). There is strong agreement, suggesting that the zonal winds in and around the hot spot are highly similar to the longitudinally-averaged eastward flow.

In an analysis subsequent to the publication of Showman et al.'s hot spot model, Li et al. (2006) used cloud-tracking at two different cloud decks to measure zonal velocities in and around the spots. Within a hot spot and at the lower cloud deck at  $\sim 3$  bar, the zonal winds were  $\sim 170$  m/s, consistent with the values measured by the *Galileo* probe. Li et al. could not measure the zonal velocity within the hot spots at the altitude of the visible upper cloud decks (due to a lack of cloud tracers), but they found that the zonal velocity immediately surrounding the hot spots was  $\sim 100$  m/s, which is consistent with observed drift rates of the hot spots themselves (Ortiz et al., 1998; Friedson, 2005). All of these observations suggest, but do not prove, that the zonal velocities within the hot spots do not differ from the longitudinally-averaged zonal velocities at the latitudes at which they are located, and we use this hypothesis throughout the remainder of this section.

### 3.2. Equatorial wind shear above 500 mbar and the stratospheric jet

In this Section, we use the EQTWE with CIRS measurements at altitudes above 500 mbar to determine the equatorial wind shear and zonal velocities. The EQTWE can provide the shear, but to determine the velocity it is necessary to integrate the shear and therefore have a known reference value of the equatorial velocity at a known altitude. The *Galileo* probe provides velocities at known altitudes, but these velocities are at  $7.46^\circ\text{N}$  jovigraphic. Unfortunately, zonal velocity profiles obtained by cloud displacements, regardless of whether they use 1D correlation, 2D correlation, or discrete feature tracking (c.f., see Table 1 in Tollefson et al., 2017), all show that the difference between the zonal velocity at the equator and at  $7.46^\circ\text{N}$  differ by  $\sim 30\%$ , or 24 m/s, so we cannot use the *Galileo* probe velocities to establish a reference value. Zonal velocities determined by numerous cloud displacement studies (c.f., Tollefson et al., 2017) provide equatorial velocities that are all nearly the same; however, those studies report that the velocities are at “cloud level”. In principle, the “cloud level” could be determined, in terms of a specific altitude, by calculating contribution

<sup>3</sup> This is because the fractional errors in the EQTWE listed in the footnote in Section 4.1 are small only if  $L_\phi$  is of order or larger than  $r_0$ .

<sup>4</sup> The velocity field used input maps sampled at  $0.05^\circ/\text{pixel}$ , with final pass correlation box sizes of 50 pixels and a search range of 5 pixels. The final pass was the 4th ACCIV pass with 10-hour separations, following three short-separation (35–45 min) passes, where the first pass used 70-pixel boxes with a range of 20 pixels, providing sensitivity to any velocities up to a maximum of 440 m/s.

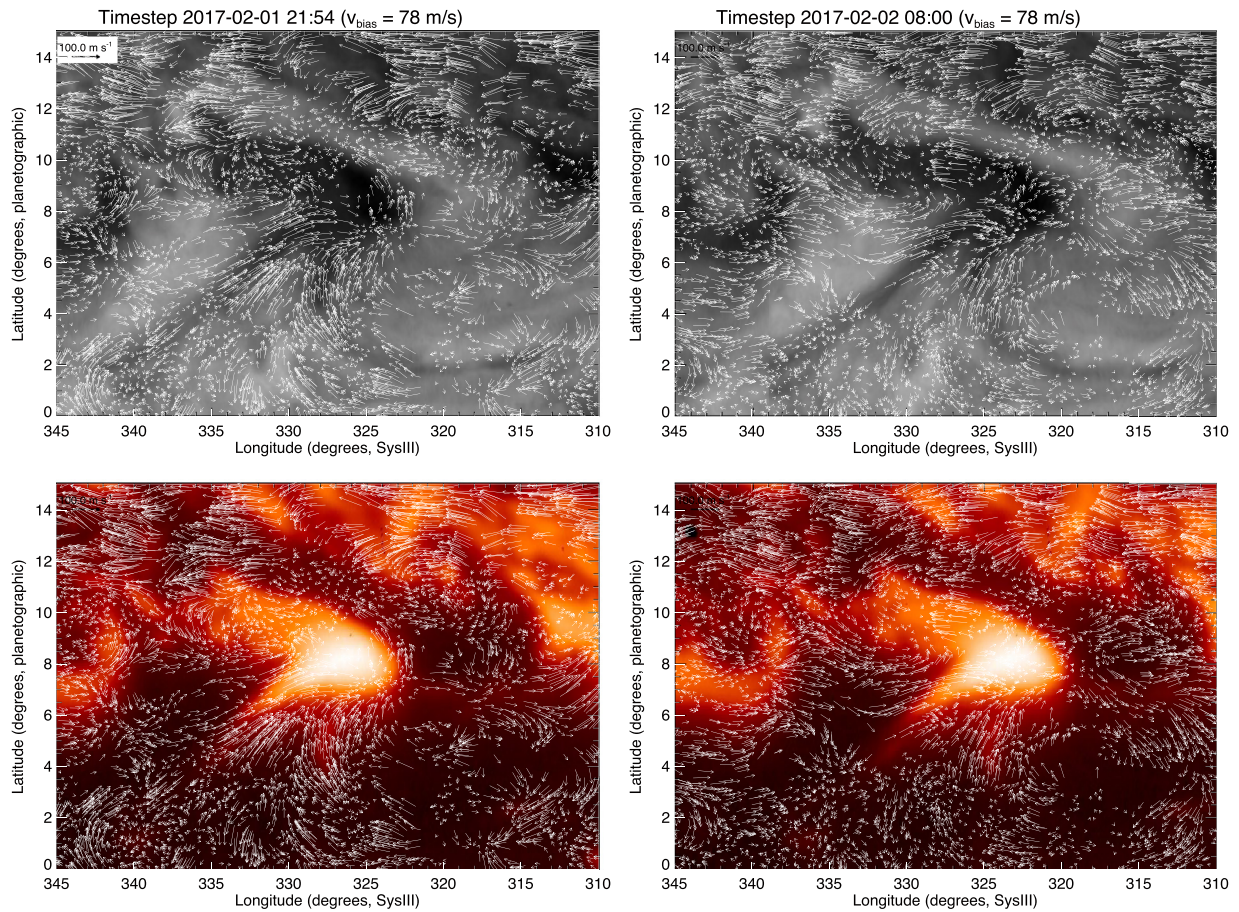


**Fig. 3.** Top row: Hubble Space Telescope WFC3/UVIS imaging data from Feb. 1–2, 2017, at 631 nm with wind vectors overlaid. Bottom row: The same wind field is compared with Gemini infrared image taken at 2017-02-01 UT 16:32. Comparison shows a strong correspondence between optically dark regions and 5  $\mu\text{m}$  bright regions, as in Orton et al. (2017). Two time steps are shown, based on 10-hour separated data processed using ACCIV (Asay-Davis et al., 2009). Time steps listed at the top of each column correspond to the midpoint of the 10-hour separated data, which is the time corresponding to the velocity field as measured, rather than the time of individual observations. Arrows show velocity vectors after the subtraction of a constant eastward velocity of 78 m/s to facilitate a comparison with vectors plotted in Showman and Dowling (2000). The Gemini data are from a single image, which was advected by a uniform velocity over the whole map area of 108 m/s eastward to match the time steps of the velocity fields. Gemini data are still under analysis for publication, but a preliminary data frame is shown here to demonstrate the strong anti-correlation between optical albedo and thermal emission.

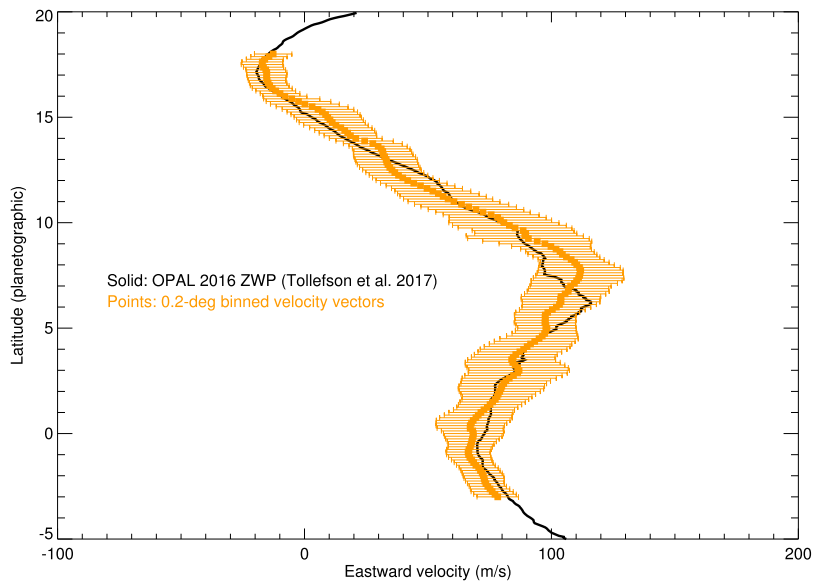


**Fig. 4.** No significant difference is seen between the longitudinally-averaged zonal winds from Tollefson et al. (2017) (black curve), and the mean eastward velocities in the velocity field in and near the hot spot in Fig. 3 (orange curve). Error bars show the standard deviation of individual vectors in each bin. A velocity of 40 m/s at a latitude of 5°N, as given by the model of Showman and Dowling (2000), is inconsistent at the 4.9-sigma level with the distribution of observed mean velocities at this latitude. At the actual latitude of the probe site, the difference is 3.9 sigm a. (For interpretation of the references to color in this figure legend, the reader is referred to the web version of this article.)

functions by assuming a model atmosphere and using radiative transfer models to compute opacities (c.f., Fig. 16 in Tollefson et al., 2018 which shows contribution functions for Neptune; and de Paater et al., 2016 which shows contribution functions for Jupiter at radio wavelengths, where the decrease in  $\text{NH}_3$  gas signifies the cloud base, e.g.,  $\text{NH}_4\text{SH}$ ,  $\text{NH}_3$ -ice). However, for Jupiter there is no definitive altitude of the cloud features used in the derivation of the wind profile, and estimates vary between 500 mbar (c.f., Flasar et al., 2004) and 1.5 bar (the tops of  $\text{NH}_4\text{SH}$  clouds). Therefore to establish the pressure for “cloud level”, we used an equatorial zonal velocity of  $76.7 \pm 5$  m/s from the cloud displacement study of Garcia-Melendo and Sánchez-Lavega (2001) because that study used images that were taken near the time of the *Galileo* probe entry at the “cloud level”. From this same study, we used the value of  $101 \pm 10$  m/s for the zonal velocity at the probe entry latitude. The *Galileo* probe data (Fig. 2) show that a velocity of 101 m/s corresponds to an altitude of 950 mbar. Using the upper and lower bounds of the probe velocities shown by the dashed lines in Fig. 2, we argue that the reference altitude is 950 mbar bounded above and below by 1.2 bar and 680 mbar. Therefore, we use as a reference point an equatorial velocity of  $76.7 \pm 5$  m/s at an altitude of  $950 \pm 250$  mbar. The uncertainty in the *Galileo* probe velocities dominate the uncertainty in determining the cloud level, so we base our estimates of the uncertainty of the reference altitude on the uncertainty that arises from the probe velocity uncertainties in Fig. 2 rather than on the smaller uncertainties in the velocities obtained from the cloud displacement study.

In addition to a reference velocity and altitude, to compute the zonal velocity at the equator, equatorial zonal velocity shears must be obtained with the EQTWE, which, in turn, requires calculating the second derivative of the mirror-symmetric component of the temperature  $\partial^2 T^M(P, \theta)/\partial\theta^2|_{\theta=0}$ . We do this with a least-squares fit of the temperature data in each panel of Fig. 1. Near the equator, we fit  $T^M(P, \theta)$  (which, by definition, is an even function of  $\theta$ ) to a parabola that is symmetric with respect to  $\theta = 0$ , so

$$T^M(P, \theta) = T^M(P, \theta = 0) + c\theta^2 \quad (16)$$

$$= T^M(P, \theta = 0) + \frac{\partial^2 T^M(P, \theta)}{\partial\theta^2}\bigg|_{\theta=0} \frac{\theta^2}{2}. \quad (17)$$

We emphasize that  $c \equiv \partial^2 T^M(P, \theta)/\partial\theta^2|_{\theta=0}/2$  because the reason for the least-squares fit is to determine the observed value of  $\partial^2 T^M(P, \theta)/\partial\theta^2|_{\theta=0}$ . To do the least-squares first, we first fold the temperature values  $T(P, \theta)$  in Fig. 1 about the equator to obtain the values of  $T^M(P, \theta)$  shown in Fig. 5. The values of the longitudinally-averaged, mirror-symmetric shears  $\partial v_\phi^M/\partial r$  at the equator are determined from these temperature fits and the EQTWE in Eq. (10), or in writing the shear in terms of  $\ln P$ ,

$$\frac{\partial v_\phi^M}{\partial \ln P} = -H \frac{\partial v_\phi^M}{\partial z} = \frac{R}{r_0 f_0} \frac{\partial^2 T^M}{\partial \theta^2}\bigg|_p, \quad (18)$$

where all quantities in the equation above are to be evaluated at the equator, and where  $H \equiv RT/g$  is the local pressure scale height and  $R$  is the specific gas constant for the Jovian atmosphere. The shears are shown in Fig. 6.<sup>5</sup>

<sup>5</sup> The fractional errors in the shear are equal to the fraction errors in determination of  $\frac{\partial^2 T^M}{\partial \theta^2}\bigg|_{P, \theta=0}$ . Using the absolute error bars of any individual temperature measurement in Fig. 1 would make a derivative or a second derivative of the temperature have errors of order unity. However, taking the temperature measurements as a group, we argue that fitting a parabola through them gives a quantitatively significant way of determining second derivative of the temperature. Estimating the

The zonal mirror-symmetric velocity is determined by integrating the vertical velocity shears at the equator and is shown in Fig. 7. The symbols in the figure are the velocities at  $v_\phi^M(\ln P_i)$  at  $P_0$  (solid squares, the reference pressure, which is 950 mbar for the black (and 1.2 bar and 680 mbar for the gray curves), each with a velocity of 76.7 m/s),  $P_1 = 330$  mbar,  $P_2 = 220$  mbar,  $P_3 = 100$  mbar,  $P_4 = 10$  mbar,  $P_5 = 5$  mbar,  $P_6 = 2$  mbar, and  $P_7 = 1$  mbar. The vertical shears,  $d v_\phi^M/d(\ln P)\big|_i$ , are known at each value of  $P_i$  by the EQTWE in Eq. (18) for  $1 \leq i \leq 7$ . For  $i = 0$ , the shear can be obtained by differentiating the velocity determined by the *Galileo* probe (but see the next footnote). To obtain the values of  $v_\phi^M(\ln P_i)$  from its shear or vertical derivative, we integrate  $d v_\phi^M/d(\ln P)$  in  $(\ln P)$  using the trapezoidal rule, or

$$v_\phi^M(\ln P_{i+1}) \equiv v_\phi^M(\ln P_i) + \frac{[(\ln P_{i+1}) - (\ln P_i)]}{2} \left( \frac{d v_\phi^M}{d(\ln P)}\bigg|_{P_i} + \frac{d v_\phi^M}{d(\ln P)}\bigg|_{P_{i+1}} \right), \quad (19)$$

with  $i = 0$ . Because the shears  $v_\phi^M(\ln P_i)$  are known for all  $i$ , once  $v_\phi^M(\ln P_i)$  has been found, the value of  $v_\phi^M(\ln P_{i+1})$  can be determined. Using the trapezoidal rule in this fashion, we have computed the values of  $v_\phi^M(\ln P_i)$  and plotted them as open circles in Fig. 7 for  $i \geq 1$ . To compute the continuous curves that connect the open circles in Fig. 7, rather than use a curve fitting subroutine, we use the trapezoidal rule for consistency: Eq. (19) is equivalent to finding  $v_\phi^M(\ln P_i)$  by drawing the quadratic curve in  $(\ln P)$  that passes through the point  $(v_\phi^M(\ln P_i), (\ln P_i))$  that has slopes  $d v_\phi^M/d(\ln P)\big|_{P_i}$  and  $d v_\phi^M/d(\ln P)\big|_{P_{i+1}}$ , respectively, at  $\ln P_i$  and  $\ln P_{i+1}$ . The value of  $v_\phi^M(\ln P_{i+1})$  in Eq. (19) is the value of this quadratic curve at  $\ln P_{i+1}$ . Each continuous curve in Fig. 7 is the union of the quadratic curves between  $\ln P_{i+1}$  and  $\ln P_i$  constructed in this manner. This method of construction makes each curve and its derivative continuous in  $(\ln P)$ .<sup>6</sup> As mentioned in the

uncertainty in the second derivative cannot be determined by examining the distance between the observational points (squares and circles) in Fig. 5 and the best-fit parabola because all of the observational points are either in the northern or southern hemisphere. Therefore, none of those points will lie on the curve of  $T^M(P, \theta)$  for fixed  $P$ , so even if the best-fit parabola exactly represented  $T^M$ , the observational points would not lie on the parabola (unless  $T^A = 0$ ). One possible estimate of the uncertainty could be made by varying the range in  $\theta$  over which a parabola is fit. Changing the range from  $|\theta| \leq 5^\circ$  to  $|\theta| \leq 10^\circ$  in panels a–g in Fig. 1, fractionally changed the values of  $\partial^2 T^M/\partial\theta^2$  by 20%. However, we believe that the range  $|\theta| \leq 5^\circ$  has too few points to carry out a proper best-fit, and therefore we think that 20% severely overestimates the fractional error of  $\partial^2 T^M/\partial\theta^2$ . Many studies have used temperatures with the TWE to estimate velocity shears. Unfortunately, neither the algorithms for computing  $\partial T^M/\partial\theta$  nor their uncertainties are typically published, so we have no way of comparing our fractional errors to those of previous studies. For panel h in Fig. 1, varying the range of  $\theta$  made a very large change in the value of  $\partial^2 T^M/\partial\theta^2$ . Therefore, we chose not to use temperatures at 500 mbar to compute the velocity shear or the velocity. (See the next footnote in this section.) Possibly, the measurements at 500 mbar have a large uncertainty due to aerosol effects on the spectrum at this altitude.

<sup>6</sup> As discussed in the first footnote in Section 3.2, the temperatures at 500 mbar (the lowest altitude at which the CIRS temperatures were reported by Fletcher et al., 2016) were considered to be too noisy to use. Therefore, we decided not to use the temperatures and the shear determined from them using the EQTWE at 500 mbar. The value of  $v_\phi^M$  plotted at 500 mbar in Fig. 7 with the open square is the value at 500 mbar of the quadratic curve connecting  $(\ln P_0)$  (the solid square) and  $(\ln P_1)$  at 330 mbar that was constructed with the trapezoidal rule. The value of the shear that we plotted with an open square in Fig. 6 at 500 mbar is “reverse engineered”; it is the value of the derivative of the quadratic curve connecting  $(\ln P_0)$  and  $(\ln P_1)$  in Fig. 7 that was constructed with the trapezoidal rule. We used this shear value at 500 mbar with the EQTWE (and the value of  $T(P = 500 \text{ mbar}, \theta = 0)$  in panel h, Fig. 1) to determine the value of  $\partial^2 T_M(P, \theta)/\partial\theta^2\bigg|_{P=500 \text{ mbar}, \theta=0}$ . We then used this

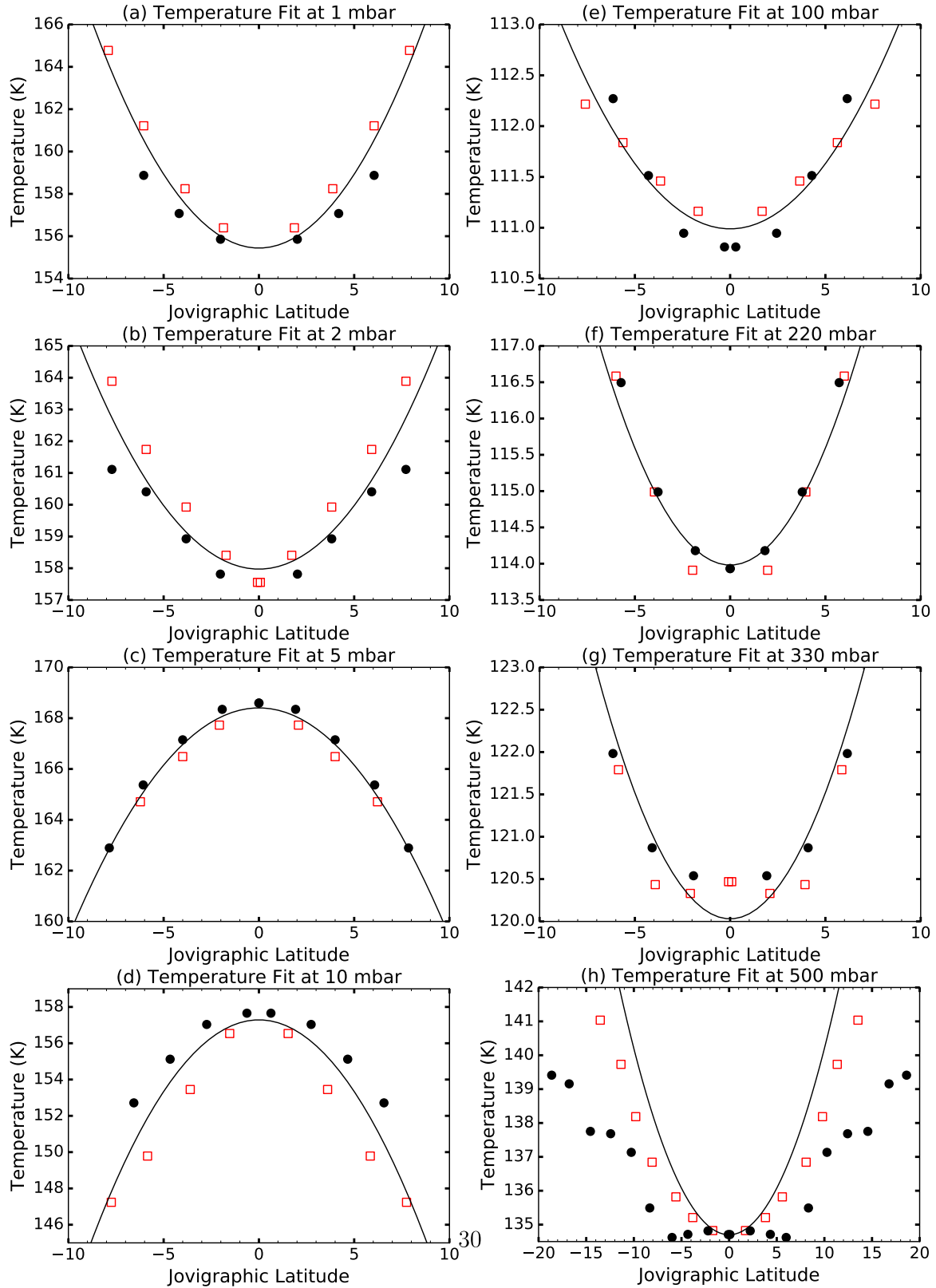


**Fig. 5.** Least-squares fits (solid line) to the temperature data in Fig. 1 with a parabola symmetric about the equator. The data in Fig. 1 are folded about the equator to provide the mirror-symmetric component of temperature  $T^M$ . Solid black circles (open red squares) are the temperature data in the northern (southern) hemisphere. The fits only use the temperatures at latitudes  $|\theta| \leq 10^\circ$  jovigraphic to assure a local fit to the equator. As explained in the text, the parabola in panel h is not determined from a least-squares fit, but rather, “reverse-engineered” from the shear at 500 mbar.

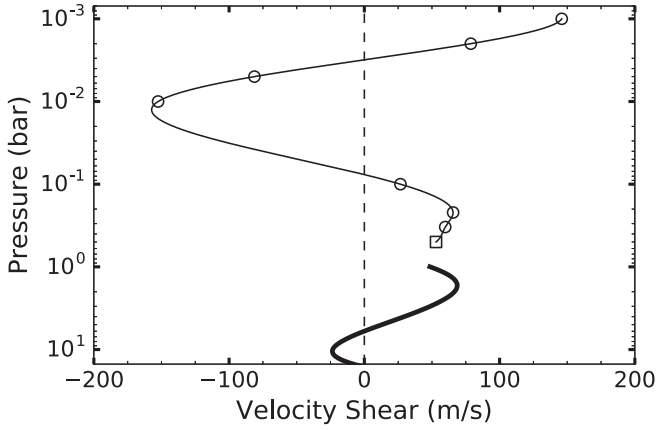


**Fig. 6.** The velocity shear  $\partial v_\phi^M / \partial \ln P \equiv -H \partial v_\phi^M / \partial r$  as a function of altitude, where  $H$  is the vertical pressure scale height, approximately 27 km at 1 bar. The open circles are the values of the shear at the equator obtained from the EQTWE applied to the temperatures in panels a–g in Fig. 5. The open square at 500 mbar is its “reverse-engineered” shear value at the equator described in the text. The thin line through the open circles and square is to “guide the eye”. The shear shown by the thick curve is the vertical derivative of the zonal velocity from the *Galileo* probe shown in Fig. 2 at latitude 7.46°N (jovigraphic). There is no physical reason why the thick and the thin curves should smoothly join together because they are at different latitudes; however, as discussed in the text, it appears that the vertical shears of the zonal velocities may be nearly independent of latitude. The top altitude shown in the thick curve is the “reference altitude” defined in the text.

footnote following Eq. (100) at pg. 80, rather than use the EQTWE in Eq. (10), there is an alternate form of the EQTWE that can be used to evaluate  $\frac{\partial v_\phi^M}{\partial r}$  that does not have any fractional errors involving  $[T^A]/[T^M]$ :

$$\frac{\partial v_\phi^M}{\partial r} = -\frac{g'}{r f_0 T^M} \left[ \frac{\partial^2 T^M}{\partial \theta^2} \Big|_P - \frac{1}{T^M} \left( \frac{\partial T^A}{\partial \theta} \Big|_P \right)^2 \right], \quad (20)$$

where all quantities and their derivatives are computed at the equator. In principle, the quantities on the right side of Eq. (20) can be determined from the temperature in Fig. 1. Curve-fitting the data with parabolas that are not constrained to be symmetric yield values of  $T^M$  and  $\frac{\partial^2 T^M}{\partial \theta^2}$  such that the values are much larger than their uncertainties. However, curve-fitting does not give reliable values of  $\frac{\partial T^A}{\partial \theta}$  at the equator because the values of these terms are smaller than their uncertainties. Therefore, it is better to use the EQTWE in Eq. (10), forego the seemingly more accurate Eq. (20), and accept the fact that Eq. (10) has a fractional error of order  $\{[T^A]/[T^M]\}^2$ .

value of the temperature’s second derivative and the value of  $T(P = 500 \text{ mbar}, \theta = 0)$  in panel h, Fig. 1 to create, or “reverse-engineer”, a new parabola (symmetric about the equator as in Eq. (17)). This reverse-engineered parabola is shown in panel h, Fig. 5. This parabola does a good job fitting the two temperature values nearest the equator, but does a poor job far from the equator. Perhaps this is not a surprising finding considering the noisy data and the fact that the parabolic approximation of the temperature profile is only valid close to the equator. Finally, we note that we might have been incautious in determining the value of the vertical shear of  $v_\phi^M$  at the equator by using the *Galileo* probe data because the latter was taken at jovicentric latitude 6.53°N (7.46°N jovigraphic), rather than  $\theta = 0$ . To check the validity of estimate of the vertical shear at the equator, we constructed a new quadratic curve as a function of  $(\ln P)$  for  $v_\phi^M$  at the equator by connecting data at  $(\ln P_0)$ ,  $(\ln P_1)$ , and  $(\ln P_2)$  such that  $v_\phi^M$  at  $(\ln P_0)$  is 76.7 m/s, and the vertical shear at  $(\ln P_1)$  and  $(\ln P_2)$  are the values of the vertical shear determined from the temperature by the EQTWE. This quadratic curve in  $(\ln P)$  is nearly indistinguishable from the curve plotted in Fig. 7. The closeness of these two curves shows that at cloud level, the vertical shear of the azimuthal velocity at the equator and at jovicentric latitude 6.53°N are nearly the same, despite the fact that the azimuthal velocity itself differs substantially at these two latitudes. See Fig. 9.

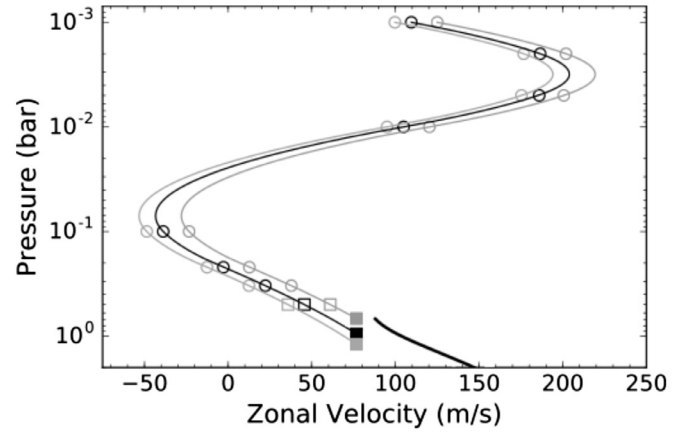


**Fig. 7.** The thin black curve shows the zonal velocity  $v_\phi^M$  derived with the EQTWE at the equator and by integrating the shear from Fig. 6 as a function of altitude. The thick black curve below 700 mbar shows the zonal velocity from the *Galileo* probe in Fig. 2 at a jovigraphic latitude 7.46° N, rather than at the equator. The open black square and open black circles are at the same altitudes as they are in Fig. 6, and the slope of the thin black curve at each open circle is equal to the shear at the corresponding open circle in Fig. 6. The black solid square at 950 mbar is at the reference altitude or “cloud level” (see text), and its value was set equal to the zonal velocity that was determined from cloud displacements (García-Melendo and Sánchez-Lavega, 2001) at the “cloud level”. The thin continuous curve that connects the black symbols and the open black symbols themselves were computed by integrating the velocity shears with the trapezoidal rule (see text). The gray curves, open circles, open square, and solid square plotted to the right and left of their black counterparts correspond to the same values as their black counterparts, with the exception that the reference altitude for the “cloud level” is 680 mbar or 1.2 bar. The stratospheric jet near 3 mbar has a peak westward velocity of  $\sim 205$  m/s when the cloud level is set to 950 mbar. In general, the velocity of the stratospheric jet increases with decreasing altitude of the cloud level reference altitude.

Figs. 6 and 7 show that the vertical wind shear remains at the large negative value that was measured by the *Galileo* probe at  $P = 685$  mbar up to altitudes of  $P \approx 200$  mbar and then becomes positive at a value of  $P$  between 10 and 100 mbar (i.e., just above the tropopause, in the stratosphere), and changes sign and becomes negative again at  $P$  between 2 and 5 mbar. In fact, because the EQTWE in Eq. (10) shows that the wind shear is directly proportional to  $\partial^2 T / \partial \theta^2$ , these comments about the wind shear above 500 mbar are obvious by a casual inspection of Fig. 1.

The stratospheric equatorial jet shown in Fig. 7 is centered near an altitude of 3 mbar and has a vertical thickness of  $\sim 20$  km. According to Figs. 1 and 5, it has a meridional width of  $\sim 20^\circ$  or  $\sim 25,000$  km. It has a maximum eastward-going velocity of  $\sim 205 \pm 15$  m/s. To understand our estimate of the uncertainty of the jet speed, note that the uncertainty in the altitude of the reference altitude at “cloud level” has an effect on the velocity because the velocity is an integral of the zonal shear that starts at the reference velocity and altitude. A change in the reference velocity of  $\pm 5$  m/s will simply shift the zonal velocity plotted in Fig. 7 by  $\pm 5$  m/s. A change in the reference altitude by  $\pm 250$  m/s will have a bigger effect. The two thin gray curves in Fig. 7 show the effects of changing the reference altitude from 950 mbar to 1.2 bar and 680 mbar (the lower and upper limits on the cloud level altitude as determined from the uncertainty in the *Galileo* probe velocity measurements), respectively, while keeping the “cloud level” zonal fixed at 77 m/s. Lowering the reference altitude increases the maximum velocity of the stratospheric jet. The uncertainty of the stratospheric jet speed,  $\pm 15$  m/s is based on the uncertainty in the reference altitude, which is larger than the uncertainty in the jet speed due to the uncertainties in the reference velocity. (Here, we do not consider the effect of the uncertainties in the zonal wind shears obtained via the EQTWE due to the difficulty in obtaining a reliable measure of the uncertainties in  $\partial^2 T / \partial \theta^2$ ).

### 3.3. Application of the EQTWE to the Galileo probe

Little is known about the temperature profiles at altitudes below 700 mbar, because infrared temperature measurements cannot typically be done at these depths. Thus, we wish to use the EQTWE to determine the meridional temperature profile at the depths where the *Galileo* probe took measurements (0.7–21 bar). Using the EQTWE in Eq. (10) to express the second derivative  $\partial^2 T^M / \partial \theta^2$  in terms of the zonal shear  $\sigma(P) \equiv \partial v_\phi^M / \partial r$  at the equator, which is defined to be the longitudinal average of  $\partial v_\phi^M / \partial r|_{\theta=0}$ , and approximating  $T^M(P, \theta)$  as a parabola symmetric about the equator, as in Eq. (17), then near the equator:

$$T^M(P, \theta) = T(P, 0) [1 - r_0 f_0 \sigma / (2g') \theta^2]. \quad (21)$$

Note that  $T(P, 0) \equiv T^M(P, 0)$ . Fig. 1 shows by direct observation that at altitudes corresponding to  $P \leq 500$  mbar, that there are local extrema of  $T^M$  at the equator, so  $\sigma \neq 0$ . A convenient way to express the magnitudes of these extrema is Fig. 8, which shows  $\Delta T(P) \equiv [T(P, 0) - T^M(P, \bar{\theta})] / T(P, 0)$ , where  $\bar{\theta}$  is a reference latitude that we set to  $7.46^\circ$  jovigraphic. From Eqs. (17) and (21), we see that  $\Delta T(P)$  and the equatorial zonal shear  $\sigma$  and  $dv_\phi / d \ln P|_{\theta=0}$  are related by :

$$\begin{aligned} \Delta T(P) &= \bar{\theta}^2 r_0 f_0 \sigma / (2g') = -\frac{\bar{\theta}^2 r_0 f_0}{2g'} \frac{dv_\phi}{d(\ln P)} \frac{1}{H} \\ &= -\frac{\bar{\theta}^2 r_0 f_0}{2RT(P, 0)} \frac{dv_\phi}{d \ln P}. \end{aligned} \quad (22)$$

Using Eq. (22), we obtain values of  $\Delta T(P)$  from values of  $dv_\phi / d \ln P|_{\theta=0}$ , where the latter are obtained by differentiating the zonal velocity in Fig. 2.

From the *Galileo* probe we have values of the shear at  $7.46^\circ N$ , rather than at the equator where the EQTWE requires them. Although the zonal velocities at  $7.46^\circ N$  and the equator are quite different, Fig. 9, which is a blow up of Fig. 7 near the reference altitude of 950 mbar, shows that the values of the zonal velocity shear at  $7.46^\circ N$  and the equator are quite similar (differing by less than 2%). In particular, at 950 mbar, the value of the vertical shear at  $7.46^\circ N$  (as determined by differentiating the *Galileo* probe velocity) gives a shear value for  $\partial v_\phi / \partial \ln P$  of 44.5 m/s per  $\ln P$ , or equivalently, a shear value for  $\partial v_\phi / \partial r$  of  $-1.91$  (m/s)/km. At 950 mbar, the value of the vertical shear at the equator (as determined with the temperature observations at the equator and the EQTWE) gives a shear value for  $\partial v_\phi / \partial \ln P$  of 43.8 m/s per  $\ln P$ , or equivalently, a shear value for  $\partial v_\phi / \partial r$  of  $-1.88$  (m/s)/km. It is this observation at 950 mbar and our assumption that  $\partial v_\phi^M / \partial \ln P$  remains approximately independent of latitude down to altitudes of  $\sim 13$  bar, that we justify our use of the shear from the *Galileo* probe in the EQTWE.

To determine the vertical shear at 950 mbar at the equator from the EQTWE and the temperatures in Fig. 1, we did the following: because we did not feel that we had reliable temperature information at the equator for altitudes lower than 330 mbar, we used the EQTWE at 220 mbar and at 330 mbar to determine the shear at the equator, and then extrapolated these values to 950 mbar. We did the extrapolation by assuming that the zonal velocity was a parabolic function of the pressure (*n.b.*, this assumption that the velocity is parabolic in altitude has no relationship with the fact that we assumed that  $T^M$  was locally parabolic in  $\theta$ , other than a fact that that a parabola is the first three terms of a Taylor expansion). The parabola is uniquely determined by requiring that its derivatives (or velocity shears) at 220 and 330 mbar are equal to the values that we derived from the EQTWE (as shown in Fig. 6),

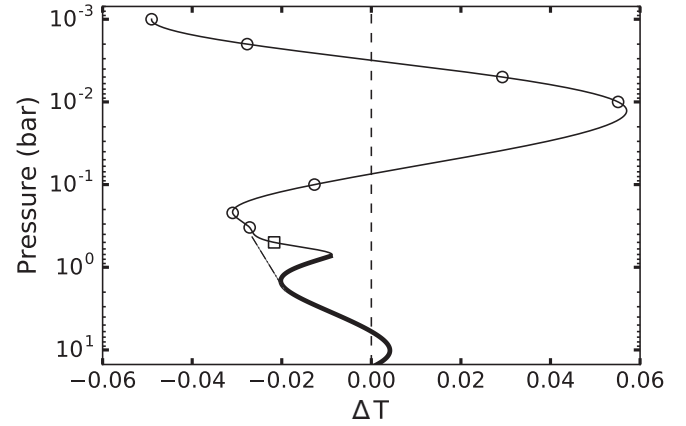


**Fig. 8.** The difference  $\Delta T \equiv [T(P, 0) - T^M(P, 7.5^\circ)] / T(P, 0)$  between the equatorial temperature and the temperature at  $7.5^\circ$  jovigraphic, normalized by the value of temperature at the equator as a function of  $P$ . The thick curve shows values determined by the EQTWE using the zonal wind from the *Galileo* probe. The equator is cool compared to its surrounding latitudes with  $\Delta T(P) < 0$  at altitudes between 1 and 5 bar; however, the equator is relatively warm with  $\Delta T(P) > 0$  at altitudes between 5 and 13 bar. The open circles are values of  $\Delta T(P)$  found by fitting the symmetric component  $T^M(P, \theta)$  of observed CIRS temperatures in Fig. 1 with a parabola that is symmetric about the equator. The open square at 500 mbar is “reverse engineered” as described in the footnote in Section 3.2. The thin curve through the open circles, open square, and connecting to the thick curve is to “guide the eye”. As explained in the text, the “kink” in the temperature between  $\sim 500$  mbar and 1.5 bar may be nonphysical due to uncertainties in the values of the *Galileo* probe wind shear. As explained in the text at the end of Section 3.3, replacing those wind shear values with a straight-line extrapolation of the wind shear at 1.5 bar would change the “kink” to the dot-dash line between  $\sim 500$  mbar and 1.5 bar.

and that the velocity at 950 mbar is the one we chose for the reference altitude (as shown in Fig. 7). Differentiating this parabola at 950 mbar gives our value for the extrapolated vertical shear at 950 mbar at the equator from the EQTWE. Throughout the remainder of this section, we make the approximation that the shear at the equator is the value of the shear measured by the probe.

The uncertainties in  $\Delta T$  are due to the fractional errors in the vertical shear of the *Galileo* probe velocity and due to our assumption that the shear at the equator and  $7.46^\circ N$  are the same. We note that the blow-up of the probe velocity in Fig. 9 shows a “hook” near 900 mbar. The difference in the velocities given by the thick curve with the hook and a new curve that is a straight extrapolation (the dot-dash line that removes the “hook”) of the curve at altitudes above 1 bar is small.<sup>7</sup> A straight extrapolation falls well within the uncertainties in the figures. However, the difference in the slope between the hooked curve and the straight extrapolation is large between 680 mbar and 1 bar, and this difference in slope creates factor-of-2 differences in the shear  $\partial v_\phi / \partial r$  of the hooked curve and the straight extrapolation (and, therefore in  $\Delta T$ ) at those altitudes. The small hook in the probe velocity’s shear in Fig. 9 near 900 mbar may be nonphysical.<sup>8</sup> Therefore, the kink in Fig. 8 at altitudes between 680 mbar and 1 bar may also be nonphysical. If we use the wind shear from the dot-dash curve (extrapolation), rather than the thick continuous curve (actual *Galileo* probe measurements), in Fig. 9 at altitudes between 500 and 1.5 bar in the EQTWE to determine  $\Delta T$ , (i.e., use the far right side of Eq. (22) to compute  $\Delta T$ , where the value of  $dv_\phi / d \ln P$

<sup>7</sup> Replacing the hooked curve with the straight-line extrapolation would make a negligible difference in the determination of the reference velocity.

<sup>8</sup> We have called into question the accuracy of the experimental velocity measurements of the *Galileo* probe at the highest altitudes where the measurements were reported. We have also called into question the accuracy of the experimental temperature measurements at the lowest altitudes where they were reported. As pointed out by Feynman and Leighton (1986), experimental data at the extreme ends of the range over which data is reported should be treated with caution.

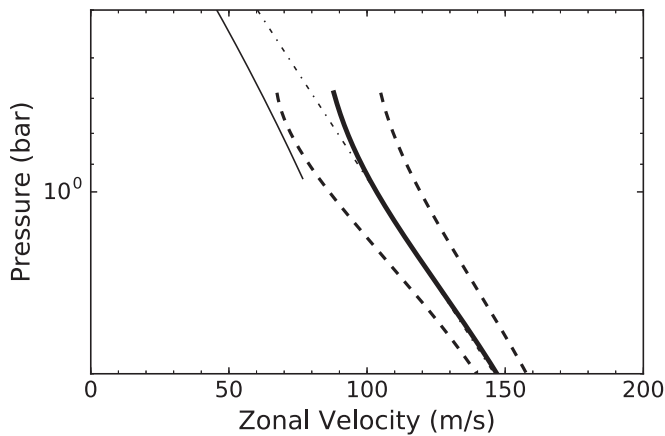


**Fig. 9.** Blow up of the lower part of Fig. 7 that is based on the reference altitude of 950 mbar. The zonal velocity  $v_{\phi}^M$  at the equator (thin continuous curve) is obtained from the EQTWE and the temperatures in Fig. 1. This part of the curve is extrapolated down to the 950 mbar altitude using the velocity shear values at 220 and 330 mbar as described in the text. The thick curve is the zonal velocity from the *Galileo* probe at 7.46°N jovigraphic. The thick dashed lines on either side of the thick curve are the dashed lines showing the probe velocity uncertainty in Fig. 2. As described in the text, we are concerned that the “hook” in the *Galileo* probe velocity at altitudes above 1 bar may be erroneous. The thin dot-dash line shown at altitudes above 1 bar would be the *Galileo* probe velocity if we replaced the “hook” with a straight-line extrapolation of the probe velocity at altitudes just below 1 bar. Although the zonal velocity at the equator and 7.46°N at 950 mbar differ, the vertical shears differ by less than 2%.

is fixed at its value at 1 bar and where we use the temperature profile given by Seiff et al. (1998) for  $T(P)$ , then the “kink” in Fig. 8 is replaced by a nearly straight line.

#### 3.4. Implications of the EQTWE-derived temperatures

Fig. 8 shows that altitudes between 1 and 5 bar, the equator is cool compared to the North and South Equatorial Belts, consistent with the temperatures at 500 mbar shown in panel h in Fig. 1. This anomalously cool region in a stably stratified atmosphere<sup>9</sup> is indicative of up-welling at the equator if the air rises adiabatically and therefore cools. Because the temperature extrema at the equator were derived from zonal shears that we assumed were representative of the winds at all longitudes, we envision that this up-welling is nearly axisymmetric around the planet and not confined to a compact location and that the up-welling is part of a larger atmospheric circulation that is also nearly axisymmetric around the planet. The formation of clouds all along the equator is also indicative of an equatorial up-welling along a moist adiabat that circumscribes the planet. On Jupiter, clouds are expected to form at least three decks: a water cloud at 5–7 bar,  $\text{NH}_4\text{SH}$  clouds at 1.5–2.5 bar, and ammonia clouds above 1 bar (Lewis, 1969; Atreya and Romani, 1985; Wong et al., 2015). In this picture of cloud formation, after up-welling at the equator, the air, now depleted of its condensibles, travels pole-ward and sinks, adiabatically warming. This picture of equatorial up-welling and cooling is also consistent with pictures of the Jovian zone-belt system dating back to at least 1969: rising motion at the central latitude of each nearly axisymmetric zone that extends all the way around the planet, and sinking motion at the central latitude of each belt (Ingersoll and Cuzzi, 1969; Barcilon and Gierasch, 1970). This picture, as shown schematically by the upper two cells in Fig. 10, applies to Jupiter’s equator, which has anticyclonic vorticity for  $|\theta| < 10^\circ$ , and is therefore a zone with the equator as its central latitude. This upper layer of cells looks

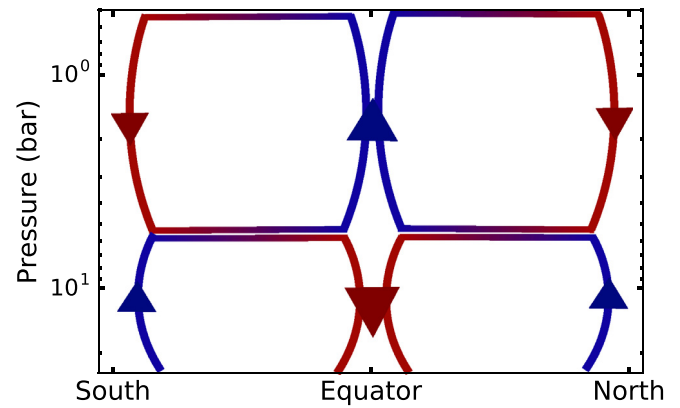


**Fig. 10.** Schematic of the proposed 2-layer cellular circulation in Jupiter’s troposphere implied by the EQTWE. For altitudes above 5 bar (and beneath the 10–100 mbar height where the equatorial temperature anomaly shifts from being cold to warm according Fig. 8, air rises adiabatically at the equator, locally cooling and drying the atmosphere. Dry air then travels pole-ward and descends down to 5 bar. At altitudes below 5 bar, this scenario is reversed. The upper layer looks similar to Earth’s equatorial Hadley cells. The flows are independent of longitude. This scenario is based on our application of the EQTWE to *Galileo* Probe wind shear data, assuming horizontal homogeneity in composition. If water vapor is inhomogeneous at  $P > 8$  bar, there may be no reversed circulation at depth.

similar to Earth’s equatorial Hadley cells. This picture of rising gas in the equatorial zone (EZ) and sinking in the north equatorial belt (NEB) was recently given credence by microwave maps constructed using the Very Large Array (de Pater et al., 2016), which showed bands, encircling the entire planet, of ammonia rising from deep levels (altitudes below  $\sim 8$  bar) up to cloud condensation levels (altitudes between 0.7 and 2.5 bar) in the EZ, a few degrees north of the equator, accompanied by descending ammonia-depleted air in the belts, in particular the NEB. Recent Juno observations of an ammonia plume (Li et al., 2017) just north of the equator during perijove passes PJ1 and PJ3 are consistent with our model in Fig. 10 as discussed below in Section 3.5.

At altitudes between 5 bar and 13 bar, the temperature anomalies in Fig. 8 show that the equator is relatively warm with respect to the surrounding air and therefore implies a circulation that is opposite to the one at altitudes above 5 bar and is illustrated by the lower layer of cells in Fig. 10. A 2-layer cellular circulation like the one in Fig. 10 was proposed earlier by Ingersoll et al. (2000). Showman and de Pater (2005) also suggested a similar scenario to explain the overall ammonia abundance depletion at altitudes above  $\sim 2$  bar and between belts and zones.

Our meridional temperature gradient has strong quantitative similarities to one case considered in Showman and Ingersoll (1998). That work attempted to use a more general, gradient-wind balance, producing estimates of the meridional temperature gradient at the Probe entry site based on the probe wind data. Gradient wind balance includes a centripetal force that depends on the curvature of the flow,  $R$ . For zonal flow, (i.e.,  $R \rightarrow \infty$ ), Showman and Ingersoll (1998) found the equator to be cooler than the probe site at altitudes above 5 bar, and warmer than the probe site at deeper levels near 10 bar. Magnitudes of the meridional temperature gradients for their zero-curvature flow case are very similar to the gradients in our Fig. 8, although we find the strongest gradient near 300 mbar and Showman and Ingersoll (1998) found the strongest gradient closer to 1.5 bar.

A final note about our use of the EQTWE in this section is that we assume that the Jovian atmosphere has a horizontally homogeneous molecular weight. By doing so, we ignore the effects of the density variations of ammonia, hydrogen sulfide, water and, other trace gases in the atmosphere, which lead to departures from Eq. (2) and the EQTWE. The density variation of an atmosphere

<sup>9</sup> We argue that the atmosphere at these altitudes is stably stratified, based, in part, by the findings of Magalhães et al. (2002).

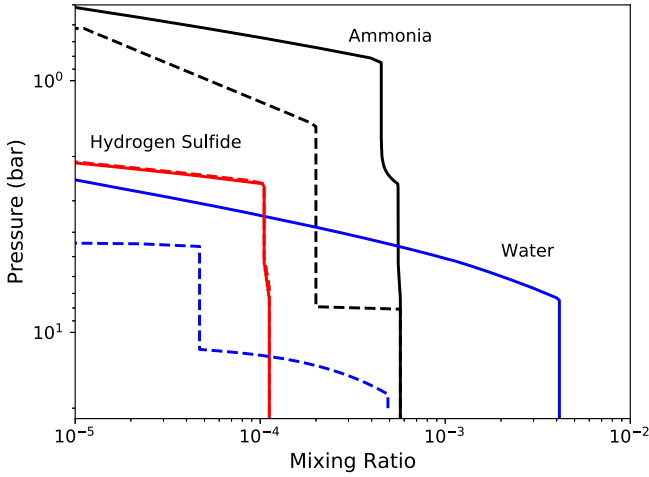


**Fig. 11.** Mixing ratio profiles of ammonia gas at the equator (solid black) and NEB (dashed black) based on radiative transfer models that fit VLA observations. The figure shows that the gases are sufficiently small that compositional effects are not important in the EQTWE, and virtual temperatures do not need to be used. The curves of water (solid blue) and hydrogen sulfide (solid red) are derived from thermochemical models assuming both are 4.5 times enhanced above solar O and S at  $P > 8$  bar (de Pater et al., 2016). The dashed blue line shows the water abundance profile in a hot spot as derived by Bjoraker et al. (2015), based upon infrared measurements that are sensitive down to the 7–8 bar level. The molecular weight is affected mostly by ammonia at  $P < 5$  bar, and mostly by water at  $P > 5$  bar, depending on the exact mixing ratio profiles. Note that at present there is no accurate measurement for water at  $P > 8$  bar. (For interpretation of the references to color in this figure legend, the reader is referred to the web version of this article.)

due to a tracer with non-spatially uniform mixing ratio, and its contribution to the vertical wind shear are accounted for by the second term on the right side of Eq. (142) in Appendix C. This term can have a large effect on the vertical wind shear. For example, Tollefson et al. (2018) found in some applications to Neptune’s atmosphere that the *sign* of the wind shear predicted by the TWE and EQTWE changes when compositional anomalies are properly accounted for. However, we believe that the compositional structure of Neptune differs from that of Jupiter with the latter having much smaller volatile mixing ratios so that the compositional effect on the vertical wind shear of Jupiter is at most a few percent of the thermal effect. To see this, note that we assume that the spatial non-uniformity of the mixing ratios of the trace gases are indicated by the difference between the mixing ratios at the NEB and at the equator in Fig. 11, which shows that the difference is important only for ammonia and potentially water at  $P > 8$  bar.<sup>10</sup> The ratio of the compositional contribution to the EQTWE (i.e., the second term in Eq. (142)), to the thermal contribution (i.e., the first term in Eq. (142)) is approximately  $\Delta m/\Delta T$ , if the characteristic meridional length scales of mirror-symmetric components of  $T$  and  $m$  are similar at the equator. Here,  $\Delta m$  is defined like  $\Delta T$ , the normalized difference between its value at the equator and at  $7.5^\circ$  jovigraphic;  $\Delta m \equiv m(\theta = 0) - m(\theta = 7.5^\circ)$ . From Figs. 8 and 11,  $\Delta m/\Delta T$  is on the order of up to 10%, so the vertical zonal shear is given by the EQTWE with a fractional error of only a few percent due to ignoring compositional effects. Note that the above is only valid at  $P < 8$  bar where we have observation constraints for  $\text{NH}_3$ ,

<sup>10</sup> The ammonia mixing ratios are determined from radiative transfer models that fit VLA data, but the water and  $\text{H}_2\text{S}$  abundances are theoretically derived from thermochemical calculations, assuming deep abundances for both (de Pater et al., 2016). It is clear, though, from these models and other data (including the *Galileo* probe data – Wong et al. (2004), that the  $\text{H}_2\text{S}$  mixing ratio is much smaller than the  $\text{NH}_3$  value, and hence will not effect the ratio  $\Delta m/\Delta T$  at altitudes above the water cloud by more than a factor of 2.

$\text{H}_2\text{S}$ , and  $\text{H}_2\text{O}$  (see Fig. 11, de Pater et al., 2016, and Bjoraker et al., 2015). An accurate measurement of water at  $P > 8$  bar is needed to evaluate its compositional contribution on the EQTWE.

### 3.5. Comparison with Juno results

Is there a relation between the ammonia plume observed by *Juno* near  $3.5^\circ\text{N}$  jovicentric as shown in Fig. 12 and the ascending and descending motions at the equator that we inferred from the EQTWE and the *Galileo* probe observations as shown in Fig. 10?

The ammonia plume shown in Fig. 12 upwells from below 8 bar (also see de Pater et al., 2016) to 800 mbar (*n.b.* ammonia condensation is believed to occur between 0.7 and 2.5 bar in the EZ) and is presumed to be anomalously cool due to adiabatic cooling. The term “plume” is somewhat misleading because the *Juno* results and de Pater et al. (2016) suggest that this ammonia “plume” extends around the entire planet with not much variation in longitude. de Pater et al. (2016) distinguish between the rising ammonia gas in the equatorial zone that circumscribes the planet, independent of longitude (referred to as “plume” above), and bonafide plumes of ammonia gas signifying the counterpart of the Rossby wave causing the well-known  $5\ \mu\text{m}$  hot spots. If we assume that the TWE is valid *qualitatively* near the plume (which is not unreasonable because Flasar et al., 2004 used the TWE at  $5^\circ$  to successfully obtain qualitative information about the equatorial stratospheric jet), then the TWE implies that on the northern or polar side [southern or equatorial side] of the cool ammonia plume that the temperature increases [decreases] with increasing latitude, and the zonal velocity decreases [increases] with increasing altitude. The latitude of the entry of the *Galileo* probe is  $6.53^\circ\text{N}$  jovicentric. Assuming that the plume is cool and applying the TWE to the *Galileo* entry site where  $v_\phi$  decreases [weakly increases] with increasing altitude between 770 mbar and 5 bar [between 5 and 13 bar], the ammonia plume would need to be south of the entry site at altitudes between 770 mbar and 5 bar but be north of the entry side between 5 and 13 bar. Despite some meandering of the plume’s central latitude with altitude, this amount of variation is not supported by Fig. 12. Thus, application of the traditional TWE to the plume is inconsistent with the *Galileo* probe measurements.

Now consider what the EQTWE implies about the cool ammonia plume and the *Galileo* probe velocity measurements. Model the temperature anomaly of the plume as a Gaussian, so that its local longitudinally-averaged temperature is

$$T(\ln P, \theta) \equiv \bar{T}(\ln P) + c e^{-(\theta-a)^2/(2\chi^2)}, \quad (23)$$

where  $\bar{T}(\ln P)$  is the average temperature as a function of depth,  $c < 0$  is the strength of the temperature anomaly (which is likely to be in the range of  $-2$  to  $-8$  K),  $a$  is the central latitude of the plume (in degrees latitude and can vary as a function of altitude, but meanders around  $3.5^\circ$ ), and  $\chi$  is the width of the rising plume (also in degrees latitude and a function of altitude). The EQTWE in Eq. (18) depends on  $T^M = \bar{T}(\ln P) + \frac{c}{2} [e^{-(\theta-a)^2/(2\chi^2)} + e^{-(-\theta-a)^2/(2\chi^2)}]$ , rather than  $T$ , and although  $T$  has a local minimum near the equator,  $T^M$  can have a local minimum (if  $a < \chi$ ) or a local maximum (if  $a > \chi$ ) at the equator. Using this  $T^M$  and the arguments in Section 3.3 that the vertical wind shear measured by the *Galileo* probe is the same as it is at the equator, the vertical velocity shears deduced from the EQTWE are qualitatively consistent with the *Galileo* observations only if  $a < \chi$  between 770 mbar and 5 bar and  $a$  is slightly larger than  $\chi$  between 5 and 13 bar. From Fig. 12, this dependence of  $a$  and  $\chi$  is possible, but the observations are not good enough to provide a definitive answer.

However, the latitudinal thickness of the plume may be too small to allow the application of either the TWE or the EQTWE.

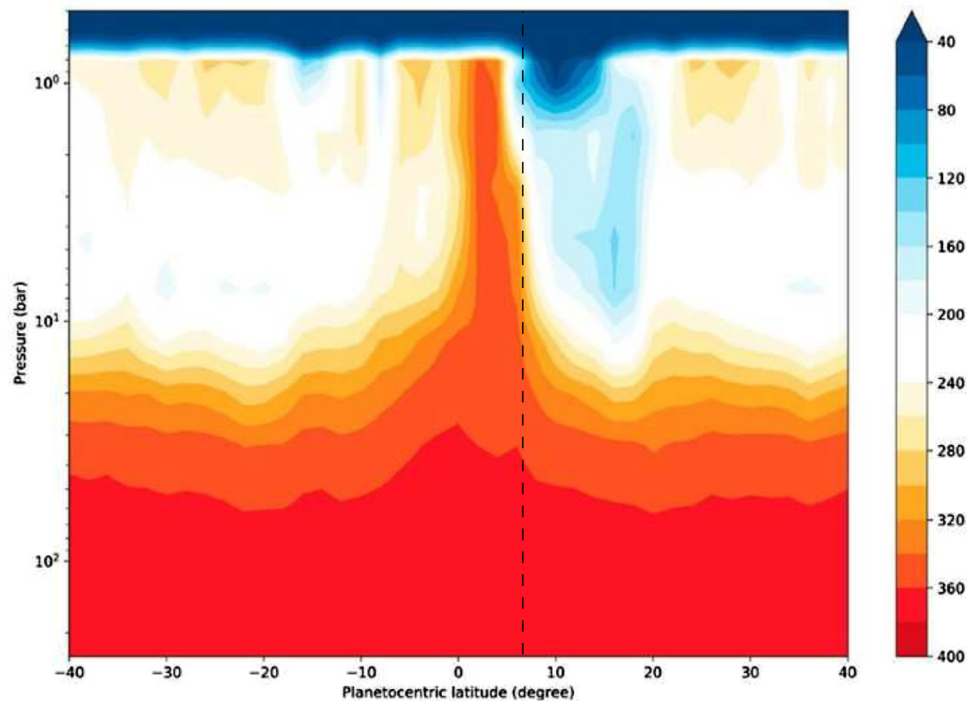


**Fig. 12.** Ammonia plume near the Jovian equator from Li et al. (2017). The colored contours show the ammonia concentration measured by *Juno* in parts per million. The vertical broken line is at the entry latitude of the *Galileo* Probe. The central latitude of the plume  $a$  would need to be south [north] of the dashed line at altitudes above [below] 5 bar to be consistent with the TWE. The latitudinal thickness  $\chi$  of the plume would need to be greater than [less than]  $a$  at altitudes above [below] 5 bar to be co-consistent with the EQTWE. The thinness of the plume may invalidate the use of both the TWE and the EQTWE. (For interpretation of the references to color in this figure legend, the reader is referred to the web version of this article.)

To see this, note that neither equation is valid unless the nonlinear advection terms involving the velocity and its derivatives are small compared to the pressure and Coriolis terms in Euler's equation (or equivalently, that the nonlinear advection terms in Eq. (36) are small compared to the pressure and Coriolis terms). The nonlinear terms are created by different velocities at different length scales, and the uncertainties in the EQTWE that we listed in expression (4) come about by requiring the main contribution to the nonlinear terms are due to large velocities of order  $V_\theta$  and  $V_\phi$  (or greater) at the large length scales of  $L_\phi$  and  $L_\theta$  (or greater). However, in any intermittent, turbulent fluid such as the atmosphere of Jupiter, there are bound to be small features such as vortices and plumes, where locally a nonlinear advection term becomes large due to the large velocity derivatives (i.e., small length scales) of the features. These local, but spatially compact, large magnitudes of the nonlinear advection terms usually do not invalidate either the TWE or the EQTWE as long as the equations are not applied directly to the regions containing these features. (In some sense, one should think of the TWE and the EQTWE as being used with temperature and velocity fields that have been averaged over lengths  $L_\phi$  and  $L_\theta$ ). Because the ammonia plume's latitudinal thickness is approximately 2500 km, which is much less than  $L_\theta$ , it might not be valid to use either the TWE or EQTWE with the plume. One interpretation of the *Galileo* probe and *Juno* plume measurements is that the longitudinally-averaged temperature at  $|\theta| \leq 10^\circ$  has two components. One is a spatially large-scale, nearly parabolic (in  $\theta$ ) flow, approximately symmetric about the equator. Between 770 mbar and 5 bar [between 5 and 13 bar], this temperature has a minimum [maximum] at the equator. Superposed on this large-scale component, there is a small-scale, cool anomaly associated with the ammonia plume near  $3.5^\circ\text{N}$  jovicentric. However, this small-scale temperature anomaly associated with the plume has no effect on the large-scale temperatures and velocities in the EQTWE.

## 4. Conclusion and discussion

### 4.1. Summary of findings

We have derived a thermal wind equation valid at the equator, the EQTWE, that relates the vertical zonal wind shear to the second derivative of the temperature (or density) with respect to latitude. The EQTWE was derived to be valid at the equator, but it is also accurate at latitudes up to  $18^\circ$  away from the equator with only a 10 % error. We used the EQTWE to determine temperature profiles at altitudes below 500 mbar using wind shear measurements from the *Galileo* Doppler Wind Experiment Probe and found that the equator is cool with respect to surrounding latitudes by  $\sim 5$  K for altitudes above 5 bar. There appears to be no previously published measurement or inference of Jovian temperatures at altitudes below 500 mbar, other than those found with a general circulation model. Below 5 bar, down to  $\sim 13$  bar, the equator is warmer than the surrounding latitudes by  $\sim 2$  K. Below  $\sim 13$  bar, the *Galileo* probe did not measure values of the wind shear greater than their uncertainties. We argued that our results support a 2-layer model of global circulation with the top layer similar to the Hadley cells on Earth and the lower layer with cells with the opposite rotation. The 2-layer model was first introduced by Ingersoll et al. (2000) and later re-proposed by Showman and de Pater (2005). We also argued that, unlike Neptune, compositional anomalies such as ammonia and other volatiles<sup>11</sup> do not have an important role compared to thermal anomalies in affecting Jupiter's vertical wind shear. We showed that at altitudes above 680 mbar (the highest altitude where we have reported *Galileo* probe wind speeds), the strong vertical wind shear con-

<sup>11</sup> This observations is true for ammonia, but for water and other volatiles, future observations or new radiative transfer models might show that water or other volatiles might be important.

tinues up to 200 mbar, decreases, and then changes sign in the lower stratosphere near 80 mbar, and then changes sign again near 3 mbar. Our result for the wind shear at altitudes between 300 and 500 mbar obtained with EQTWE contradicts those obtained earlier with TWE because the TWE is ill-conditioned at low latitudes because the Coriolis parameter goes to zero near the equator. At 3 mbar we found an equatorial stratospheric jet with velocities of  $205 \pm 15$  m/s, 65 m/s faster than had been previously obtained using the TWE (Flasar et al., 2004) near the equator. To determine the zonal velocities above  $\sim 1$  bar using the zonal velocity vertical shear obtained from the EQTWE, it was necessary to integrate the shear. To do the integration, it was necessary to determine the altitude of the “cloud level” at which zonal velocity profiles have been computed using cloud displacements (c.f., Tollefson et al., 2017). We found a “cloud level” of  $950 \pm 250$  mbar, higher than the more commonly cited value of 500 mbar, but agreeing with results from Matcheva et al. (2005). The difference in the zonal velocity  $v_\phi$  between the equator (with a velocity of 77 m/s) and the latitude of the entry of the *Galileo* probe,  $7.46^\circ\text{N}$  jovigraphic, is 24 m/s, or more than 30%. However, the difference in the vertical zonal shear at cloud level between these latitudes is less than 2% and is approximately 44 m/s per  $\ln P$  or  $-1.9$  (m/s)/km. The only altitudes at which we can make a direct comparison of the shears at the equator and  $7.46^\circ$  are within a small band around 950 mbar. At altitudes between 1 bar and 680 mbar (the highest altitude where we have reported *Galileo* probe wind speeds) there is a “hook” in the shear of the probe’s measured speeds; a linear extrapolation of the shear from lower altitudes is, however, within the probe’s error bars, and hence we cannot be certain this hook is real.

Our results on the wind shear above 500 mbar illustrate the importance of the EQTWE because another analysis (Li et al., 2006) that used the TWE came to an opposite conclusion and showed that the wind shear was approximately zero between 315 and 499 mbar. One of several problems that Li et al. encountered was that they had to use the TWE at latitudes as low as  $3^\circ$  where the traditional Rossby number is of order unity.<sup>12</sup> Although it is possible by using the mirror-symmetric component of  $T$  to employ the TWE this close to the equator (see section 4.2), it requires great care because it requires taking the ratio of two small numbers (which is ill-conditioned): the meridional derivative of  $T$  and  $\sin \theta$ , where the former has a large observational uncertainty (see the error bars in the temperature data near the equator in Fig. 1). A second problem encountered by Li et al. in using the TWE is that they were required to find the value of the wind shear at the equator by extrapolating the values of the wind shear at these low latitudes to the equator, and extrapolation (in contrast to interpolation) of noisy data is ill-conditioned. In contrast to the use of the TWE at or near the equator, the EQTWE is well-conditioned and, in the case examined here, the sign and magnitude of the wind shear can be determined qualitatively just by inspection of the thermal observations.

de la Torre Juárez et al. (2002) developed a modified thermal wind equation (their Eq. (12)) for the vertical wind shear of a “geostrophic velocity” in terms of a geopotential that is valid at the equator. However, their horizontal “geostrophic velocity” (defined in the un-numbered equation before their Eq. (12)) is identically zero at the equator, and their modified TWE shows that

<sup>12</sup> This value is based on the traditional Rossby number,  $Ro = V_\phi / fL$ , where we take  $V_\phi$  to be the characteristic zonal velocity, which we set to 170 m/s using Fig. 2;  $f = f_0 \sin \theta$ ; and  $\theta = 3^\circ$ . The value of  $L$  is the characteristic length of the velocity in the meridional direction, which in the context of how  $Ro$  is used with respect to the fractional errors of the TWE is the characteristic value of  $r v_\phi / (\partial v_\phi / \partial \theta)$ . From Fig. 2 in Asay-Davis et al. (2011), the approximate half-wavelength of  $v_\phi$  at the equator is approximately  $17^\circ$  or 21,000 km. For a sinusoidal function, the characteristic value of the function divided by its derivative is the half-wavelength divided by  $\pi$ , so  $L = 6,600$  km. With these values,  $Ro = 1.4$

the vertical shear of this velocity is proportional to  $\sin \theta$ , so no information is provided by this equation at the equator. Unfortunately, due to the manner in which their modified TWE is written, it cannot be Taylor-expanded about the equator to obtain a useful relationship for the velocity shear as  $\theta \rightarrow 0$ . In fact, their Fig. 4 for the zonal geostrophic velocity shear obtained with their modified thermal wind equation using observed temperatures at 100 and 400 mbar shows that the vertical shear is nearly zero (with  $|\partial v_\phi^M / \partial (\ln P)| < 0.5$  m/s) at the equator and up to latitudes with  $\pm 20^\circ$ . This finding strongly disagrees (by a factor of 100) with the results obtained by Flasar et al. (2004) for the full velocity and our results (Fig. 6) for the mirror-symmetric component of the zonal velocity at those altitudes. The results of de la Torre Juárez et al. (2002) also disagree with the velocity shear measurements obtained by the *Galileo* probe for the full velocity at lower altitudes.

#### 4.2. Applicability of the textbook TWE near the equator

We noted in our Introduction that Allen and Sherwood (2008) observed that the TWE appears to apply very well to zonal flows on Earth at low latitudes, and we can now explain the circumstances when the TWE will work.<sup>13</sup> First note

<sup>13</sup> We noted in our Introduction that an equatorial thermal wind equation was derived by Andrews et al. (1987) (their Eq. (8.2.2)). Their derivation is effectively as follows. They start with the TWE in Eq. (15):

$$\sin \theta f_0 \frac{\partial v_\phi}{\partial r} = -\frac{g}{rT} \frac{\partial T}{\partial \theta} \Big|_p + \text{small terms}, \quad (24)$$

where by “small terms”, we mean all of the terms that were discarded in the derivation of the textbook TWE because they were judged to be small either due to slow timescales or a small local Rossby number. The “small terms” are typically not small near the equator. Andrews et al. (1987) then note that the term on the left side of Eq. (24) goes to zero at the equator, and that the right side of Eq. (24) also goes to zero at the equator if  $T$  is mirror-symmetric about the equator. Therefore, they Taylor-expand both terms in  $\theta$  about  $\theta = 0$ , retain only the leading non-zero term from each expansion (which is equivalent to applying l’Hôpital’s rule), and drop the “small terms” to obtain our EQTWE in Eq. (3). In general, dropping the “small terms” is *not valid* because if the “small terms” are not *identically* zero at the equator, then those “small terms” are much larger than the two terms that were Taylor-expanded, which are *identically* zero at the equator. In some sense, the bulk of our derivation of the EQTWE in the Appendices is spent showing that if  $T$ ,  $\rho$ , and the velocity are mirror-symmetric about the equator, then the “small terms” (i.e., the terms labeled  $\mathcal{A} - \mathcal{N}$  in Section A.2) are also *identically* zero at the equator, and when the “small terms” are Taylor-expanded, the leading non-zero terms are small compared to  $f_0 \partial v_\phi / \partial r$  and  $g/(rT)(\partial^2 T / \partial \theta^2) \Big|_p$ . It appears that Andrews et al. (1987) did not believe that their equatorial thermal wind equation was generally applicable because if  $T$  were not exactly symmetric with respect to the equator, then at the equator  $\sin \theta f_0 \partial v_\phi / \partial r = 0$ , but  $g/(rT)(\partial T / \partial \theta) \Big|_p$  would not be zero. Therefore, if one Taylor-expands  $g/(rT)(\partial T / \partial \theta) \Big|_p$  as  $[g/(rT)(\partial T / \partial \theta)] \Big|_{p, \theta=0} - \theta [g/(rT^2)(\partial T / \partial \theta)^2] \Big|_{p, \theta=0} + \theta [g/(rT)(\partial^2 T / \partial \theta^2)] \Big|_{p, \theta=0}$ , one cannot discard the first two terms of this expansion because  $(\partial T / \partial \theta) \Big|_{p, \theta=0}$  is not equal to zero. However, Andrews et al. (1987) were too cautious. Their EQTWE differs from our EQTWE in Eq. (10) because the latter only relates the mirror-symmetric components of the velocity and temperature. For most planetary flows, replacing  $T$  with  $T^M$  and  $v_\phi$  with  $v_\phi^M$  in an equatorial thermal wind would make only a minor numerical change. The EQTWE we derived in Eq. (20) does not require any restrictions on the symmetry. However, the EQTWE that we derived in Eq. (10) has the symmetry requirement that  $([T^A]/[T^M])^2 \ll 1$ . This inequality puts a constraint on how large  $(\partial T / \partial \theta)$  can be at the equator: by a Taylor series expansion at the equator,  $[T^A] \simeq \theta (\partial T / \partial \theta) \Big|_{\theta=0}$ . Thus, the previous inequality requires that  $\left\{ (\partial T / \partial \theta) \Big|_{\theta=0} \right\}^2 \ll ([T^M]/\bar{\theta})^2$ , where  $\bar{\theta}$  is the characteristic distance from the equator where the EQTWE is applied. This constraint is not strong, and for  $|\theta| \leq 10^\circ$ , the temperatures in Fig. 1 satisfy the constraint by better than 1 part in  $10^5$ .

that the EQTWE in Eq. (10) at pg. 17 states

$$f_0 \frac{\partial v_\phi^M}{\partial r} = - \frac{g'}{rT^M} \frac{\partial^2 T^M}{\partial \theta^2} \Big|_p, \quad (25)$$

where  $T^M$  and  $v_\phi^M$  are the mirror-symmetric components of the temperature and zonal velocity. Now, Taylor expand  $\partial T^M / \partial \theta$  around the equator to obtain its value at latitude  $\bar{\theta}$

$$\begin{aligned} \frac{\partial T^M}{\partial \theta} \Big|_{\theta=\bar{\theta}} &= \frac{\partial T^M}{\partial \theta} \Big|_{\theta=0} + \bar{\theta} \frac{\partial^2 T^M}{\partial \theta^2} \Big|_{\theta=0} + \frac{\bar{\theta}^2}{2} \frac{\partial^3 T^M}{\partial \theta^3} \Big|_{\theta=0} \\ &+ \frac{\bar{\theta}^3}{6} \frac{\partial^4 T^M}{\partial \theta^4} \Big|_{\theta=0} + \dots \end{aligned} \quad (26)$$

Noting that

$$\frac{\partial T^M}{\partial \theta} \Big|_{\theta=0} = \frac{\partial^3 T^M}{\partial \theta^3} \Big|_{\theta=0} \equiv 0, \quad (27)$$

we see that

$$\frac{\partial^2 T^M}{\partial \theta^2} \Big|_{\theta=0} = \frac{1}{\bar{\theta}} \frac{\partial T^M}{\partial \theta} \Big|_{\theta=\bar{\theta}} [1 + O(\bar{\theta}^2)] \quad (28)$$

$$= \frac{1}{\sin \bar{\theta}} \frac{\partial T^M}{\partial \theta} \Big|_{\theta=\bar{\theta}} [1 + O(\bar{\theta}^2)]. \quad (29)$$

Substituting Eq. (29) into Eq. (25) gives

$$(\sin \bar{\theta}) f_0 \frac{\partial v_\phi^M}{\partial r} \Big|_{\theta=0} = - \frac{g'}{rT^M} \frac{\partial T^M}{\partial \theta} \Big|_{p, \theta=\bar{\theta}} [1 + O(\bar{\theta}^2)], \quad (30)$$

which is the textbook TWE, with the exceptions that Eq. (30) is only the zonal component of the TWE and that the equation uses only the mirror-symmetric components of  $T$  and  $v_\phi$  and that the derivative of the zonal velocity is at the equator rather than  $\theta = \bar{\theta}$ .

Given the zonal shear, the meridional derivative of  $T^M$  can be determined at low latitudes, very close to the equator with Eq. (30). However given the meridional derivative of  $T^M$ , Eq. (30) is ill-conditioned to find the wind shear because it requires computing the ratio of two small quantities: the meridional derivative of  $T^M$  and  $\sin \bar{\theta}$ . In contrast, the EQTWE is well-conditioned for finding the wind shear given the temperature profile and vice versa.

In some cases, such as the measurement of the Jovian stratospheric equatorial jet (Flasar et al., 2004) and the Earth's equatorial zonal wind from radiosonde measurements (Allen and Sherwood, 2008), luck combined with caution might allow the TWE to be used near the equator to determine the zonal velocity shear. Luck requires that the flow is sufficiently mirror-symmetric about the equator so that  $\left| \frac{\partial T^M}{\partial \theta} \right| \gg \left| \frac{\partial T^A}{\partial \theta} \right|$ ; otherwise, the needed value of

$\frac{\partial T^M}{\partial \theta}$  is likely to be difficult to extract from the observed value of  $\frac{\partial T}{\partial \theta}$ . Caution requires being able to evaluate  $\frac{\partial T^M}{\partial \theta}$  accurately enough from observational or numerical data that its division by  $\sin \theta$  does not create too large a fractional error. Consider the stratospheric equatorial jet. In Section 3.2, we argued that the uncertainties in the CIRS temperature are the principal uncertainties in determining  $\partial^2 T / \partial \theta^2$ . We believe that the temperature uncertainties are also the main source of uncertainty in  $\partial T / \partial \theta$ , and therefore the uncertainties in  $\partial^2 T / \partial \theta^2$  and  $\partial T / \partial \theta$  near the equator are of the same order. However, Eq. (29) shows the value of  $\partial T / \partial \theta$  is approximately 14 times smaller than the value of  $\partial^2 T / \partial \theta^2$  because  $1/\bar{\theta} \approx 14$  at the latitudes where the TWE is applied by Flasar et al. (2004). Thus the fractional error of  $(1/\sin \theta) (\partial T / \partial \theta)$  and of the zonal shear deduced from the TWE are of order unity, which is why it is not

surprising that the velocity of the stratospheric equatorial jet found by Flasar et al. (2004) differs from our value by  $\sim 50\%$ .<sup>14</sup>

The stratospheric jet near  $5^\circ$  latitude has a Rossby number greater than unity, so the textbook TWE does not apply to it and therefore cannot be used to compute the zonal shear from the meridional temperature gradient. Eq. (30) does apply, but requires using the meridional gradient of the mirror-symmetric component of the temperature,  $\frac{\partial T^M}{\partial \theta}$ , rather than the gradient of the full temperature,  $\frac{\partial T}{\partial \theta}$ . If the meridional gradient of the non-mirror symmetric component of the temperature had happened to be significant at the altitude of the stratospheric jet, then even if  $\frac{1}{\sin \theta} \frac{\partial T}{\partial \theta}$  were accurately determined, the TWE would give an incorrect velocity shear.

#### 4.3. Future work

Our application of the EQTWE in the Jovian tropics, resulting in Fig. 8, supports that scenario of a 2-layer cellular global circulation schematically shown in Fig. 10 with the boundary between the two layers near 5 bar (which is identical to the altitude in Fig. 2 where the wind shear changes sign near  $\sim 5$  bar). This altitude is also the location of the proposed Jovian water cloud (Atreya and Romani, 1985; de Pater et al., 2005), which begs the question of whether the locations of the boundary and of the water cloud are a coincidence or whether they are dynamically linked, i.e., it is possible that the upward and downward motions at the layers' boundary creates the water cloud or vice versa. Computational methods and availability of resources have advanced sufficiently that a 2-layer model can be simulated numerically. A numerical model of the global circulation can show whether the terminations of the upwelling and downwelling motions at the boundary between the two layers promotes the formation of water clouds. A simulation could also test whether an *ab initio* water cloud placed at 5 bar would cause a Hadley cell circulation in the upper troposphere to form a lower boundary at the location of the water cloud. A simulation could also be used to determine whether a circulation similar to a Hadley cell circulation, but with the opposite sense of rotation, in the troposphere below 5 bar would form an upper boundary at the location of the water cloud. This type of numerical simulation might also explain why the equatorial jet near 3 mbar is so intense and whether it is steady in time or part of a 4–5 year quasi-biennial oscillation. It will be interesting to see if the global circulation model agrees with our surprising finding here that the vertical zonal wind shear at the equator and at  $7.46^\circ\text{N}$  are nearly identical despite the fact that the zonal velocities at these latitudes differ by more than 30%. It is important to know how big the differences are between the winds shear at various pairs of latitudes and how dependent those differences are as a function of altitude. How these differences vary with respect to latitude and altitude can distinguish between different models of the zone/belt system. Using a fully dynamic set of equations, that includes the transport of energy and momentum due to waves (c.f., Rossby waves Liu and Schneider, 2010 and internal gravity waves Holton, 1983) and due to the anomalous heating/cooling of the clouds (from absorbed/emitted radiation and due to the phase transitions within them), rather than the kinematic approximations used in the TWE and EQTWE, could provide an explanation of the Galileo probe

<sup>14</sup> As we showed in Section 3.2, one large source in the uncertainty in our measurement of the stratospheric jet wind speed from wind shears obtained by the EQTWE is the uncertainty in reference altitude for the “cloud level” velocities, which we determined was  $950 \pm 250$  mbar. Flasar et al. (2004), using a reference altitude of 500 mbar determined the jet velocity is 140 m/s. If we had used the same reference altitude with our EQTWE analysis, we would have obtained a maximum jet velocity of 235 m/s.

velocity measurements that differs from the Hadley cell explanation in Fig. 10.

Future observations with ALMA with different spectral lines, such as HCN and CO that probe different depths in the stratosphere (e.g., Lellouch et al., 2006), could be used to determine zonal wind speeds as a function of latitude at multiple altitudes. Using mid-infrared data as in Fig. 1, one could then test the EQTWE for self-consistency. These measurements and values could be used to guide the construction of a numerical general circulation model that extends from the troposphere into the stratosphere.

The simulation could also be used to analyze the recent *Juno* Microwave Radiometer data that suggest a minimum in the ammonia abundance near the 6 bar level at latitudes  $|\theta| \leq 40^\circ$ , except for the equator (Bolton et al., 2017; Li et al., 2017). This observational finding seems counter-intuitive to the 2-layer cellular circulation scenario, where one might expect a condensable gas to decrease with altitude (due c.f., to cloud formation), but never increase. Showman and de Pater (2005) postulated latitudinal (horizontal) transport from belts to zones at all altitudes in the upper cell to deplete the ammonia abundance also in the zones. If, in contrast, gas and clouds are transported in the upper cell from zones to belts, cloud particles should evaporate during descent in the belt and thereby enhance the ammonia concentration in the belts in the upper layer as observed by *Juno*. Detailed numerical simulations of future VLA and *Juno* observations could either confirm the 2-layer cellular circulation model or reject it and perhaps replace it with a new circulation model that is consistent with all of the observations and with the results of the EQTWE analysis presented in this paper.

## Acknowledgments

We thank Peter Gierasch for interesting discussions. Partial support was supplied by NSF grants AST-1009907, AST-1615004, and AST-1510703; by NASA PATM grants NNX10AB93G and NNX13AG56G; by NASA PAST grant NNX14AJ43G; and by the NASA Earth and Space Science Fellowship program Grant NNX16AP12H to UC Berkeley. Partial support for computational work was provided by NSF XSEDE (NSF OCI-1053575) and NASA-HEC. Data for Figs. 3 and 4 are from Gemini program GN-2017A-Q-60 and HST programs GO-14334 and GO-14661. Support for HST programs GO-14334 and GO-14661 was provided by NASA through a grant from the Space Telescope Science Institute, which is operated by the Association of Universities for Research in Astronomy, Inc., under NASA contract NAS 5-26555. Support for Gemini data analysis was provided by the NASA Solar System Observations Program grant number NNX15AJ41G. The authors acknowledge additional observing team members Amy Simon, Andrew Stephens, Megan Barnett, Glenn Orton, Gordon Bjoraker, Alberto Adriani, and Sushil Atreya for use of the HST and Gemini data.

## Appendix A

To derive our EQTWE is straight-forward but tedious. In Section A.1, we take the curl of the governing Euler's equation (in the rotating frame of the planet) to obtain the vorticity equation, and using the mathematical identities in Appendix B, we simplify it. This simplification is the starting point of the derivation of both the TWE and the EQTWE. In Section A.2 we show that all of the terms in the vorticity equation for an equatorially-symmetric flow field go to zero at the equator *not just the Coriolis term*. Thus, to obtain useful information at the equator, we take the limit of every term as  $\theta \rightarrow 0$  by Taylor expanding all of the terms there – a method that is a generalization of l'Hôpital's rule. In Section A.3 we show that in this limit that all of the nonlinear advection terms are small compared to the Coriolis and pressure terms. The balance

between the limits of the Coriolis and pressure terms yields the EQTWE. The nonlinear advection terms are small when the flow is dominated by large velocities of order  $V_\theta$  and  $V_\phi$  (or greater) at the large length scales of  $L_\phi$  and  $L_\theta$  (or greater). This requirement is what leads to our obtaining fractional errors that depend on  $V_\theta$ ,  $V_\phi$ ,  $L_\phi$ , and  $L_\theta$ . In Section A.4 we relax the requirement that the flow field be exactly mirror-symmetric with respect to the equator. Relaxing this requirement shows that new fractional errors of order  $([T^A]/[T^M])^2$ ,  $([\rho^A]/[\rho^M])^2$ , and  $([\mathbf{v}^A]/[\mathbf{v}^M])^2$  are introduced.

### A1. Governing equation for the azimuthal component of the vorticity

Starting with Euler's equation we now derive the EQTWE. Euler's equation in spherical coordinates rotating around the  $z$ -axis with angular velocity  $\Omega_0$  is:

$$\begin{aligned} \frac{\partial \mathbf{v}}{\partial t} &= -(\mathbf{v} \cdot \nabla) \mathbf{v} - \frac{\nabla P}{\rho} + f_0 \mathbf{v} \times \hat{\mathbf{z}} - g \hat{\mathbf{r}} + \nabla(\Omega_0^2 r^2 \cos^2 \theta)/2, \quad (31) \\ &= (\mathbf{v} \times \boldsymbol{\omega}) - \frac{\nabla P}{\rho} - \nabla|\mathbf{v}|^2/2 + f_0 \mathbf{v} \times \hat{\mathbf{z}} - g \hat{\mathbf{r}} + \nabla(\Omega_0^2 r^2 \cos^2 \theta)/2, \quad (32) \end{aligned}$$

where gravity is in the  $\hat{\mathbf{r}}$  direction.

The curl of Eq. (32) gives the vorticity  $\boldsymbol{\omega}$  equation.

$$\begin{aligned} \frac{\partial \boldsymbol{\omega}}{\partial t} + (\mathbf{v} \cdot \nabla) \boldsymbol{\omega} - (\boldsymbol{\omega} \cdot \nabla) \mathbf{v} + (\nabla \cdot \mathbf{v}) \boldsymbol{\omega} &= \frac{\nabla \rho \times \nabla P}{\rho^2} \\ &+ f_0 [(\hat{\mathbf{z}} \cdot \nabla) \mathbf{v} - (\nabla \cdot \mathbf{v}) \hat{\mathbf{z}}], \quad (33) \end{aligned}$$

where the gravity term, which is a potential force, vanishes exactly because it is a perfect gradient (even when  $g$  is not constant), and where we used the following vector identity twice:

$$\nabla \times (\mathbf{A} \times \mathbf{B}) \equiv (\nabla \cdot \mathbf{B}) \mathbf{A} - (\nabla \cdot \mathbf{A}) \mathbf{B} + (\mathbf{B} \cdot \nabla) \mathbf{A} - (\mathbf{A} \cdot \nabla) \mathbf{B}. \quad (34)$$

Taking the dot product of Eq. (33) with  $\hat{\boldsymbol{\phi}}$  and using the identity (see Batchelor, 2000, Appendix 2)

$$\hat{\boldsymbol{\phi}} \cdot [(\mathbf{A} \cdot \nabla) \mathbf{B}] \equiv (\mathbf{A} \cdot \nabla) B_\phi + A_\phi (B_r - B_\theta \tan \theta)/r, \quad (35)$$

we obtain:

$$\begin{aligned} \frac{\partial \omega_\phi}{\partial t} + (\mathbf{v} \cdot \nabla) \omega_\phi + v_\phi (\omega_r - \omega_\theta \tan \theta)/r \\ - (\boldsymbol{\omega} \cdot \nabla) v_\phi - \omega_\phi (v_r - v_\theta \tan \theta)/r \\ + (\nabla \cdot \mathbf{v}) \omega_\phi \\ = \hat{\boldsymbol{\phi}} \cdot \frac{\nabla \rho \times \nabla P}{\rho^2} + f_0 \frac{\partial v_\phi}{\partial z}, \quad (36) \end{aligned}$$

If Eq. (2) is valid, then we could replace  $\frac{\nabla \rho \times \nabla P}{\rho^2}$  with  $-\frac{\nabla T \times \nabla P}{T \rho}$ .

As a crude approximation,  $\nabla P$  in Eq. (36) could be replaced with the hydrostatic equation, i.e.,  $\nabla P \simeq -g \rho \hat{\mathbf{r}}$ , so that  $\nabla \rho \times \nabla P$  could be replaced with  $g \rho \hat{\mathbf{r}} \times \nabla \rho$ , and so that the azimuthal component of  $\nabla \rho \times \nabla P$  could be approximated as  $-\frac{g \rho}{r} \frac{\partial \rho}{\partial \theta}$ . Eq. (124) in Appendix B, which we repeat here for convenience, gives the exact form of this approximation including its fractional errors:

$$\begin{aligned} \hat{\boldsymbol{\phi}} \cdot (\nabla \rho \times \nabla P) &= \frac{g' \rho}{r} \frac{\partial \rho}{\partial \theta} \Big|_p \\ &\times \left[ 1 + O \left( \frac{DV_\phi^2}{g' L_\phi^2}, \frac{DV_\theta^2}{g' L_\theta^2}, \frac{DV_\phi V_\theta}{g' L_\phi L_\theta}, \frac{f_0 V_\phi}{g'}, \frac{V_\phi^2}{g' r_0} \right) \right], \quad (37) \end{aligned}$$

with the large square brackets meaning that the equation has fractional errors of  $O \left( \frac{DV_\phi^2}{g' L_\phi^2}, \frac{DV_\theta^2}{g' L_\theta^2}, \frac{DV_\phi V_\theta}{g' L_\phi L_\theta}, \frac{f_0 V_\phi}{g'}, \frac{V_\phi^2}{g' r_0} \right)$ . Note that the partial derivative of the density in Eq. (37) holds  $P$ , rather than  $z$ , constant. Here, we define the effective gravity as in Section 4.1,  $g' \equiv g - (f_0^2 r_0 \cos \theta)/4$  (i.e.,  $g'$  is  $g$  minus the centrifugal acceleration in the radial direction).

For the giant gas planets, these fractional error terms are small because the vertical scale height  $D$  is much smaller than the extent of the horizontal flow. Therefore, we shall drop these fractional errors from the remainder of our derivation below, *but note that we have included these fractional errors in the enumerated list of fractional errors listed in Section 4.1, expression (4), and Section A.3.*

Using Eqs. (36) and (37) without the fractional error terms, we obtain

$$\begin{aligned} & \frac{\partial \omega_\phi}{\partial t} + (\mathbf{v} \cdot \nabla) \omega_\phi + v_\phi (\omega_r - \omega_\theta \tan \theta) / r \\ & - (\boldsymbol{\omega} \cdot \nabla) v_\phi - \omega_\phi (v_r - v_\theta \tan \theta) / r \\ & + (\nabla \cdot \mathbf{v}) \omega_\phi \\ & = - \frac{\mathbf{g}'}{r\rho} \frac{\partial \rho}{\partial \theta} \Big|_p + f_0 \frac{\partial v_\phi}{\partial z}. \end{aligned} \quad (38)$$

If Eq. (2) is valid, we could replace  $-\frac{\mathbf{g}'}{r\rho} \frac{\partial \rho}{\partial \theta} \Big|_p$  with  $\frac{\mathbf{g}'}{rT} \frac{\partial T}{\partial \theta} \Big|_p$  in the above equation and in all of the following equations wherever  $\frac{\mathbf{g}'}{r\rho} \frac{\partial \rho}{\partial \theta} \Big|_p$  appears.

Noting that

$$\frac{\partial}{\partial z} \equiv \sin \theta \frac{\partial}{\partial r} + \frac{\cos \theta}{r} \frac{\partial}{\partial \theta}, \quad (39)$$

and assuming that changes in the flow are slow in time so that  $|\partial \omega_\phi / \partial t| \ll \left| \frac{\mathbf{g}'}{r\rho} \frac{\partial \rho}{\partial \theta} \Big|_p \right|$ , Eq. (38) becomes

$$\begin{aligned} & -f_0 \frac{\cos \theta}{r} \frac{\partial v_\phi}{\partial \theta} + (\mathbf{v} \cdot \nabla) \omega_\phi + v_\phi (\omega_r - \omega_\theta \tan \theta) / r \\ & - (\boldsymbol{\omega} \cdot \nabla) v_\phi - \omega_\phi (v_r - v_\theta \tan \theta) / r + (\nabla \cdot \mathbf{v}) \omega_\phi \\ & = - \frac{\mathbf{g}'}{r\rho} \frac{\partial \rho}{\partial \theta} \Big|_p + f_0 \sin \theta \frac{\partial v_\phi}{\partial r}. \end{aligned} \quad (40)$$

Two of the largest contributions to the term  $(\boldsymbol{\omega} \cdot \nabla) v_\phi$ , which appears on the left side of Eq. (40) cancel, but to see this we need to exploit some identities.

$$(\boldsymbol{\omega} \cdot \nabla) v_\phi \equiv \frac{\omega_\phi}{r \cos \theta} \frac{\partial v_\phi}{\partial \phi} + \omega_r \frac{\partial v_\phi}{\partial r} + \frac{\omega_\theta}{r} \frac{\partial v_\phi}{\partial \theta} \quad (41)$$

$$\omega_r \equiv \frac{1}{r \cos \theta} \left[ -\cos \theta \frac{\partial v_\phi}{\partial \theta} + \sin \theta v_\phi + \frac{\partial v_\theta}{\partial \phi} \right] \quad (42)$$

$$\omega_\theta \equiv -\frac{1}{r} \left[ \frac{1}{\cos \theta} \frac{\partial v_r}{\partial \phi} - v_\phi - r \frac{\partial v_\phi}{\partial r} \right] \quad (43)$$

$$\omega_\phi \equiv \frac{1}{r} \left[ -r \frac{\partial v_\theta}{\partial r} - v_\theta + \frac{\partial v_r}{\partial \theta} \right] \quad (44)$$

Substituting these identities and canceling:<sup>15</sup>

$$(\boldsymbol{\omega} \cdot \nabla) v_\phi = \frac{1}{r^2 \cos \theta} \left[ -r \frac{\partial v_\theta}{\partial r} - v_\theta + \frac{\partial v_r}{\partial \theta} \right] \frac{\partial v_\phi}{\partial \phi} \quad (45)$$

$$+ \frac{1}{r \cos \theta} \left[ -\cos \theta \frac{\partial v_\phi}{\partial \theta} + \sin \theta v_\phi + \frac{\partial v_\theta}{\partial \phi} \right] \frac{\partial v_\phi}{\partial r} \quad (46)$$

$$- \frac{1}{r^2} \left[ \frac{1}{\cos \theta} \frac{\partial v_r}{\partial \phi} - v_\phi - r \frac{\partial v_\phi}{\partial r} \right] \frac{\partial v_\phi}{\partial \theta} \quad (47)$$

Eq. (40) becomes

$$\begin{aligned} & -f_0 \frac{\cos \theta}{r} \frac{\partial v_\phi}{\partial \theta} + (\mathbf{v} \cdot \nabla) \omega_\phi + v_\phi (\omega_r - \omega_\theta \tan \theta) / r \\ & - \frac{\omega_\phi}{r \cos \theta} \frac{\partial v_\phi}{\partial \phi} - \omega_\phi (v_r - v_\theta \tan \theta) / r \\ & - \frac{v_\phi \tan \theta}{r} \frac{\partial v_\phi}{\partial r} - \frac{1}{r \cos \theta} \frac{\partial v_\phi}{\partial r} \frac{\partial v_\theta}{\partial \phi} \\ & - \frac{1}{r^2} \frac{\partial v_\phi}{\partial \theta} \left[ v_\phi - \frac{1}{\cos \theta} \frac{\partial v_r}{\partial \phi} \right] \\ & + (\nabla \cdot \mathbf{v}) \omega_\phi \\ & = - \frac{\mathbf{g}'}{r\rho} \frac{\partial \rho}{\partial \theta} \Big|_p + f_0 \sin \theta \frac{\partial v_\phi}{\partial r}. \end{aligned} \quad (48)$$

The textbook TWE can be derived from the equation above by replacing  $-\frac{\mathbf{g}'}{r\rho} \frac{\partial \rho}{\partial \theta} \Big|_p$  with  $\frac{\mathbf{g}'}{rT} \frac{\partial T}{\partial \theta} \Big|_p$ , and showing that there is a dominant balance between the two terms on the right-hand side of Eq. (48). The derivation of the EQTWE Eq. (3) arises similarly but uses a Taylor series expansion around the equator.

## A2. Taylor series expansion

Starting with Eq. (48) we derive the EQTWE in Eq. (3) in two stages. In the first stage, presented in this section, we make the idealized assumption that the velocity and thermodynamic variables are mirror-symmetric about the equator, i.e., we assume that  $T$ ,  $\rho$ ,  $v_\phi$ , and  $v_r$  are symmetric about the equator and that  $v_\theta$  is anti-symmetric. In practice, this is too unrealistic an assumption, so in the second stage of our derivation of the EQTWE, presented in Section A.4, we drop this ideal assumption. We have chosen to present our derivation in these stages because we believe it is much easier to explain and understand this way. However, before continuing with the derivation, we need to emphasize that the final derivation does not depend on mirror-symmetry of the velocity.

Our temporary assumption is that the flow is mirror-symmetric; specifically, each velocity component  $v_r$ ,  $v_\theta$  and  $v_\phi$ , like the thermodynamic variables  $\rho$ ,  $P$ , and  $T$ , is decomposed, as in Section 4.1, into a component that is mirror-symmetric (denoted with an ‘‘M’’ superscript) about the equator and a component that is anti-mirror-symmetric (denoted with a ‘‘A’’ superscript). For  $v_\phi$  and  $v_r$ :

$$v_\phi^M(r, \theta, \phi) \equiv [v_\phi(r, \theta, \phi) + v_\phi(r, -\theta, \phi)] / 2 \quad (49)$$

$$v_\phi^A(r, \theta, \phi) \equiv [v_\phi(r, \theta, \phi) - v_\phi(r, -\theta, \phi)] / 2 \quad (50)$$

$$v_r^M(r, \theta, \phi) \equiv [v_r(r, \theta, \phi) + v_r(r, -\theta, \phi)] / 2 \quad (51)$$

$$v_r^A(r, \theta, \phi) \equiv [v_r(r, \theta, \phi) - v_r(r, -\theta, \phi)] / 2 \quad (52)$$

However, for  $v_\theta$  the symmetries are defined with the opposite signs:

$$v_\theta^M(r, \theta, \phi) \equiv [v_\theta(r, \theta, \phi) - v_\theta(r, -\theta, \phi)] / 2 \quad (53)$$

$$v_\theta^A(r, \theta, \phi) \equiv [v_\theta(r, \theta, \phi) + v_\theta(r, -\theta, \phi)] / 2, \quad (54)$$

that is,  $v_\theta^M$  is anti-symmetric with respect to the equator, while  $v_\theta^A$  is symmetric with respect to the equator. The mirror-symmetric component of the velocity vector  $\mathbf{v}^M$  is made up of the three mirror-symmetric components defined in Eqs. (49), (51), and (53); and the anti-mirror-symmetric component of the velocity vector  $\mathbf{v}^A$  is made up of the three anti-mirror-symmetric components. It is possible to have solutions to the equations of motion in which the flow is mirror-symmetric with no anti-mirror-symmetric components defined in Eqs. (50), (52), and (54). (i.e.,

<sup>15</sup> We postpone to a footnote in Section A.3 our discussion of how large these canceled terms are and why, without their cancellation, they would invalidate the EQTWE.

with  $\rho^A \equiv T^A \equiv P^A \equiv \mathbf{v}^A \equiv 0$ ). We assume in this section that the flow is mirror-symmetric.

A mirror-symmetric flow has an  $\omega_r$  and  $\omega_\phi$  that are anti-symmetric with respect to the equator, while  $\omega_\theta$  and  $(\nabla \cdot \mathbf{v})$  are symmetric with respect to the equator. With a mirror-symmetric flow, all of the terms in Eq. (48) are anti-symmetric with respect to the equator. This means that every term in the equation vanishes at the equator, *not just the Coriolis terms*. This fact does *not* mean that the equation provides no information at the equator. On the contrary, by Taylor-expanding each term about  $\theta = 0$ , each term becomes a power series in the odd powers of  $\theta$ . If we replace each of the terms in Eq. (48) with its power series expansion in  $\theta$ , then drop all terms that are of order  $\theta^3$  and higher, and then divide both sides of the equation by  $\theta$ , we obtain an equation that is *exact* at the equator and a good approximation where  $\theta$  is small. This is an example of an asymptotic expansion and is the method that was used in evaluating quotients with l'Hôpital's rule. Finally, we shall make an estimate in terms of the usual dimensionless constants of each of the terms in Eq. (48) and show that all of the terms on the left side of Eq. (48) are small compared to those on the right side to yield the EQTWE in Eq. (3).

Before continuing with the derivation, we wish to make several important comments. So far we have been rigorous. We started with Euler's equation and differentiated it once to obtain the vorticity equation. Our two approximations so far (assumption of a near steady flow, and the use of Eq. (37)) end up allowing us to discard terms. However, these approximations were all made *after* the last differentiation. This is important because even though a term is small compared to other terms, the derivative of that term may be of order or larger than the derivative of the other terms. Furthermore, none of our approximations become invalid at the equator. In addition, we have not ignored *any* components of the Coriolis force. Finally, there are no  $(\sin\theta)$  terms in any denominators, which would become infinite at the equator.

There is an important difference in carrying out Taylor series expansions of functions that are symmetric or anti-symmetric about the equator. For a mirror-symmetric velocity field,  $v_\phi$  is symmetric about  $\theta = 0$  such that  $v_\phi(r, \theta, \phi) = v_\phi(r, -\theta, \phi)$ , and we Taylor-expand  $v_\phi$  in even powers of  $\theta$ , with  $v_\phi = [v_\phi] + [\partial^2 v_\phi / \partial \theta^2] \theta^2 / 2 + \dots$ , where the quantities in the square brackets are evaluated at  $\theta = 0$ . For a mirror-symmetric velocity velocity field,  $v_\theta$  is anti-symmetric function about  $\theta = 0$  such that  $v_\theta(r, \theta, \phi) = -v_\theta(r, -\theta, \phi)$ , and we Taylor-expand  $v_\theta$  in odd powers of  $\theta$ , with  $v_\theta = [\partial v_\theta / \partial \theta] \theta + [\partial^3 v_\theta / \partial \theta^3] \theta^3 / 6 + \dots$ , where the quantities in the square brackets are evaluated at  $\theta = 0$ . This means that we Taylor expand  $\partial v_\phi / \partial \theta$  at the equator in an odd series as  $\partial v_\phi / \partial \theta = [\partial^2 v_\phi / \partial \theta^2] \theta + O(\theta^3)$ . Similarly, we expand  $\partial v_\theta / \partial \theta$  at the equator in an even series as  $\partial v_\theta / \partial \theta = [\partial v_\theta / \partial \theta] + O(\theta^2)$ .

The Taylor series expansions in Eq. (48) make use of expansions of the vorticity components and the divergence. Expressed as a Taylor series in powers of  $\theta$ , note that  $\omega_r$  and  $\omega_\phi$  is an odd function of  $\theta$ , and  $\omega_\theta$  is an even function of  $\theta$ , with:

$$\omega_r = \frac{1}{r} \left[ -\frac{\partial^2 v_\phi}{\partial \theta^2} + v_\phi + \frac{\partial^2 v_\theta}{\partial \phi \partial \theta} \right] \theta + O(\theta^3) \tag{55}$$

$$\omega_\theta = -\frac{1}{r} \left[ \frac{\partial v_r}{\partial \phi} - v_\phi - r \frac{\partial v_\phi}{\partial r} \right] + O(\theta^2) \tag{56}$$

$$\omega_\phi = \frac{1}{r} \left[ -r \frac{\partial^2 v_\theta}{\partial r \partial \theta} - \frac{\partial v_\theta}{\partial \theta} + \frac{\partial^2 v_r}{\partial \theta^2} \right] \theta + O(\theta^3) \tag{57}$$

The divergence of the velocity is an even power series:

$$\nabla \cdot \mathbf{v} = \frac{1}{r} \left[ r \frac{\partial v_r}{\partial r} + 2v_r + \frac{\partial v_\theta}{\partial \theta} + \frac{\partial v_\phi}{\partial \phi} \right] + O(\theta^2) \tag{58}$$

Below are the Taylor series expansions of each of the terms that appear in Eq. (48), with a label assigned to each term so that we can refer to it when estimating its order of magnitude. The notation that  $O(\theta^3)$  means “terms of order  $\theta^3$  and higher”, and note that all of the quantities and derivatives that have horizontal braces beneath them or in large square brackets should be evaluated at the equator.

$$f_0 \frac{\cos \theta}{r} \frac{\partial v_\phi}{\partial \theta} = \underbrace{\left[ \frac{f_0}{r} \frac{\partial^2 v_\phi}{\partial \theta^2} \right]}_A \theta + O(\theta^3) \tag{59}$$

$$(\mathbf{v} \cdot \nabla) \omega_\phi = \underbrace{\left\{ v_r \left[ -\frac{\partial^3 v_\theta}{\partial r^2 \partial \theta} - \frac{1}{r} \frac{\partial^2 v_\theta}{\partial r \partial \theta} + \frac{1}{r^2} \frac{\partial v_\theta}{\partial \theta} + \frac{1}{r} \frac{\partial^3 v_r}{\partial r \partial \theta^2} - \frac{1}{r^2} \frac{\partial^2 v_r}{\partial \theta^2} \right]}_B \right. \tag{60}$$

$$\left. + \frac{1}{r^2} \frac{\partial v_\theta}{\partial \theta} \left[ -r \frac{\partial^2 v_\theta}{\partial r \partial \theta} - \frac{\partial v_\theta}{\partial \theta} + \frac{\partial^2 v_r}{\partial \theta^2} \right] \right\} \tag{61}$$

$$+ \underbrace{\left\{ \frac{v_\phi}{r^2} \left[ -r \frac{\partial^3 v_\theta}{\partial r \partial \theta \partial \phi} - \frac{\partial^2 v_\theta}{\partial \theta \partial \phi} + \frac{\partial^3 v_r}{\partial \theta^2 \partial \phi} \right] \right\}}_C \theta + O(\theta^3) \tag{62}$$

$$(\mathbf{v}_\phi \omega_r) / r = \underbrace{\frac{v_\phi}{r^2} \left[ -\frac{\partial^2 v_\phi}{\partial \theta^2} + v_\phi + \frac{\partial^2 v_\theta}{\partial \phi \partial \theta} \right]}_E \theta + O(\theta^3) \tag{63}$$

$$(\mathbf{v}_\phi \omega_\theta \tan \theta) / r = -\underbrace{\frac{v_\phi}{r^2} \left[ \frac{\partial v_r}{\partial \phi} - v_\phi - r \frac{\partial v_\phi}{\partial r} \right]}_F \theta + O(\theta^3) \tag{64}$$

$$\frac{\omega_\phi}{r \cos \theta} \frac{\partial v_\phi}{\partial \phi} = \underbrace{\frac{1}{r^2} \frac{\partial v_\phi}{\partial \phi} \left[ -r \frac{\partial^2 v_\theta}{\partial r \partial \theta} - \frac{\partial v_\theta}{\partial \theta} + \frac{\partial^2 v_r}{\partial \theta^2} \right]}_G \theta + O(\theta^3) \tag{65}$$

$$(\omega_\phi v_r) / r = \underbrace{\frac{v_r}{r^2} \left[ -r \frac{\partial^2 v_\theta}{\partial r \partial \theta} - \frac{\partial v_\theta}{\partial \theta} + \frac{\partial^2 v_r}{\partial \theta^2} \right]}_H \theta + O(\theta^3) \tag{66}$$

$$(\omega_\phi v_\theta \tan \theta) / r = \underbrace{0}_I + O(\theta^3) \tag{67}$$

Note that the Taylor series for the above expression starts with the  $\theta^3$  term.

$$\frac{v_\phi \tan \theta}{r} \frac{\partial v_\phi}{\partial r} = \underbrace{\left[ \frac{v_\phi}{r} \frac{\partial v_\phi}{\partial r} \right]}_J \theta + O(\theta^3) \tag{68}$$

$$\frac{1}{r \cos \theta} \frac{\partial v_\phi}{\partial r} \frac{\partial v_\theta}{\partial \phi} = \underbrace{\left[ \frac{1}{r} \frac{\partial v_\phi}{\partial r} \frac{\partial^2 v_\theta}{\partial \phi \partial \theta} \right]}_K \theta + O(\theta^3) \tag{69}$$

$$\frac{1}{r^2} \frac{\partial v_\phi}{\partial \theta} v_\phi = \underbrace{\left[ \frac{1}{r^2} \frac{\partial^2 v_\phi}{\partial \theta^2} v_\phi \right]}_L \theta + O(\theta^3) \tag{70}$$

$$\frac{1}{r^2} \frac{\partial v_\phi}{\partial \theta} \frac{1}{\cos \theta} \frac{\partial v_r}{\partial \phi} = \underbrace{\left[ \frac{1}{r^2} \frac{\partial^2 v_\phi}{\partial \theta^2} \frac{\partial v_r}{\partial \phi} \right]}_M \theta + O(\theta^3) \tag{71}$$

$$\begin{aligned} \omega_\phi (\nabla \cdot \mathbf{v}) &= \frac{1}{r^2} \underbrace{\left[ r \frac{\partial v_r}{\partial r} + 2v_r + \frac{\partial v_\theta}{\partial \theta} + \frac{\partial v_\phi}{\partial \phi} \right]}_{\mathcal{N}} \left[ -r \frac{\partial^2 v_\theta}{\partial r \partial \theta} - \frac{\partial v_\theta}{\partial \theta} + \frac{\partial^2 v_r}{\partial \theta^2} \right] \\ &\quad + O(\theta^3) \end{aligned} \quad (72)$$

$$\frac{g'}{rT} \frac{\partial T}{\partial \theta} \Big|_p = \left[ \frac{g'}{rT} \frac{\partial^2 T}{\partial \theta^2} \Big|_p \right] \theta + O(\theta^3) \quad (73)$$

$$f_0 \sin \theta \frac{\partial v_\phi}{\partial r} = \underbrace{\left[ f_0 \frac{\partial v_\phi}{\partial r} \right]}_P \theta + O(\theta^3) \quad (74)$$

### A3. Estimates of the magnitudes of the terms in the Taylor expansion

Now we need to estimate the magnitude of all of the terms in expressions (59)–(74). Recalling that  $L_\phi$ ,  $L_\theta$ , and  $D$  are the characteristic lengths in the east-west, north-south, and vertical (i.e., radial) directions over which the time-averaged velocity changes at the equator; and that  $V_\phi$  and  $V_r$  are the characteristic velocities of the east-west and vertical components of the time-averaged velocity at the equator; we define  $V_\theta$  such that the characteristic value of the time-averaged  $\partial v_\theta / \partial \theta$  at the equator is  $r_0 V_\theta / L_\theta$ , where  $r_0$  is the characteristic value of  $r$  in the atmosphere where we are carrying out this analysis. To estimate the magnitude of each term, we replace  $\partial / \partial \theta$  with  $r_0 / L_\theta$ ;  $\partial / \partial \phi$  with  $r_0 / L_\phi$ ; and  $\partial / \partial r$  with  $1/D$ .

Non-dimensionalizing each of the labeled expressions in (59)–(74) by expressing it in units of  $D / (f_0 V_\phi)$ , their magnitudes are:<sup>16</sup>

$$\mathcal{A} = O\left(\frac{Dr_0}{L_\theta^2}\right) \quad (75)$$

$$\mathcal{B} = \overline{Ro} \ O\left(\frac{r_0}{D} \frac{V_r V_\theta}{V_\phi^2}, \frac{V_r V_\theta}{V_\phi^2}, \frac{D}{r_0} \frac{V_r V_\theta}{V_\phi^2}, \frac{r_0}{L_\theta} \frac{V_r^2}{V_\phi^2}, \frac{D}{L_\theta} \frac{V_r^2}{V_\phi^2}\right) \quad (76)$$

$$\mathcal{C} = \overline{Ro} \ O\left(\frac{r_0}{L_\theta} \frac{V_\theta^2}{V_\phi^2}, \frac{D}{L_\theta} \frac{V_\theta^2}{V_\phi^2}, \frac{Dr_0}{L_\theta^2} \frac{V_r V_\theta}{V_\phi^2}\right) \quad (77)$$

$$\mathcal{D} = \overline{Ro} \ O\left(\frac{r_0}{L_\theta} \frac{V_\theta}{V_\phi}, \frac{D}{L_\theta} \frac{V_\theta}{V_\phi}, \frac{Dr_0}{L_\theta L_\phi} \frac{V_r}{V_\phi}\right) \quad (78)$$

$$\mathcal{E} = \overline{Ro} \ O\left(\frac{D}{L_\theta}, \frac{DL_\theta}{r_0^2}, \frac{D}{L_\theta} \frac{V_\theta}{V_\phi}\right) \quad (79)$$

$$\mathcal{F} = \overline{Ro} \ O\left(\frac{DL_\theta}{r_0 L_\phi} \frac{V_r}{V_\phi}, \frac{DL_\theta}{r_0^2}, \frac{L_\theta}{r_0}\right) \quad (80)$$

$$\mathcal{G} = \overline{Ro} \ O\left(\frac{r_0}{L_\phi} \frac{V_\theta}{V_\phi}, \frac{D}{L_\phi} \frac{V_\theta}{V_\phi}, \frac{Dr_0}{L_\theta L_\phi} \frac{V_r}{V_\phi}\right) \quad (81)$$

$$\mathcal{H} = \overline{Ro} \ O\left(\frac{V_r V_\theta}{V_\phi^2}, \frac{D}{r_0} \frac{V_r V_\theta}{V_\phi^2}, \frac{D}{L_\theta} \frac{V_r^2}{V_\phi^2}\right) \quad (82)$$

$$\mathcal{I} = 0 \quad (83)$$

<sup>16</sup> In making our estimates of magnitudes, we make the assumption that  $T$ ,  $\rho$ , and  $\mathbf{v}$  have only one magnitude and one length scale associated with each of the three spatial dimensions. This is, of course, not true, and although an intermittent turbulent flow filled with vortices and waves may be dominated by a large-scale flow with temperatures, densities and velocities with characteristic lengths of  $L_\theta$ ,  $L_\phi$ , and  $D$ , the velocity field is likely to be filled with small, intense vortices whose values of  $\nabla \times \mathbf{v}$  at some specific locations with small volume that are much greater than  $V_\phi / L_\theta$ , etc. These small vortices do not invalidate our estimate of the magnitudes as long as they do not significantly affect the longitudinally-averaged, quasi-steady flow. We could quantify the previous statement by returning to Eq. (32), and averaging it in  $\theta$  and  $\phi$  over length scales of size  $L_\theta$  and  $L_\phi$ , respectively.

$$\mathcal{J} = \overline{Ro} \ O\left(\frac{L_\theta}{r_0}\right) \quad (84)$$

$$\mathcal{K} = \overline{Ro} \ O\left(\frac{r_0}{L_\phi} \frac{V_\theta}{V_\phi}\right) \quad (85)$$

$$\mathcal{L} = \overline{Ro} \ O\left(\frac{D}{L_\theta}\right) \quad (86)$$

$$\mathcal{M} = \overline{Ro} \ O\left(\frac{Dr_0}{L_\theta L_\phi} \frac{V_r}{V_\phi}\right) \quad (87)$$

$$\mathcal{P} = 1, \quad (88)$$

where  $\overline{Ro} \equiv V_\phi / (f_0 L_\theta)$ . Note that the term  $\mathcal{N}$  comes from  $\omega_\phi (\nabla \cdot \mathbf{v})$ , and the terms  $\mathcal{B}$ ,  $\mathcal{C}$ , and  $\mathcal{D}$  come  $(\mathbf{v} \cdot \nabla) \omega_\phi$ . It should be obvious that estimating the magnitudes of terms by replacing  $\partial / \partial \theta$  with  $r_0 / L_\theta$ ;  $\partial / \partial \phi$  with  $r_0 / L_\phi$ ; and  $\partial / \partial r$  with  $1/D$  as we did to obtain Eqs. (75)–(87), will lead to an estimate that the  $\mathcal{N}$  term is of the same order as the  $\mathcal{B}$ ,  $\mathcal{C}$ , and  $\mathcal{D}$  terms.<sup>17</sup> Using this estimate for  $\mathcal{N}$  and the assumptions numbered 2 – 4 in Section 4.1 that  $D \leq O(r_0)$ ,  $D \leq O(L_\theta)$ , and  $D \leq O(L_\phi)$ , we see by inspection that all of the terms  $\mathcal{B} - \mathcal{N}$  are of order

$$\overline{Ro} \ O\left(\frac{r_0}{D} \frac{V_r V_\theta}{V_\phi^2}, \frac{r_0}{L_\theta} \frac{V_r^2}{V_\phi^2}, \frac{D}{L_\theta} \frac{V_\theta^2}{V_\phi^2}, \frac{r_0}{L_\phi} \frac{V_\theta}{V_\phi}, \frac{Dr_0}{L_\theta L_\phi} \frac{V_r}{V_\phi}, \frac{D}{L_\theta}, \frac{DL_\theta}{r_0 L_\phi} \frac{V_r}{V_\phi}, \frac{L_\theta}{r_0}\right). \quad (89)$$

or less.

We can make a further simplification of the fractional errors if the flow is divergence-free, which implies:

$$V_r / D \leq O(V_\theta / L_\theta, V_\phi / L_\phi). \quad (90)$$

Using this expression<sup>18</sup> to replace  $V_r / D$  in expression (89), and again using assumptions numbered 2 – 4 in Section 4.1 shows that all of the terms  $\mathcal{B} - \mathcal{N}$  are of order

$$O\left[\overline{Ro}, \overline{Ro} \left(\frac{r_0}{L_\theta} \frac{V_\theta^2}{V_\phi^2}, \frac{r_0}{L_\phi} \frac{V_\theta}{V_\phi}, \frac{r_0}{L_\phi}, \frac{D}{L_\theta}\right)\right] \quad (91)$$

or less, where  $\widetilde{Ro}$  is another type of Rossby with  $\widetilde{Ro} \equiv V_\phi / (f_0 r_0)$ . If expression (91) is small compared to unity,<sup>19</sup> and if  $\frac{Dr_0}{L_\theta^2}$  is also small compared to unity, then terms  $\mathcal{A} - \mathcal{N}$  are small compared to the  $\mathcal{P}$  term, and the effect of terms  $\mathcal{A} - \mathcal{N}$  in Eq. (48) can be written as fractional error terms. In particular, Eq. (48) can be re-written:

$$\frac{g'}{r\rho} \frac{\partial^2 \rho}{\partial \theta^2} \Big|_p = f_0 \frac{\partial v_\phi}{\partial r} \left\{ 1 + O\left[\overline{Ro} \left(\frac{r_0}{L_\theta} \frac{V_\theta^2}{V_\phi^2}, \frac{r_0}{L_\phi} \frac{V_\theta}{V_\phi}, \frac{r_0}{L_\phi}, \frac{D}{L_\theta}\right), \frac{DV_\phi^2}{gL_\phi^2}, \frac{DV_\theta^2}{gL_\phi^2}, \frac{DV_\phi V_\theta}{gL_\phi L_\theta}, \frac{Dr_0}{L_\theta^2}, \widetilde{Ro}\right]\right\}, \quad (92)$$

where we have included *all* of the fractional errors that we have made, (including the approximation used in Appendix B in Eq. (124) with the exceptions of the very modest approximations:  $D \leq O(r_0)$ ,  $D \leq O(L_\theta)$ ,  $D \leq O(L_\phi)$ , and that the flow is sufficiently

<sup>17</sup> Actually, this estimate for  $\mathcal{N}$  is very likely to be a large overestimate because most of the flows in planetary atmospheres are nearly divergence-free. This overestimate means that our final estimate of the fraction errors in the EQTWE might be inflated. However, this is consistent with all of our estimates of the fractional errors because we are purposefully taking a conservative approach to error estimation and not considering that there are cancellations between large terms.

<sup>18</sup> This is likely to be an overestimate of the magnitude of  $V_r / D$  when the horizontal divergence of the velocity is small compared to  $V_\theta / L_\theta$  or  $V_\phi / L_\phi$ , which is often the case in planetary flows.

<sup>19</sup> If the term  $\frac{1}{r} \frac{\partial v_\phi}{\partial r} \frac{\partial v_\theta}{\partial \theta}$  had not canceled in Eqs. (46) and (47), then there would be an additional fractional error term of  $\overline{Ro} (r_0 / L_\theta)$ , which could be very large if  $r_0 \gg L_\theta$ .

steady in time that the characteristic value of  $\partial\omega_\phi/\partial t$  at the equator is less than or equal to the characteristic value of  $\mathbf{v}\cdot\nabla\omega_\phi$  at the equator. If Eq. (2) is valid, then

$$\frac{g'}{rT} \frac{\partial^2 T}{\partial\theta^2} \Big|_p = -f_0 \frac{\partial v_\phi}{\partial r} \left\{ 1 + O \left[ \overline{Ro} \left( \frac{r_0}{L_\theta} \frac{V_\theta^2}{V_\phi^2}, \frac{r_0}{L_\phi} \frac{V_\theta}{V_\phi}, \frac{r_0}{L_\phi}, \frac{D}{L_\theta} \right), \frac{DV_\theta^2}{gL_\phi^2}, \frac{DV_\theta^2}{gL_\theta^2}, \frac{DV_\phi V_\theta}{gL_\phi L_\theta}, \frac{Dr_0}{L_\theta^2}, \widetilde{Ro} \right] \right\}. \quad (93)$$

Eqs. (92) and (93) may be considered to be “overkill” with respect to listing all of the fractional errors. The long expressions for the fractional errors come about because we have considered the possibility that the characteristic two horizontal  $V_\phi$  and  $V_\theta$  could be very different and that  $L_\phi$  and  $L_\theta$  could be very different. Usually (c.f., Pedlosky, 1979, Chapter 2), the characteristic velocities would be considered the same. Similarly, the two characteristic horizontal lengths  $L_\phi$  and  $L_\theta$  would also be considered the same.

To compare our fractional errors of the EQTWE to the reported fractional errors in the textbook TWE, we can take a less cautious approach to estimating error size by assuming (as many other authors have) that  $V_\phi/L_\phi \approx V_\theta/L_\theta$ . Using this relationship, the fractional errors in the EQTWE are:

$$O \left[ \overline{Ro} \left( \frac{r_0 L_\theta}{L_\phi^2}, \frac{r_0}{L_\phi}, \frac{D}{L_\theta} \right), \frac{DV_\theta^2}{gL_\phi^2}, \frac{Dr_0}{L_\theta^2}, \widetilde{Ro} \right]. \quad (94)$$

If we are even less cautious and adopt the traditional assumption that  $V_\phi = V_\theta$ , then the fractional errors in the EQTWE are:

$$O \left[ \overline{Ro} \frac{r_0}{L_\phi}, \frac{DV_\phi^2}{gL_\phi^2}, \frac{Dr_0}{L_\phi^2}, \widetilde{Ro} \right]. \quad (95)$$

Thus for a mirror-symmetric flow, the EQTWE is:

$$-\frac{g'}{rT} \frac{\partial^2 T}{\partial\theta^2} \Big|_p = f_0 \frac{\partial v_\phi}{\partial r} \quad (96)$$

with fractional errors in Eqs. (93), (94), or Eq. (95).

If Eq. (2) is not valid (as is the case of Neptune Tollefson et al., 2018), then the wind shear is related to the density by the “equatorial density wind equation” (EQDWE), which from Eq. (92) is:

$$\frac{g'}{r\rho} \frac{\partial^2 \rho}{\partial\theta^2} \Big|_p = f_0 \frac{\partial v_\phi}{\partial r} \quad (97)$$

This equation has the same fractional errors as the EQTWE. It can be re-written to look like the EQTWE if the kinetic temperature  $T$  is replaced with the virtual temperature as done by Tollefson et al. (2018) in applying it to the zonal flows of Neptune.

We close this section with comments about the derivation we wish to stress. If the assumptions enumerated in Section 4.1 are true, Eqs. (96) and (97) are valid at and near the equator. The reason the textbook TWE does not work at the equator is because the second term on the right-hand side of Eq. (48) equals zero, meaning that other terms must balance the thermal component. However, as we have shown *all* terms in the equation are zero at the equator. We also point out that the detailed fractional errors in the textbook TWE can be derived (without assuming that  $V_\theta = V_\phi$  and that  $L_\theta = L_\phi$ ), by re-examining Eq. (48) and using the estimating techniques employed in Section A.3 to determine the relative importance of the terms on the left side of the equation to the terms on the right side.

#### A4. Extension of the Equatorial Thermal Wind Equation (EQTWE) to flows without mirror-symmetry

In this section we drop the assumption that the flow is mirror-symmetric and re-derive the EQTWE along with its fractional er-

rors. We shall show that the only change needed for a non-mirror-symmetric flow is that EQTWE now relates the mirror-symmetric components of the temperature or density to the mirror-symmetric component of the azimuthal velocity, such that Eq. (96) becomes

$$-\frac{g'}{rT^M} \frac{\partial^2 T^M}{\partial\theta^2} \Big|_p = f_0 \frac{\partial v_\phi^M}{\partial r}, \quad (98)$$

and Eq. (97) becomes

$$\frac{g'}{r\rho^M} \frac{\partial^2 \rho^M}{\partial\theta^2} \Big|_p = f_0 \frac{\partial v_\phi^M}{\partial r}. \quad (99)$$

The only fractional error that these equations have that are in addition to those already listed in Eqs. (92) or (93) is  $O\{[\rho^A]/[\rho^M]\}^2$  or  $O\{[T^A]/[T^M]\}^2$ , respectively. Note that these equations are formally valid only at the equator. However, we can employ them at small distances from the equator, e.g., the entry location of the *Galileo* velocity probe data, by suitable Taylor expansions.

We begin by taking the anti-mirror-symmetric component of Eq. (48) to obtain.

$$\begin{aligned} & -f_0 \frac{\cos\theta}{r} \frac{\partial v_\phi^M}{\partial\theta} + \left\{ (\mathbf{v}\cdot\nabla)\omega_\phi + v_\phi(\omega_r - \omega_\theta \tan\theta)/r \right. \\ & - \frac{\omega_\phi}{r \cos\theta} \frac{\partial v_\phi}{\partial\phi} - \omega_\phi(v_r - v_\theta \tan\theta)/r - \frac{v_\phi \tan\theta}{r} \frac{\partial v_\phi}{\partial r} \\ & - \frac{1}{r \cos\theta} \frac{\partial v_\phi}{\partial r} \frac{\partial v_\theta}{\partial\phi} - \frac{1}{r^2} \frac{\partial v_\phi}{\partial\theta} \left[ v_\phi - \frac{1}{\cos\theta} \frac{\partial v_r}{\partial\phi} \right] \\ & \left. + (\nabla\cdot\mathbf{v})\omega_\phi \right\}^A = - \left( \frac{g'}{r\rho^M} \frac{\partial \rho^M}{\partial\theta} \Big|_p \right) \left\{ 1 + O \left[ \left( \frac{\rho^A}{\rho^M} \right)^2 \right] \right\} \\ & + f_0 \sin\theta \frac{\partial v_\phi^M}{\partial r}. \end{aligned} \quad (100)$$

The large brackets with the superscript  $A$ ,  $\{\}^A$  means “take the anti-mirror-symmetric component of the quantity within the brackets”. We have used the facts that the anti-mirror-symmetric component of  $-f_0 \frac{\cos\theta}{r} \frac{\partial v_\phi}{\partial\theta}$  is exactly  $-f_0 \frac{\cos\theta}{r} \frac{\partial v_\phi^M}{\partial\theta}$ , and that the anti-mirror-symmetric component of  $f_0 \sin\theta \frac{\partial v_\phi}{\partial r}$  is exactly  $f_0 \sin\theta \frac{\partial v_\phi^M}{\partial r}$ . We also used the fact<sup>20</sup> that the anti-mirror-symmetric component of  $\frac{g'}{r\rho} \frac{\partial \rho}{\partial\theta} \Big|_p$  is  $\frac{g'}{r\rho^M} \frac{\partial \rho^M}{\partial\theta} \Big|_p$  with a fractional error of  $O\{[\rho^A]/[\rho^M]\}^2$ .

Following the methodology used in Section A.2 (and the spirit of l'Hôpital's Rule), we Taylor-expand each term in Eq. (100), divide by  $\theta$ , and retain only the first term. The Taylor expansion of

<sup>20</sup> We note that the anti-mirror-symmetric component of  $\frac{g'}{r\rho} \frac{\partial \rho}{\partial\theta} \Big|_p$  is

$$\left[ \frac{g'}{r\rho^M} \frac{\partial^2 \rho^M}{\partial\theta^2} \Big|_p - \frac{g'}{r(\rho^M)^2} \left( \frac{\partial \rho^A}{\partial\theta} \Big|_p \right)^2 \right] \theta + O(\theta^3). \quad (101)$$

If we could accurately measure  $\frac{\partial v_\phi^M}{\partial\theta} \Big|_p$ , we would have an equatorial density wind equation or EQDWE of the form  $\frac{g'}{r\rho^M} \left[ \frac{\partial^2 \rho^M}{\partial\theta^2} \Big|_p - \frac{1}{\rho^M} \left( \frac{\partial \rho^A}{\partial\theta} \Big|_p \right)^2 \right] = f_0 \frac{\partial v_\phi^M}{\partial r}$ , and this equation would hold without fractional errors involving  $[\rho^A]/[\rho^M]$ . A similar expression can be found for the EQTWE (see Eq. (20) below) without fractional errors that involve  $[T^A]/[T^M]$ .

$$-f_0 \frac{\cos\theta}{r} \frac{\partial v_\phi^M}{\partial\theta} \text{ is an odd series in } \theta \text{ and is}$$

$$-\theta \frac{f_0}{r} \left[ \frac{\partial^2 v_\phi^M}{\partial\theta^2} \right] + \theta^3 \left\{ \frac{f_0}{2r} \left[ \frac{\partial^2 v_\phi^M}{\partial\theta^2} \right] - \frac{f_0}{6r} \left[ \frac{\partial^4 v_\phi^M}{\partial\theta^4} \right] \right\} + O(\theta^5), \quad (102)$$

where the expressions in large square brackets should be evaluated at the equator. So, for this term we retain only

$$-\left[ \frac{f_0}{r} \frac{\partial^2 v_\phi^M}{\partial\theta^2} \right], \quad (103)$$

The term in Eq. (103) is similar to the  $\mathcal{A}$  term in Eq. (59). As another example, the Taylor series expansion of  $f_0 \sin\theta \frac{\partial v_\phi^M}{\partial r}$  in Eq. (100) is also an odd series in  $\theta$ :

$$f_0 \theta \left[ \frac{\partial v_\phi^M}{\partial r} \right] + \theta^3 f_0 \left\{ \left[ \frac{\partial^3 v_\phi^M}{\partial r \partial \theta^2} \right] / 2 - \left[ \frac{\partial v_\phi^M}{\partial r} \right] / 6 \right\} + O(\theta^5) \quad (104)$$

So, we retain only

$$\left[ f_0 \frac{\partial v_\phi^M}{\partial r} \right], \quad (105)$$

The term in Eq. (105) is similar to the  $\mathcal{P}$  term in Eq. (74). The same estimates that were used in Section A.3 show that the term in Eq. (103) is smaller than the term in Eq. (105) by a factor of  $\frac{Dr_0}{L_\theta^2}$ .

Therefore, we can drop the term  $-f_0 \frac{\cos\theta}{r} \frac{\partial v_\phi^M}{\partial\theta}$  from Eq. (100) and account for it by noting that it leads to a fractional error of  $O\left(\frac{Dr_0}{L_\theta^2}\right)$ .

After dividing by  $\theta$ , the first term in the Taylor series expansion of  $\frac{g'}{r\rho^M} \frac{\partial\rho^M}{\partial\theta}$  in Eq. (100) is

$$\left[ \frac{g'}{r\rho^M} \frac{\partial^2\rho^M}{\partial^2\theta} \right]_p, \quad (106)$$

where all of the quantities and their derivatives should be evaluated at the equator.

By definition, the long, multi-term expression in Eq. (100) that has  $\{\}^A$  is anti-mirror-symmetric. Therefore when it is expanded as a Taylor series about the equator, it is an odd series in  $\theta$ . Following the procedure in Section A.2, we could find the first non-vanishing term of the Taylor series expansion of each of these terms, and then estimate their magnitudes following our method in Section A.3. However, it is not necessary to do so. In Section A.3, we found that the terms surrounded by  $\{\}^A$  were all much smaller<sup>21</sup> than the term in Eq. (105), and we calculated the resulting fractional errors in Eq. (48) that would arise if we dropped them. Our analysis did *not* depend on the symmetry of the terms, but only on the estimates of their velocities and lengths. These estimates still hold, so the analysis in Section A.3 also works for Eq. (100) as do the estimates of the fractional errors that arise when the terms surrounded by  $\{\}^A$  are dropped from Eq. (100). Equating expression (105) to expression (106), we obtain the equatorial density wind equation, EQDWE, or Eq. (99). If Eq. (2) is valid, then the EQTWE, or Eq. (10) follows. These two equations have the fractional errors listed in Section 4.1.

<sup>21</sup> This is only true if  $|\mathbf{v}^A| \leq |\mathbf{v}^M|$ , so we should include this inequality in our list of assumptions in Section 4.1. However, this inequality holds for all of the giant gaseous planets. For example, there is no planet in which the zonal component of the velocity,  $v_\phi$ , near the equator is mostly anti-symmetric.

## Appendix B

Here we prove the identities in spherical coordinates:

$$\frac{\nabla P \times \nabla \rho}{\rho^2} \equiv \frac{1}{\rho^2} \frac{\partial P}{\partial r} \hat{\mathbf{r}} \times \nabla_\perp \rho \Big|_p + \frac{\nabla_\perp P \times \nabla_\perp \rho}{\rho^2} \quad (107)$$

$$\equiv -\frac{g}{\rho} \hat{\mathbf{r}} \times \nabla_\perp \rho \Big|_p + \frac{\nabla_\perp P \times \nabla_\perp \rho}{\rho^2} + \frac{1}{\rho^2} \left( \frac{\partial P}{\partial r} + \rho g \right) \hat{\mathbf{r}} \times \nabla_\perp \rho \Big|_p, \quad (108)$$

where  $\nabla_\perp$  is the horizontal (i.e., non-radial or  $\theta$  and  $\phi$  directions) component of the gradient operator holding  $r$  constant, and where  $\nabla_\perp \Big|_p$  is the horizontal (i.e., non-pressure coordinate direction) component of the gradient operator holding  $P$  constant. Partial derivatives with respect to  $r$  implicitly mean to hold  $\theta$  and  $\phi$  constant. These identities will allow us to relate the gradients of the temperature along constant  $r$  surfaces  $\nabla_\perp T$  to gradients of the temperature along constant  $P$  surfaces  $\nabla_\perp \Big|_p T$ . Approximations of these relationships are implicitly used in most textbook derivations of the thermal wind equation, but for completeness, we derive them here with *no* approximations.

We start with the chain rule identity between the  $(r, \theta, \phi)$  coordinates and the  $(P, \theta, \phi)$  coordinates:

$$\frac{\partial \rho}{\partial \theta} \Big|_{P,\phi} \equiv \frac{\partial \rho}{\partial \theta} \Big|_{r,\phi} + \frac{\partial \rho}{\partial r} \Big|_{\theta,\phi} \frac{\partial r}{\partial \theta} \Big|_{P,\phi}, \quad (109)$$

where we remind the reader that the subscripts of the large vertical bars are the independent variables that remain fixed during the partial differentiation. A similar chain rule is

$$\frac{\partial \rho}{\partial \phi} \Big|_{P,\theta} \equiv \frac{\partial \rho}{\partial \phi} \Big|_{r,\theta} + \frac{\partial \rho}{\partial r} \Big|_{\theta,\phi} \frac{\partial r}{\partial \phi} \Big|_{P,\theta}, \quad (110)$$

Combining Eqs. (109) and (110) gives a “horizontal gradient” chain rule:

$$\nabla_\perp \rho \Big|_p \equiv \nabla_\perp \rho \Big|_r + \frac{\partial \rho}{\partial r} \Big|_{\theta,\phi} \nabla_\perp r \Big|_p. \quad (111)$$

Using another chain rule identity

$$\frac{\partial P}{\partial r} \Big|_{\theta,\phi} \frac{\partial r}{\partial \theta} \Big|_{P,\phi} \frac{\partial \theta}{\partial P} \Big|_{r,\phi} \equiv -1, \quad (112)$$

we obtain

$$\frac{\partial r}{\partial \theta} \Big|_{P,\phi} \equiv -\frac{\partial P}{\partial \theta} \Big|_{r,\phi} / \frac{\partial P}{\partial r} \Big|_{\theta,\phi}. \quad (113)$$

A chain rule similar to Eq. (113) is

$$\frac{\partial r}{\partial \phi} \Big|_{P,\theta} \equiv -\frac{\partial P}{\partial \phi} \Big|_{r,\theta} / \frac{\partial P}{\partial r} \Big|_{\theta,\phi}. \quad (114)$$

Combining Eqs. (113) and (114) gives

$$\nabla_\perp r \Big|_p \equiv -\nabla_\perp P / \frac{\partial P}{\partial r} \Big|_{\theta,\phi}. \quad (115)$$

Using Eq. (115), we eliminate  $\nabla_\perp r \Big|_p$  from Eq. (111) and obtain

$$\nabla_\perp \rho \Big|_p \equiv \nabla_\perp \rho - \left[ \left( \frac{\partial \rho}{\partial r} \right) / \left( \frac{\partial P}{\partial r} \right) \right] \nabla_\perp P \quad (116)$$

The tautology:

$$\nabla P \times \nabla \rho \equiv \frac{\partial P}{\partial r} \hat{\mathbf{r}} \times \nabla_\perp \rho - \frac{\partial \rho}{\partial r} \hat{\mathbf{r}} \times \nabla_\perp P + \nabla_\perp P \times \nabla_\perp \rho, \quad (117)$$

combined with Eq. (116) gives

$$\nabla P \times \nabla \rho \equiv \frac{\partial P}{\partial r} \hat{\mathbf{r}} \times \left\{ \nabla_{\perp} \rho - \left[ \left( \frac{\partial \rho}{\partial r} \right) / \left( \frac{\partial P}{\partial r} \right) \right] \nabla_{\perp} P \right\} + \nabla_{\perp} P \times \nabla_{\perp} \rho \quad (118)$$

However using Eq. (116), we see that the expression in the large curly brackets in Eq. (118) is equal to  $\nabla_{\perp} \rho|_p$ , so Eq. (118) becomes

$$\begin{aligned} \nabla P \times \nabla \rho &= \frac{\partial P}{\partial r} \hat{\mathbf{r}} \times \nabla_{\perp} \rho|_p + \nabla_{\perp} P \times \nabla_{\perp} \rho \quad (119) \\ &= -g\rho \hat{\mathbf{r}} \times \nabla_{\perp} \rho|_p + \left( \frac{\partial P}{\partial r} + \rho g \right) \hat{\mathbf{r}} \times \nabla_{\perp} \rho|_p + \nabla_{\perp} P \times \nabla_{\perp} \rho \quad (120) \end{aligned}$$

Note that we are only interested in the  $\phi$  component of  $(\nabla P \times \nabla \rho)$ :

$$\hat{\phi} \cdot (\nabla P \times \nabla \rho) = \frac{g\rho}{r} \frac{\partial \rho}{\partial \theta} \Big|_p \left[ 1 - \left( \frac{1}{g\rho} \frac{\partial P}{\partial r} + 1 \right) \right] \quad (121)$$

$$= \frac{g\rho}{r} \frac{\partial \rho}{\partial \theta} \Big|_p \left[ 1 + \frac{1}{g} \left( \frac{\partial v_r}{\partial t} + (\mathbf{v} \cdot \nabla) v_r - f_0 \cos \theta (v_\phi + r f_0/4) - v_\phi^2/r \right) \right] \quad (122)$$

$$= \frac{g'\rho}{r} \frac{\partial \rho}{\partial \theta} \Big|_p \left[ 1 + \frac{1}{g'} \left( \frac{\partial v_r}{\partial t} + (\mathbf{v} \cdot \nabla) v_r - f_0 \cos \theta v_\phi - v_\phi^2/r \right) \right] \quad (123)$$

$$= \frac{g'\rho}{r} \frac{\partial \rho}{\partial \theta} \Big|_p \left[ 1 + O \left( \frac{DV_\phi^2}{g'L_\phi^2}, \frac{DV_\theta^2}{g'L_\theta^2}, \frac{DV_\phi V_\theta}{g'L_\phi L_\theta}, \frac{f_0 V_\phi}{g'}, \frac{V_\phi^2}{g'r_0} \right) \right], \quad (124)$$

where we used the radial component of Euler's equation to go from Eq. (121) to Eq. (122), and we used Eq. (90) and the assumption that the characteristic time for  $\mathbf{v}_r$  is sufficiently slow that  $|\partial \mathbf{v}_r / \partial t|$  is less than or equal to one or more of the other terms within the large parentheses to go from Eq. (123) to Eq. (124). Note that the last two fractional errors in Eq. (124) are small compared to the third fractional error if  $\bar{R}\bar{\omega} \leq 1$ . Table 1 shows that  $\bar{R}\bar{\omega} \ll 1$  and that the other fractional errors in Eq. (124) are small, so that subject to these small fractional errors, we obtain:

$$\hat{\phi} \cdot (\nabla P \times \nabla \rho) \simeq \frac{g'\rho}{r} \frac{\partial \rho}{\partial \theta} \Big|_p. \quad (125)$$

Note that using the same reasoning as we used above, we can show that

$$\frac{\nabla P \times \nabla T}{T\rho} \equiv \frac{1}{T\rho} \frac{\partial P}{\partial r} \hat{\mathbf{r}} \times \nabla_{\perp} T \Big|_p + \frac{\nabla_{\perp} P \times \nabla_{\perp} T}{T\rho} \quad (126)$$

$$\begin{aligned} &\equiv -\frac{g}{T} \hat{\mathbf{r}} \times \nabla_{\perp} T \Big|_p + \frac{\nabla_{\perp} P \times \nabla_{\perp} T}{T\rho} \\ &+ \frac{1}{T\rho} \left( \frac{\partial P}{\partial r} + \rho g \right) \hat{\mathbf{r}} \times \nabla_{\perp} T \Big|_p, \quad (127) \end{aligned}$$

and that

$$\hat{\phi} \cdot (\nabla P \times \nabla \rho) \simeq -\frac{g'T}{r} \frac{\partial T}{\partial \theta} \Big|_p. \quad (128)$$

Finally, we note that for the observable layers of the atmospheres of the giant gas planets, generally the horizontal gradients of the temperature and density along surfaces of constant pressure are similar to their values along surfaces of constant  $r$ . To see this, note

that Eq. (116) shows that when  $V_\theta \simeq V_\phi$  and  $L_\theta \simeq L_\phi$  that

$$\left\| \nabla_{\perp} \rho \Big|_p - \nabla_{\perp} \rho \right\| / \left\| \nabla_{\perp} \rho \right\| \simeq O(V_\theta^2 / (gD), (V_\theta^2 \sin \theta) / (gD\bar{R}\bar{\omega})). \quad (129)$$

An equation similar to Eq. (129) holds for the temperature.

### Appendix C

We wish to apply the equatorial density wind equation, EQDWE, in Eq. (99) to the *Galileo* probe wind shear measurements on Jupiter. In this case, it is possible that the EQTWE does not apply because the atmosphere is a mixture with more than one component, and the mixing ratios of the components may be functions of location, so Eq. (2) is not valid. (Neptune has a non-constant mixing ratio, so the modification below is required – see Tollefson et al., 2018). Here, we re-write the EQDWE in a form that is easier to apply to the observations. Note that

$$\rho \equiv \rho_{H-He} + \rho_X, \quad (130)$$

where  $\rho$  is the total density,  $\rho_{H-He}$  is the density due to the “dry” hydrogen-helium atmosphere without condensibles, and  $\rho_X$  is the density due to a condensible species X, which could be water or methane or ammonia, etc. This equation is exact. Here, we limit ourselves to just one condensible species.

$$P = P_{H-He} + P_X, \quad (131)$$

where  $P$  is the total pressure,  $P_{H-He}$  is the partial pressure due to the “dry” hydrogen-helium atmosphere, and  $P_X$  is the partial pressure due to species X. This equation is Dalton's law of partial pressure. We assume that the ideal gas law for a mixture applies:

$$P = T(R_{H-He} \rho_{H-He} + R_X \rho_X) \quad (132)$$

$$= \bar{R}T(\rho_{H-He}/\mu_{H-He} + \rho_X/\mu_X), \quad (133)$$

where  $\bar{R}$  is the universal gas constant (independent of species),  $\mu_{H-He}$  is the molecular weight of the hydrogen-helium mixture,  $\mu_X$  is the molecular weight of species X,  $R_{H-He} \equiv \bar{R}/\mu_{H-He}$  is the specific gas constant of the hydrogen-helium mixture, and  $R_X \equiv \bar{R}/\mu_X$  is the specific gas constant of species X.

Along an isobar of pressure  $P_0$ ,

$$\frac{P_0}{\bar{R}T} = \frac{\rho_{H-He}}{\mu_{H-He}} + \frac{\rho_X}{\mu_X}, \quad (134)$$

or equivalently

$$\rho_{H-He} = \frac{P_0}{\bar{R}T} \mu_{H-He} - \rho_X \frac{\mu_{H-He}}{\mu_X} \quad (135)$$

$$\rho = \rho_X \left( 1 - \frac{\mu_{H-He}}{\mu_X} \right) + \frac{P_0}{\bar{R}} \frac{\mu_{H-He}}{T}. \quad (136)$$

Thus,

$$\frac{\partial \rho}{\partial \theta} \Big|_p = \left( 1 - \frac{\mu_{H-He}}{\mu_X} \right) \frac{\partial \rho_X}{\partial \theta} \Big|_p - \left( \frac{P_0}{\bar{R}} \frac{\mu_{H-He}}{T} \right) \frac{1}{T^2} \frac{\partial T}{\partial \theta} \Big|_p \quad (137)$$

Therefore up to fractional errors of  $O\{[\rho^A]^2/[\rho^M]^2\}$ , at the equator,

$$\begin{aligned} \frac{1}{\rho^M} \frac{\partial^2 \rho^M}{\partial \theta^2} \Big|_p &= \frac{1}{\rho^M} \frac{\partial^2 \rho_X^M}{\partial \theta^2} \Big|_p \left( 1 - \frac{\mu_{H-He}}{\mu_X} \right) \\ &- \left( \frac{P_0^M}{\bar{R}} \frac{\mu_{H-He}}{T^M} \right) \left( \frac{1}{\rho^M (T^M)^2} \right) \frac{\partial^2 T^M}{\partial \theta^2} \Big|_p \quad (138) \end{aligned}$$

Eqs. (131) and (134) show that

$$\left( \frac{P_0^M}{\bar{R}} \frac{\mu_{H-He}}{T^M} \right) \frac{1}{\rho^M T^M} = \left[ 1 - \frac{\rho_X^M}{\rho^M} \left( 1 - \frac{\mu_{H-He}}{\mu_X} \right) \right]. \quad (139)$$

Using Eq. (139) in Eq. (138), we obtain

$$\frac{1}{\rho^M} \frac{\partial^2 \rho^M}{\partial \theta^2} \Big|_p = - \frac{1}{T^M} \frac{\partial^2 T^M}{\partial \theta^2} \Big|_p \left[ 1 - \frac{\rho_X^M}{\rho^M} \left( 1 - \frac{\mu_{H-He}}{\mu_X} \right) \right] + \frac{1}{\rho^M} \frac{\partial^2 \rho_X^M}{\partial \theta^2} \Big|_p \left( 1 - \frac{\mu_{H-He}}{\mu_X} \right). \quad (140)$$

Planetary and atmospheric scientists generally use the mixing ratio  $m \equiv \rho_X/\rho$ , and to leading order in  $m$  (Fig. 11 shows that  $m$  is order  $10^{-4}$ ), Eq. (140) evaluated at the equator is

$$\frac{1}{\rho^M} \frac{\partial^2 \rho^M}{\partial \theta^2} \Big|_p = - \frac{1}{T^M} \frac{\partial^2 T^M}{\partial \theta^2} \Big|_p \left[ 1 - m^M \left( 1 - \frac{\mu_{H-He}}{\mu_X} \right) \right] + \frac{\partial^2 m^M}{\partial \theta^2} \Big|_p \left( 1 - \frac{\mu_{H-He}}{\mu_X} \right), \quad (141)$$

where  $m^M$  is the mirror-symmetric component of  $m$ . Using Eq. (141) in the EQDWE in Eq. (99), we obtain an equation for the dimensionless vertical shear

$$\frac{f_0 r}{g'} \frac{\partial v_\phi^M}{\partial r} = - \frac{1}{T^M} \frac{\partial^2 T^M}{\partial \theta^2} \Big|_p \left[ 1 - m^M \left( 1 - \frac{\mu_{H-He}}{\mu_X} \right) \right] + \frac{\partial^2 m^M}{\partial \theta^2} \Big|_p \left( 1 - \frac{\mu_{H-He}}{\mu_X} \right). \quad (142)$$

The first term on the right side of Eq. (142) is the contribution to the dimensionless vertical shear due to the temperature. The second term on the right side of Eq. (142) is the *compositional* contribution.

For planetary flows that do not obey an ideal gas equation, such as a liquid planetary center or the nearly incompressible hydrogen core in the deep interior of Jupiter or Saturn, a virtual temperature and the equation above will not be useful. In these cases, one should deal directly with the equatorial density wind equation, or EQDWE, in Eq. (99).

## References

Allen, R.J., Sherwood, S.C., 2008. Warming maximum in the tropical upper troposphere deduced from thermal winds. *Nat. Geosci.* 1 (6), 399–403.

Allison, M., 1990. Planetary waves in Jupiter's equatorial atmosphere. *Icarus* 83 (2), 282–307.

Andrews, D.G., Holton, J.R., Leovy, C.B., 1987. *Middle Atmosphere Dynamics*. Academic press.

Asay-Davis, X.S., Marcus, P.S., Wong, M.H., de Pater, I., 2009. Jupiter's shrinking great red spot and steady oval ba: velocity measurements with the advection corrected correlation image velocimetry-automated cloud-tracking method. *Icarus* 203 (1), 164–188.

Asay-Davis, X.S., Marcus, P.S., Wong, M.H., de Pater, I., 2011. Changes in Jupiter's zonal velocity between 1979 and 2008. *Icarus* 211 (2), 1215–1232.

Atkinson, D.H., Pollack, J.B., A., S., 1998. The Galileo probe doppler wind experiment: measurement of the deep zonal winds on Jupiter. *J. Geophys. Res.* 103 (E10), 911–928.

Atreya, S.K., Romani, P.N., 1985. Photochemistry and clouds of Jupiter, Saturn and Uranus. In: Hunt, G.E. (Ed.), *Recent Advances in Planetary Meteorology*. Cambridge University Press, pp. 17–68.

Barcilon, A., Gierasch, P., 1970. A moist, hadley cell model for Jupiter's cloud bands. *J. Atmos. Sci.* 27 (4), 550–560.

Batchelor, G.K., 2000. *An Introduction to Fluid Dynamics*. Cambridge university press.

Bjoraker, G.L., H., W.W., de Pater, I., Ádámkóvics, 2015. Jupiter's deep cloud structure revealed using Keck observations of spectrally resolved line shapes. *Astrophys. J.* 810 (2), 122–131.

Bolton, S.J., Adriani, A., Adumitroaie, V., Allison, M., Anderson, J., Atreya, S., Bloxham, J., Brown, S., Connerney, J.E.P., DeJong, E., Folkner, W., Gautier, D., Grassi, D., Gulkis, S., Guillot, T., Hansen, C., Hubbard, W.B., Iess, L., Ingersoll, A., Janssen, M., Jorgensen, J., Kaspi, Y., Levin, S.M., Li, C., Lunine, J., Miguel, Y., Mura, A., Orton, G., Owen, T., Ravine, M., Smith, E., P., S., Stone, E., Stevenson, D., Thorne, R., Waite, J., Durante, D., Ebert, R.W., Greathouse, T.K., Hue, V., Parisi, M., Szalay, J.R., Wilson, R., 2017. Jupiter's interior and deep atmosphere: the initial pole-to-pole passes with the Juno spacecraft. *Science* 356, 821–825.

Conrath, B., Flasar, F.M., Hanel, R., Kunde, V., Maguire, W., Pearl, J., Pirraglia, J., Samuelson, R., Gierasch, P., Weir, A., Bezzard, B., Gautier, D., Cruikshank, D., Horn, L., Springer, R., Shaffer, W., 1989. Infrared observations of the neptunian system. *Science* 246 (4936), 1454–1459. doi:10.1126/science.246.4936.1454. <http://science.sciencemag.org/content/246/4936/1454.full.pdf>

de la Torre Juárez, M., Fisher, B., Orton, G., 2002. Large scale geostrophic winds with a full representation of the coriolis force: application to IR observations of the upper jovian troposphere. *Geophys. Astrophys. Fluid Dyn.* 96 (2), 87–114.

de Pater, I., DeBoer, D., Marley, M., Freedman, R., Young, R., 2005. Retrieval of water in Jupiter's deep atmosphere using microwave spectra of its brightness temperature. *Icarus* 173 (2), 425–438.

de Pater, I., Sault, R.J., Butler, B., DeBoer, D., Wong, M.H., 2016. Peering through Jupiter's clouds with radio spectral imaging. *Science* 352 (6290), 1198–1201. doi:10.1126/science.aaf2210. <http://science.sciencemag.org/content/352/6290/1198.full.pdf>

Feynman, R.P., Leighton, R., 1986. *Surely You're Joking, Mr. Feynman! (Adventures of a Curious Character)*. Norton.

Fitzpatrick, P.J., de Pater, I., Luszcz-Cook, S., Wong, M.H., Hammel, H.B., 2014. Dispersion in Neptunes zonal wind velocities from NIR Keck AO observations in July 2009. *Astrophys. Space Sci.* 350 (1), 65–88.

Flasar, F., Achterberg, R., Conrath, B., Gierasch, P., Kunde, V., Nixon, C., Bjoraker, G., Jennings, D., Romani, P., Simon-Miller, A., et al., 2005. Titan's atmospheric temperatures, winds, and composition. *Science* 308 (5724), 975–978.

Flasar, F., Kunde, V., Achterberg, R., Conrath, B., et al., 2004. An intense stratospheric jet on Jupiter. *Nature* 427 (6970), 132.

Fletcher, L.N., de Pater, I., Orton, G.S., Hammel, H.B., Sitko, M.L., Irwin, P.G., 2014. Neptune at summer solstice: zonal mean temperatures from ground-based observations, 2003–2007. *Icarus* 231, 146–167.

Fletcher, L.N., Greathouse, T., Orton, G., Sinclair, J., Giles, R., Irwin, P., Encrenaz, T., 2016. Mid-infrared mapping of Jupiter's temperatures, aerosol opacity and chemical distributions with irtf/texes. *Icarus* 278, 128–161.

French, R.G., McGehee, C.A., Sicardy, B., 1998. Neptune's stratospheric winds from three central flash occultations. *Icarus* 136 (1), 27–49. doi:10.1006/icar.1998.6001.

Friedson, A.J., 2005. Water, ammonia, and H<sub>2</sub>S mixing ratios in Jupiter's five-micron hot spots: a dynamical model. *Icarus* 177 (1), 1–17.

Garcia-Melendo, E., Sánchez-Lavega, A., 2001. A study of the stability of Jovian zonal winds from HST images: 1995–2000. *Icarus* 152 (2), 316–330.

Garcia-Melendo, E., Sánchez-Lavega, A., Legarreta, J., S., P.-H., R., H., 2010. A strong high altitude narrow jet detected at Saturn's equator. *Geophys. Res. Lett.* 37 (22).

Guillot, T., Miguel, Y., Militzer, B., Hubbard, W.B., Kaspi, Y., Galanti, E., Cao, H., Helled, R., Wahl, S.M., Iess, L., Folkner, W.M., Stevenson, D.J., Lunine, J.I., Reese, D.R., Biekman, A., Parisi, M., Durante, D., Connerney, J.E.P., Levin, S.M., Bolton, S.J., 2018. A suppression of differential rotation in Jupiter's deep interior. *Nature* 555, 227EP.

Holton, J.R., 1983. The influence of gravity wave breaking on the general circulation of the middle atmosphere. *J. Atmos. Sci.* 40 (10), 2497–2507.

Ingersoll, A.P., Cuzzi, J.N., 1969. Dynamics of Jupiter's cloud bands. *J. Atmos. Sci.* 26 (5), 981–985.

Ingersoll, A.P., Gierasch, P.J., Banfield, D., Vasavada, A.R., Galileo Imaging Team, 2000. Moist convection as an energy source for the large-scale motions in Jupiter's atmosphere. *Nature* 403 (6770), 630–632.

Kaspi, Y., Galanti, E., Hubbard, W.B., Stevenson, D.J., Bolton, S.J., Iess, L., Guillot, T., Bloxham, J., Connerney, J.E.P., Cao, H., Durante, D., Folkner, W.M., Helled, R., Ingersoll, A.P., Levin, S.M., Lunine, J.I., Miguel, Y., Militzer, B., Parisi, M., Wahl, S.M., 2018. Jupiter's atmospheric jet streams extend thousands of kilometres deep. *Nature* 555, 223EP–.

Kaspi, Y., Guillot, T., Galanti, E., Miguel, Y., Helled, R., Hubbard, W.B., Militzer, B., Wahl, S.M., Levin, S., Connerney, J.E., Bolton, S.J., 2017. The effect of differential rotation on Jupiter's low-degree even gravity moments. *Geophys. Res. Lett.*

Lellouch, E., Bézard, B., Strobel, D., Bjoraker, G., Flasar, F., Romani, P., 2006. On the HCN and CO<sub>2</sub> abundance and distribution in Jupiter's stratosphere. *Icarus* 184 (2), 478–497.

Lewis, J.S., 1969. The clouds of Jupiter and the NH<sub>3</sub>, H<sub>2</sub>O and NH<sub>3</sub>H<sub>2</sub>S systems. *Icarus* 10, 365–378. doi:10.1016/0019-1035(69)90091-8.

Li, C., Ingersoll, A., Janssen, M., Levin, S., Bolton, S., Adumitroaie, V., Allison, M., Arballo, J., Bellotti, A., Brown, S., et al., 2017. The distribution of ammonia on Jupiter from a preliminary inversion of Juno Microwave Radiometer data. *Geophys. Res. Lett.*

Li, L., Achterberg, R.K., Conrath, B.J., Gierasch, P.J., Smith, M.A., Simon-Miller, A.A., Nixon, C.A., Orton, G.S., Flasar, F.M., Jiang, X., et al., 2013. Strong temporal variation over one Saturnian year: from Voyager to Cassini. *Sci. Rep.* 3.

Li, L., Gierasch, P.J., Achterberg, R.K., Conrath, B.J., Flasar, F.M., Vasavada, A.R., Ingersoll, A.P., Banfield, D., Simon-Miller, A.A., Fletcher, L.N., 2008. Strong jet and a new thermal wave in Saturn's equatorial stratosphere. *GRL* 35, L23208. doi:10.1029/2008GL035515.

Li, L., Ingersoll, A.P., Vasavada, A.R., Simon-Miller, A.A., Del Genio, A.D., Ewald, S.P., Porco, C.C., West, R.A., 2006. Vertical wind shear on Jupiter from Cassini images. *J. Geophys. Res.* 111 (E4).

Liu, J., Schneider, T., 2010. Mechanisms of jet formation on the giant planets. *J. Atmos. Sci.* 67 (11), 3652–3672. doi:10.1175/2010JAS3492.1.

Magalhães, J.A., Seiff, A., Young, R.E., 2002. The stratification of Jupiter's troposphere at the Galileo probe entry site. *Icarus* 158 (2), 410–433.

Matcheva, K.I., Conrath, B.J., Gierasch, P.J., Flasar, F.M., 2005. The cloud structure of the Jovian atmosphere as seen by the Cassini/CIRS experiment. *Icarus* 179 (2), 432–448.

Niemann, H.B., Atreya, S.K., Carignan, G.R., Donahue, T.M., Haberman, J.A., Harpold, D.N., Hartle, R.E., Hunten, D.M., Kasprzak, W.T., Mahaffy, P.R., Owen, T.C., Way, S.H., 1998. The composition of the Jovian atmosphere as determined by the Galileo probe mass spectrometer. *J. Geophys. Res.* 103, 22831–22846. doi:10.1029/98JE01050.

- Ortiz, J.L., Orton, G.S., Friedson, A.J., Stewart, S.T., Fisher, B.M., Spence, J.R., 1998. Evolution and persistence of 5-micron hot spots at the Galileo probe entry latitude. *J. Geophys. Res.* 103 (10), 23051–23069.
- Orton, G., Momary, T., Ingersoll, A., Adriani, A., Hansen, C., Janssen, M., Arballo, J., Atreya, S., Bolton, S., Brown, S., et al., 2017. Multiple-wavelength sensing of Jupiter during the Juno mission's first perijove passage. *Geophys. Res. Lett.*
- Pedlosky, J., 1979. *Geophysical Fluid Dynamics*. Springer Science & Business Media.
- Porco, C.C., Baker, E., Barbara, J., Beurle, K., Brahic, A., Burns, J.A., Charnoz, S., Cooper, N., Dawson, D.D., Del Genio, A.D., et al., 2005. Cassini imaging science: initial results on Saturn's atmosphere: Cassini at Saturn. *Science* 307 (5713), 1243–1247.
- Sánchez-Lavega, A., García-Melendo, E., Pérez-Hoyos, S., Hueso, R., Wong, M.H., Simon, A., Sanz-Requena, J.F., Antuñaño, A., Barrado-Izagirre, N., Garate-Lopez, I., Rojas, J.F., del Río-Gaztelurrutia, T., Gómez-Forrellad, J.M., de Pater, I., Li, L., Barry, T., 2016. An enduring rapidly moving storm as a guide to Saturn's equatorial jet's complex structure. *Nat. Commun.* 7, 13262 EP
- Sault, R.J., Engel, C., de Pater, I., 2004. Longitude-resolved imaging of Jupiter at  $\lambda=2$  cm. *Icarus* 168, 336–343. doi:10.1016/j.icarus.2003.11.014. astro-ph/0612769
- Seiff, A., Kirk, D.B., Knight, T.C., Young, R.E., Mihalov, J.D., Young, L.A., Milos, F.S., Schubert, G., Blanchard, R.C., Atkinson, D., 1998. Thermal structure of Jupiter's atmosphere near the edge of a 5  $\mu$ m hot spot in the north equatorial belt. *J. Geophys. Res.* 103 (E10), 22857–22889.
- Showman, A.P., de Pater, I., 2005. Dynamical implications of Jupiter's tropospheric ammonia abundance. *Icarus* 174, 192–204. doi:10.1016/j.icarus.2004.10.004.
- Showman, A.P., Dowling, T.E., 2000. Nonlinear simulations of Jupiter's 5-micron hot spots. *Science* 289 (5485), 1737–1740.
- Showman, A.P., Ingersoll, A.P., 1998. Interpretation of Galileo probe data and implications for Jupiter's dry downdrafts. *Icarus* 132 (2), 205–220.
- Sun, Z.-P., Stoker, C.R., Schubert, G., 1991. Thermal and humidity winds in outer planet atmospheres. *Icarus* 91 (1), 154–160.
- Tollefson, J., de Pater, I., Marcus, P.S., Luszcz-Cook, S., Sromovsky, L.A., Fry, P.M., Fletcher, L.N., Wong, M.H., 2018. Vertical wind shear in Neptune's upper atmosphere explained with a modified thermal wind equation. *Icarus*.
- Tollefson, J., Wong, M.H., de Pater, I., Simon, A.A., Orton, G.S., Rogers, J.H., Atreyaf, S.K., Cosentino, R.G., Januszewski, W., Morales-Juberias, R., Marcus, P.S., 2017. Changes in Jupiter's zonal wind profile preceding and during the Juno mission. *Icarus*.
- Wong, M.H., Atreya, S.K., Kuhn, W.R., Romani, P.N., Mihalka, K.M., 2015. Fresh clouds: a parameterized updraft method for calculating cloud densities in one-dimensional models. *Icarus* 245, 273–281. doi:10.1016/j.icarus.2014.09.042.
- Wong, M.H., Mahaffy, P.R., Atreya, S.K., Niemann, H.B., Owen, T.C., 2004. Updated Galileo probe mass spectrometer measurements of carbon, oxygen, nitrogen, and sulfur on Jupiter. *Icarus* 171 (1), 153–170. doi:10.1016/j.icarus.2004.04.010.
- Young, R.E., 2003. The Galileo probe: how it has changed our understanding of Jupiter. *New Astron. Rev.* 47, 1–51. doi:10.1016/S1387-6473(02)00272-5.